The Arctic Subpolar gyre sTate Estimate (ASTE): Description and assessment of a data-constrained, dynamically consistent ocean-sea ice estimate for 2002-2017

An T Nguyen[1,1,1,1], Helen Pillar[2,2,2,2], Victor Ocaña[3,3,3], Arash Bigdeli[1,1,1], Timothy A Smith[3,3,3,3], Patrick Heimbach[4,4,4,4], Victor Ocaña[3], and Arash Bigdeli[1]

[1]University of Texas-Austin
[2]The University of Texas at Austin
[3]University of Texas at Austin
[4]university of Texas at Austin

November 30, 2022

Abstract

A description and assessment of the first release of the Arctic Subpolar gyre sTate Estimate (ASTE_R1), a medium-resolution data-constrained ocean-sea ice model-data synthesis spanning the period 2002-2017 is presented. The fit of the model to an extensive (O(10ˆ9)) set of satellite and in situ observations was achieved through adjoint-based nonlinear least-squares optimization. The improvement of the solution compared to an unconstrained simulation is reflected in misfit reductions of 77% for Argo, 50% for satellite sea surface height, 58% for the Fram Strait mooring, 65% for Ice Tethered Profilers, and 83% for sea ice extent. Exact dynamical and kinematic consistency is a key advantage of ASTE_R1, distinguishing the state estimate from existing ocean reanalyses. Through strict adherence to conservation laws, all sources and sinks within ASTE_R1 can be accounted for, permitting meaningful analysis of closed budgets, such as contributions of horizontal and vertical convergence to the tendencies of heat and salt. ASTE_R1 thus serves as the biggest effort undertaken to date of producing a specialized Arctic ocean-ice estimate over the 21st century. Transports of volume, heat, and freshwater are consistent with published observation-based estimates across important Arctic Mediterranean gateways. Interannual variability and low frequency trends of freshwater and heat content are well represented in the Barents Sea, western Arctic halocline, and east subpolar North Atlantic. Systematic biases remain in ASTE_R1, including a warm bias in the Atlantic Water layer in the Arctic and deficient freshwater inputs from rivers and Greenland discharge.

The Arctic Subpolar gyre sTate Estimate (ASTE): Description and assessment of a data-constrained, dynamically consistent ocean-sea ice estimate for 2002–2017

An T. Nguyen[1*], Helen Pillar[1], Victor Ocaña[1], Arash Bigdeli[1], Timothy A. Smith[1], Patrick Heimbach[1,2,3]

[1]Oden Institute for Computational Engineering and Sciences, University of Texas at Austin
[2]Jackson School of Geosciences, University of Texas at Austin
[3]Institute for Geophysics, University of Texas at Austin

Key Points:

- The 2002–2017 medium-resolution Arctic Subpolar gyre sTate Estimate (ASTE) is constrained to 10^9 satellite and in situ observations.
- Strict adherence to conservation laws ensures all sources/sinks can be accounted for, enabling application for meaningful budget analyses.
- ASTE captures the large-scale dynamics of the Arctic ocean-sea ice system including variability and trends in heat and freshwater storage.

*Oden Institute for Computational Engineering and Sciences
The University of Texas at Austin
201 East 24th St., POB 4.234, C0200, Austin, TX, 78712, USA

Corresponding author: An T. Nguyen, atnguyen@oden.utexas.edu

Abstract

A description and assessment of the first release of the Arctic Subpolar gyre sTate Estimate (*ASTE_R1*), a data-constrained ocean-sea ice model-data synthesis, is presented. *ASTE_R1* has a nominal resolution of 1/3° and spans the period 2002-2017. The fit of the model to an extensive (O(10^9)) set of satellite and in situ observations was achieved through adjoint-based nonlinear least-squares optimization. The improvement of the solution compared to an unconstrained simulation is reflected in misfit reductions of 77% for Argo, 50% for satellite sea surface height, 58% for the Fram Strait mooring, 65% for Ice Tethered Profilers, and 83% for sea ice extent. Exact dynamical and kinematic consistency is a key advantage of *ASTE_R1* , distinguishing the state estimate from existing ocean reanalyses. Through strict adherence to conservation laws, all sources and sinks within *ASTE_R1* can be accounted for, permitting meaningful analysis of closed budgets at the grid-scale, such as contributions of horizontal and vertical convergence to the tendencies of heat and salt. *ASTE_R1* thus serves as the biggest effort undertaken to date of producing a specialized Arctic ocean-ice estimate over the 21st century. Transports of volume, heat, and freshwater are consistent with published observation-based estimates across important Arctic Mediterranean gateways. Interannual variability and low frequency trends of freshwater and heat content are well represented in the Barents Sea, western Arctic halocline, and east subpolar North Atlantic. Systematic biases remain in *ASTE_R1* , including a warm bias in the Atlantic Water layer in the Arctic and deficient freshwater inputs from rivers and Greenland discharge.

Plain Language Summary

A 2002–2017 ocean-sea ice reconstruction, *ASTE_R1* , is distributed for use in climate studies over the early 21st century in the northern high latitudes. The product is a model-data synthesis, using a numerical model to interpolate approximately a billion satellite and in situ observations. The primary strength of *ASTE_R1* compared to most existing ocean reanalyses is that strict adherence to the equations describing the fluid flow and conservation laws is built into the product, thus making *ASTE_R1* free from artificial un-physical sources or sinks and associated "jumps" in the time-evolving state. Furthermore, the product is consistent with most available observations, both used in the synthesis and retained for independent verification. This indicates good large-scale representation of evolving sea-ice, ocean currents and water properties, including year-to-year variability and decadal trends in heat and freshwater storage in the Arctic and subpolar North Atlantic. Some systematic data-model differences remain in the product and highlight where extra data and/or model development will improve the next release. The product and underlying model configuration are freely available to the research community.

1 Introduction

The Arctic region has experienced large changes in recent decades. These include near-surface air temperature warming at twice the global rate (Richter-Menge & Jeffries, 2011), rapid decline in multi-year sea ice (Kwok & Cunningham, 2015), enhanced solar radiation absorption in the Western Arctic upper ocean (Timmermans et al., 2018), increased river and glacial discharge (Bamber et al., 2012, 2018; Proshutinsky et al., 2020), and increased influxes of freshwater from the Pacific (Woodgate, 2018) and heat from the Atlantic (Polyakov et al., 2011). Many of these changes have been suggested to trigger positive feedbacks. Enhanced shortwave absorption (Jackson et al., 2010; Perovich et al., 2011; Timmermans et al., 2018), enhanced air-ice-sea momentum transfer (Rainville & Woodgate, 2009; Martin et al., 2014), shoaling of the Atlantic Water layer (Polyakov et al., 2017, 2020), and enhanced heat flux through Fram Strait (Q. Wang et al., 2020) have all been identified to both result from and further amplify sea-ice thinning.

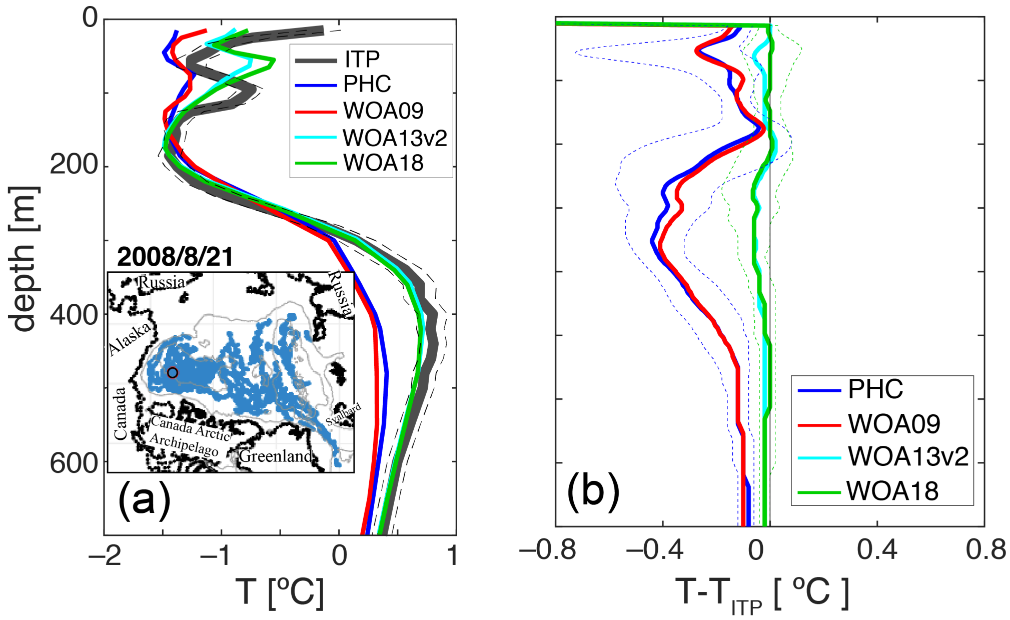

Figure 1. Comparison between ITP-derived temperature and the climatologies from the Polar Hydrography Center (PHC, blue), World Ocean Atlas 2009 (WOA09, red), 2013 version 2 (WOA13v2, cyan), and 2018 (WOA18, green). Panel (a) shows this comparison for **a single** ITP profile on August 21, 2008 (thick dark gray, with the observational uncertainty shown by the thin dashed black lines.). The location of the profile is shown in the inset. Panel (b) shows the 50th percentile difference between all ITP temperature profiles in the Canada Basin and the four climatologies. The dotted lines show the 30th and 70th percentile differences.

Some of the recent changes in the observed Arctic Ocean heat content have been linked to pulsed warming of the Atlantic Water (AW) inflow (Polyakov et al., 2017; Muilwijk et al., 2018) and can be traced back upstream into the subpolar North Atlantic (SPNA; e.g., Årthun & Eldevik, 2016). Given the importance of Arctic changes and their interaction with the SPNA to the global climate system (Carmack et al., 2016), investigations of mechanisms setting the time-mean and evolving state of the Arctic Ocean and exchanges with surrounding ocean basins must be supported by basin-scale estimates of the ocean-sea ice state.

Historically, due to extremely sparse observations, efforts to construct decadal Arctic-focused gridded datasets have been hampered. Realistic simulation of the Arctic and sub-Arctic ocean-sea ice state has remained difficult due to highly uncertain initial conditions. Beginning in the early 2000s, increased availability of *in situ* observations of subsurface ocean hydrography and of oceanic transports across Arctic gateways has improved our understanding of key processes, including interior eddy activity and mixing (Timmermans et al., 2012; Cole et al., 2014; Zhao et al., 2016; Bebieva & Timmermans, 2016), and the transformation and redistribution of watermasses (Proshutinsky et al., 2009; Rabe et al., 2014; Pnyushkov et al., 2015; Timmermans & Jayne, 2016; von Appen et al., 2015a; Polyakov et al., 2017; Timmermans et al., 2018). Over the same time period, new satellite altimetry (Kwok & Morison, 2016), gravimetry (Peralta-Ferriz et al., 2014), and sea ice observations have allowed a more accurate estimate of Ekman transport (Meneghello et al., 2018) and inventory of freshwater in the Western Arctic (Proshutinsky et al., 2019, 2020).

In parallel with increased observational coverage, great progress has also been made using theoretical and modeling frameworks to advance our understanding of Arctic Ocean dynamics, for example, elucidating the importance of eddies in gyre equilibration (Manucharyan & Isachsen, 2019; Meneghello et al., 2017) and vertical heat redistribution (Polyakov et al., 2017). Despite this progress, confident assessment of the time-mean state, interannual variability and identification of robust decadal trends remains challenging (Balmaseda et al., 2015; Timmermans & Marshall, 2020) due to multiple factors (Holloway et al., 2007; Q. Wang et al., 2016b, 2016a; Ilicak et al., 2016; Docquier et al., 2019). The most important amongst these factors is the lack of direct observations throughout the full water column, including at the air-ice-ocean interface, in and just below the mixed layer, along the Atlantic Water (AW) boundary current pathway, and at the shelf-basin regions that connect the dynamics of this energetic current and the relatively quiescent Arctic Ocean interior (Timmermans & Marshall, 2020).

To fill these gaps, the community has constructed climatologies (e.g., WOA13 version 2 and WOA18, Locarnini et al., 2018; Zweng et al., 2018) and data-model syntheses (Stammer et al., 2016; Uotila et al., 2019; Carton et al., 2019) which are assumed to have higher fidelity as the repository of incorporated data grows. The improved fit between the latest climatology and existing observations is far superior to that seen in older climatologies. For example, in the Western Arctic interior, Ice Tethered Profilers (ITP) consistently report warmer temperatures (Fig. 1) than provided by both the Polar Hydrographic Climatology (PHC, Steele et al., 2001) and the World Ocean Atlas 2009 (WOA09, Locarnini et al., 2010; Antonov et al., 2010), but are in close agreement with WOA18. Here it is important to note that this close agreement at the time/location of data acquisition is built into the majority of these climatologies and other existing Arctic model-data syntheses. These products are constructed using statistical methods such as optimal interpolation (e.g., PHC, WOA), 3D-Var, or sequential 4D-Var with short assimilation windows (Stammer et al., 2016; Uotila et al., 2019; Mu et al., 2018; Carton et al., 2019). The advantage of these methods is that the synthesis ensures a local fit to available observations (Fig. 1, Carton et al., 2019). Away from observed locations, however, the interpolator relies on incomplete, unavailable or unobtainable information. Missing values are, for example, determined via spatial/temporal correlations, potentially derived from regions/times of very different dynamics. By construction, high frequency variability cannot be fully accounted for and as a result spectral agreement with observations can be poor (Verdy et al., 2017). Importantly, this type of interpolation – and that used in 3D-Var or sequential 4D-Var – can introduce artificial sources/sinks (e.g., of mass, enthalpy and momentum, Wunsch & Heimbach, 2013; Griffies et al., 2014; Stammer et al., 2016), which make a large contribution to the total energy budget (Balmaseda et al., 2015). This violation of basic conservation principles has been shown to obfuscate the use of these products for robust identification and attribution of change, creating spurious trends (Bengtsson et al., 2004), and triggering artificial loss of balance (Pilo et al., 2018), resulting in adjustments that may propagate and amplify to corrupt the large scale solution (Sivareddy et al., 2017).

To lend additional support to studies of the Arctic ocean-sea ice system over the early 21st century we have developed a new model-data synthesis utilizing the non-linear inverse modeling framework developed within the consortium for Estimating the Circulation and Climate of the Ocean (ECCO, Stammer et al., 2002; Wunsch & Heimbach, 2007; Heimbach et al., 2019). The use of the primitive equations as a dynamical interpolator distinguishes our effort from purely statistical approaches. The inversion consists of an iterative, gradient-based minimization of a least-squares model-data misfit function. Unlike most reanalysis products that are based on sequential data assimilation, only independent, uncertain input variables, i.e. initial conditions, surface boundary conditions and model parameters are adjusted. No periodic analysis increments during the estimation period that would incur artificial sources or sinks are permitted. Through strict adherence to conservation laws, all sources and sinks within the state estimate can be

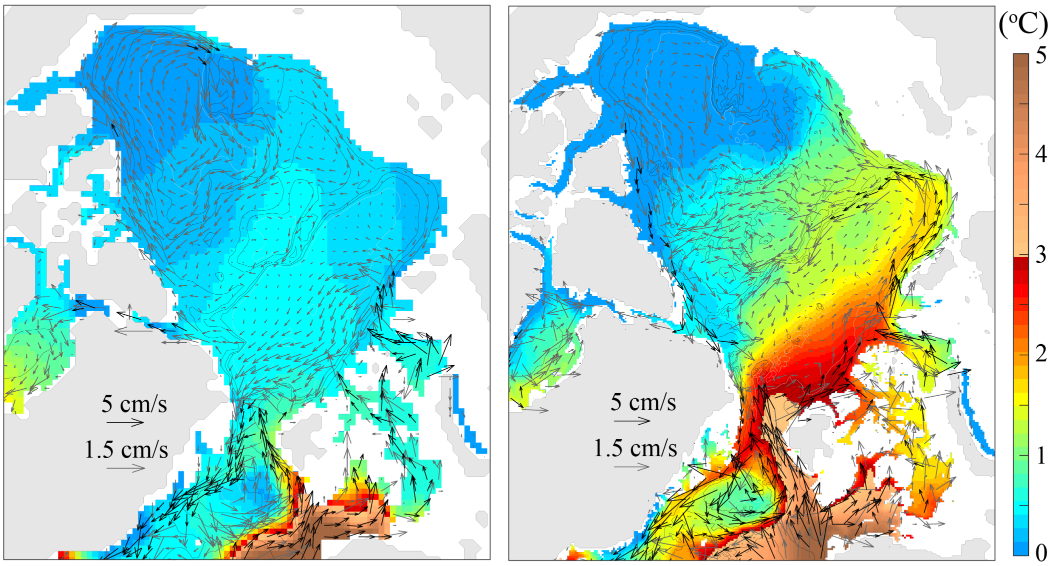

Figure 2. 2002–2015 mean circulation in the Arctic at depth 250 m as represented in ECCOv4r3 (left, averaged over 2x2 grids) and *ASTE_R1* (right, averaged over 6x6 grids). The color scale shows temperature at the same depth from the two solutions. Vector arrows are grouped into speed ranges of [0–1.5] cm/s (gray) and [1.5–5] cm/s (black), with the vector length scales provided.

accounted for over the full estimation period, permitting meaningful analysis of closed budgets (Buckley et al., 2014; Piecuch & Ponte, 2012).

Our work builds upon extensive prior efforts of the ECCO community to produce optimal (in a least-squares sense) kinematically- and dynamically-consistent data-constrained estimates of the ocean state across the globe and in various regional domains. Among the publicly available ECCO state estimates is ECCO Version 4 Release 3 (ECCOv4r3, Forget et al., 2015a; Fukumori et al., 2018a), which has been constrained to satellite and in situ data (including Argo and elephant seal data) outside of the Arctic, ITP data in the Arctic, and other mooring data at important Arctic gateways. The ECCOv4 releases have been widely used, with applications including investigation of global vertical heat and salt redistribution (Liang et al., 2017; Liu et al., 2019), heat budgets in the North Atlantic (Buckley et al., 2014, 2015; Piecuch et al., 2017; Foukal & Lozier, 2018) and the Nordic Seas (Asbjørnsen et al., 2019), high-latitude freshwater budgets (Tesdal & Haine, 2020), and sea level change (Piecuch & Ponte, 2013).

The state-estimation procedure entails reducing the total time- and space-integrated model-data misfit. Since ECCOv4r3 is a global solution, reduction of the relatively well-sampled misfit at lower latitudes dominates the production of this solution. As a result, ECCOv4r3 possesses notable biases in the Arctic (Carton et al., 2019; Tesdal & Haine, 2020), including a strong anticyclonic circumpolar circulation of Atlantic Water (Fig. 2). Furthermore, the ECCOv4r3 horizontal grid spacing of 40–45 km is well above the Rossby deformation radius in the Arctic and Nordic Seas (Nurser & Bacon, 2014). This has motivated a dedicated effort to build a higher resolution regional state estimate for use in Arctic inter-annual to decadal climate research, covering the early 21st century, culminating in the Arctic Subpolar gyre sTate Estimate (ASTE).

Here we describe the first release of ASTE (*ASTE_R1*), providing an estimate of the ocean-sea ice state for the period 2002–2017. We describe the model configuration, observational constraints and the state estimation machinery (section 2) and present the model-data misfit reduction (section 3). We then compare our estimates of volume, heat and freshwater transports through important Arctic gateways with those in the existing literature as well as present an analysis of *ASTE_R1* heat and freshwater budgets for the Arctic Ocean, Greenland-Iceland-Norwegian (GIN) Seas and subpolar North Atlantic (section 4). In section 5 we examine how an improved fit is achieved, identifying key adjustments of our independent control variables, and review remaining issues in *ASTE_R1* . In section 6 we summarize key findings and discuss future directions.

2 Methodology

2.1 Model Description

The coupled ocean-sea ice model underlying the estimation framework is an evolved version of the Massachusetts Institute of Technology general circulation model (MITgcm; Marshall et al., 1997; Adcroft et al., 2018). The model solves the primitive equations in rescaled z^* coordinates (Adcroft & Campin, 2004) with a full non-linear free surface (Campin et al., 2004). The dynamic-thermodynamic sea ice model is an evolved version of Menemenlis et al. (2005); Losch et al. (2010); Heimbach et al. (2010). Eddy-induced tracer mixing and transports along isopycnal surfaces are parameterized following Redi (1982); Gent and McWilliams (1990).

The model uses a finite-volume discretization in a so-called "latitude-longitude-polar-cap" grid configuration (LLC grid, Forget et al., 2015a). The LLC grid is topologically equivalent to a cubed-sphere grid (Adcroft et al., 2004), but reverts to a regular latitude-longitude grid equatorward of ∼57°N. The computational cost associated with solving the non-linear optimization problem for eddy-resolving simulations, which would require resolutions well below 4–15 km for the Arctic Mediterranean (Nurser & Bacon, 2014), is prohibitively high. As a compromise, ASTE is based on the medium-resolution LLC-270 grid, providing a nominal grid spacing of 1/3°, which corresponds to ∼22 km in the North Atlantic, ∼16 km in the Nordic Seas, and ∼14 km in the high Arctic interior (Fig 3).

The ASTE domain covers the entire Atlantic northward of 32.5°S, the entire Arctic and its surrounding seas (Labrador, Nordic, Barents, Bering north of 47.5°N) and the Canadian Archipelago. The model has 50 unevenly spaced vertical height levels; thicknesses range from 10 m at the surface to 500 m at 5000 m depth. The 10 m thickness at the surface cannot fully resolve surface boundary layer processes or the shallowest summer mixed layer of ∼5 m, but is deemed sufficient for capturing the 10–100 m seasonal MLD in the Arctic (Rudels et al., 2004; Rudels, 2015; Peralta-Ferriz & Woodgate, 2015; Bigdeli et al., 2017) and is a reasonable choice given the size and expense of our computations. Partial cells (Adcroft et al., 1997) are used to improve the representation of topography. The domain has boundaries at 35°S in the South Atlantic, 48.6°N in the Pacific, and at the Gibraltar Strait. Rationales for choosing a full Atlantic-Arctic domain for ASTE – rather than limiting it to the Arctic Mediterranean – are to extend the applicability of the solution to investigation of latitudinal connectivity between Atlantic and Arctic variability on decadal timescales, and to displace the imposed open boundary conditions far from the region of key interest.

We prescribe lateral open boundary conditions from the global ECCOv4r3 solution, which has been shown to be in good agreement with large-scale constraints from satellite and in situ data (including Argo). The bathymetry is a merged version of W. Smith and Sandwell (1997), version 14.1, below 60°N and the international bathymetric chart of the Arctic Ocean (IBCAO, Jakobsson et al., 2012) above 60°N, blended over a range of ± 100 km about this latitude. Special attention was paid to remove abrupt jumps over the merged region. Model depths within important canyons (e.g. Barrow) and across important gateways (e.g., Florida Straits, Greenland-Iceland-Faroe-Scotland ridge, Aleu-

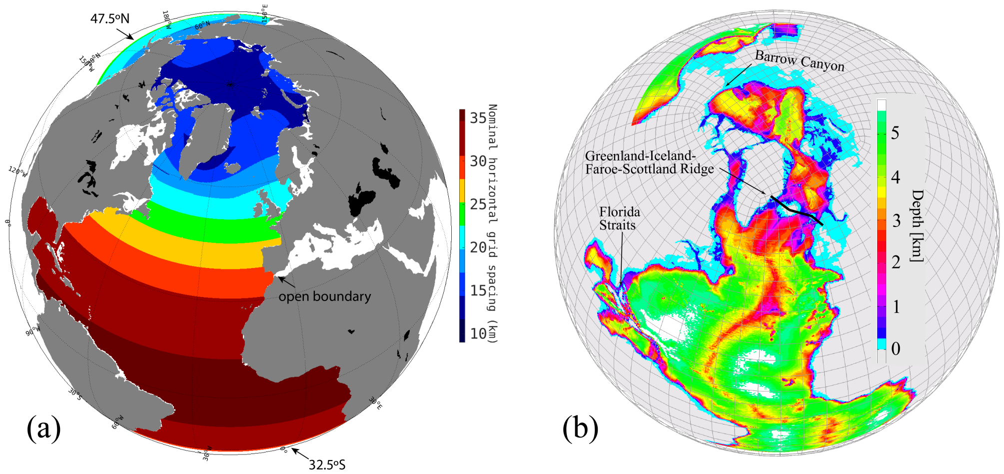

Figure 3. (a) Nominal horizontal grid spacing (km) and (b) the bathymetry in ASTE. The lateral open boundaries of the ASTE domain are at 47.5°N in the North Pacific, 32.5°S in the South Atlantic, and at the Gibraltar Strait. White areas in (a), which include the Hudson Bay, Baltic Sea, White Sea, Gulf of St. Lawrence, and all channels in the Canadian Arctic Archipelago except Nares and Barrow Straits, are masked. Depths of several important channels, including the Barrow Canyon, Greenland-Iceland-Faroe-Scotland Ridge and the Florida Straits, were carefully inspected to ensure transports consistent with published observations.

tian islands chain, Gibraltar Strait) were enforced to be consistent with observations in order to realistically simulate key transports and regional circulations.

Atmospheric forcing is applied via bulk formulae (Large & Yeager, 2008) over the open ocean, with the initial estimate of the atmospheric state variables from JRA-55 (Kobayashi et al., 2015). We considered taking ERA-Interim (Dee et al., 2011) – employed by ECCOv4r3 (Forget et al., 2015a; Fukumori et al., 2018a) – as our first guess. However, this product has a well documented warm bias of up to 2°C in the Arctic (Beesley et al., 2000; Freville et al., 2014; Jakobson et al., 2012; Lupkes et al., 2010) that causes excessive sea ice melt. ECCOv4r3 accommodated this warm bias through increased sea ice and snow wet albedos. Nguyen et al. (2011) showed reasonable modeled sea ice concentration and thickness using the Japanese Reanalysis (JRA-25) without the need to increase sea ice albedos above their observed values. For this reason, the updated three-hourly, higher-resolution JRA-55 was chosen as the initial surface boundary forcing. Monthly-mean estuarine fluxes of freshwater are based on the Regional, Electronic, Hydrographic Data Network for the Arctic Region (R-ArcticNET) dataset (Lammers & Shiklomanov, 2001; Shiklomanov et al., 2006).

As shown in Fig. 2 the ECCOv4r3 solution does not exhibit the cyclonic circulation of Atlantic water in the Arctic that is inferred from hydrographic observations (Rudels, 2012). For this reason, we elected to initialize from alternative products. Table 1 summarizes our first-guess model input parameters for sea ice, ocean mixing and momentum dissipation, along with our choice of ocean-sea ice state to initialize the unconstrained simulation. This run serves as iteration 0 of the optimization and will be referred to as *it0* for the remainder of the paper. Our selection is informed by existing observation/model-based estimates. Importantly, sea ice albedos and drag coefficients are chosen within the range of observed and previously optimized estimates Nguyen et al. (2011).

The three-dimensional parametric horizontal stirring fields for temperature and salinity are based on typical values used in the literature (Pradal & Gnanadesikan, 2014; Campin,

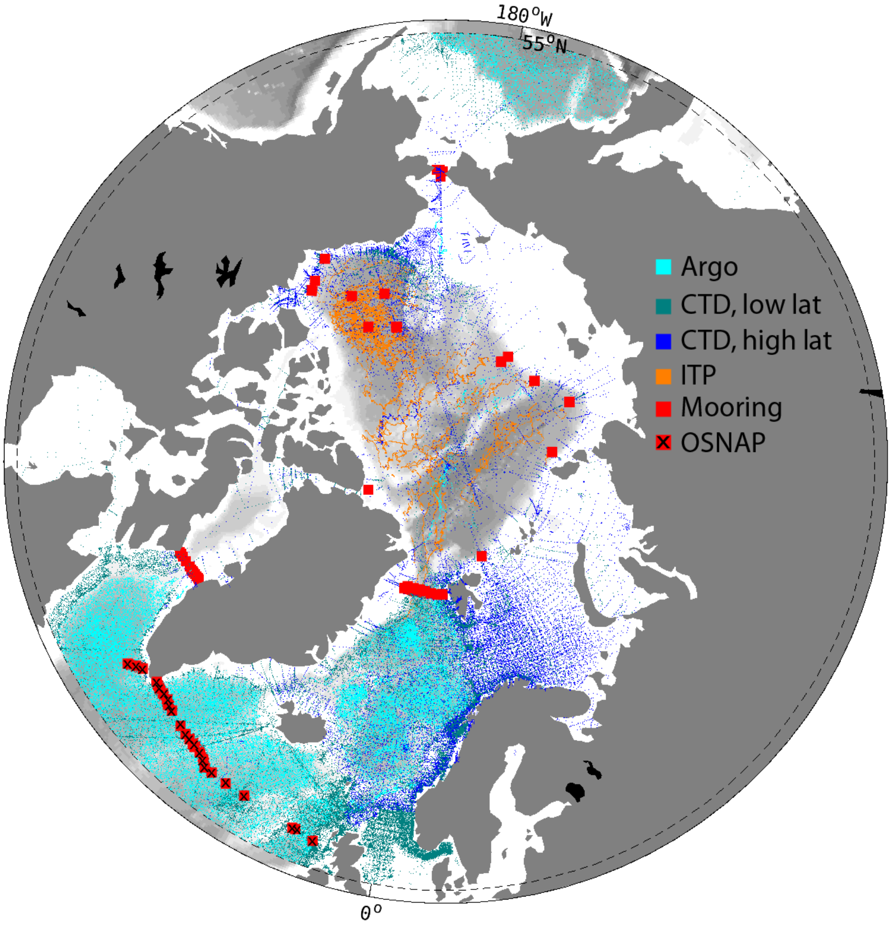

Figure 4. In situ observations used to constrain ASTE. Red squares with "x" are additional OSNAP mooring data, used for independent evaluation but not part of the cost function.

2014, *pers. comm.*) with consideration for where the ASTE grid resolves the baroclinic deformation radius as follows. The vertical background diffusivity $\mathcal{K}_d$ was set based on typical values at latitudes below 79°N of $\sim 10^{-5}$ m^2/s and limited observed and modelled ranges of 10^{-7} to 10^{-6} m^2/s at high latitudes (Padman & Dillon, 1988; Zhang & Steele, 2007; Nguyen et al., 2011; Fer, 2014; Sirevaag & Fer, 2012; Cole et al., 2014). Vertical diffusivities are enhanced by a factor of 10 near the sea floor to mimic lee wave-driven mixing (Toole, 2007; Mashayek et al., 2017). Horizontal dissipation is applied as a combination of biharmonic Leith and Laplacian viscosity (Griffies, 2004; Fox-Kemper & Menemenlis, 2008). At lower latitudes, where eddy effects are better resolved, we follow the formulation of Leith (1996) to represent the direct enstrophy cascade at mesoscales. Within the attached Gulf Stream, a higher Laplacian viscosity is initially required to reduce the Reynolds number and prevent premature separation (Dengg, 1993; Chassignet & Garraffo, 2001; Chassignet & Marshall, 2013). In the Arctic Mediterranean, where the deformation radius is 4–10 km, an ad-hoc combination of biharmonic Leith and Laplacian vicosity is used to ensure consistency of inflow velocity at Fram Strait and an approximate cyclonic circumpolar AW circulation inside the Arctic (Jochum et al., 2008, see Table 1). The model is spun up for 6 years using repeated year 2002 atmospheric forcing and open boundary conditions (Table 1). The ocean, sea ice and snow states at the end of this 6 year spin up became the initial condition for the unconstrained *it0* in the optimization procedure described next.

Field	Value	Reference	Note
Unconstrained run (*it0*)			
Ocean-sea ice state for Jan/2002 obtained after 6-yr spin up from:			
θ_0	WOA09	Locarnini et al. (2010)	Temperature
S_0	WOA09	Antonov et al. (2010)	Salinity
$\mathbf{u}_0$	0.0	–	Ocean velocity
A_{SI_0}	PIOMAS	Zhang and Rothrock (2003)	Sea ice concentration
h_{SI_0}	PIOMAS	Zhang and Rothrock (2003)	Sea ice thickness
$\mathbf{u}_{SI_0}$	0.0	–	Sea ice velocity
Sea ice parameters:			
$\alpha_{SI_{wet,dry}}$	0.7, 0.68	Johnson et al. (2007)	sea ice albedo
$\alpha_{sn_{wet,dry}}$	0.84, 0.77	Johnson et al. (2007)	snow albedo
$C_{da,dw}$	0.00114, 0.0054	Nguyen et al. (2011)	sea ice-[air,ocean] drag
Mixing and dissipation parameters:			
$\log_{10}(\mathcal{K}_z)$	−6.5 to −6.0	Nguyen et al. (2011) Zhang and Steele (2007) Padman and Dillon (1988) Sirevaag and Fer (2012); Fer (2014)	Below 50 m in eastern Arctic & below 75 m in western Arctic
	−5	Munk (1966)	Outside the Arctic & near surface in the Arctic
	value plus 1	Mashayek et al. (2017)	Grid points next to land
$\mathcal{K}_\sigma$	50 17	Pradal and Gnanadesikan (2014)	South of 60°N North of 60°N
$\mathcal{K}_{gm}$	50 50	Pradal and Gnanadesikan (2014)	South of 60°N North of 60°N
ν	Leith	Leith (1968)	Ocean interior
	Ah=0.0005 Ah=0.003	Forget et al. (2015a)	Coastal south of 40.5°N Coastal north of 40.5°N
Optimized run (*ASTE_R1*)			
$\theta_0, S_0, \mathcal{K}_\sigma, \mathcal{K}_{gm}$, $\log_{10}(\mathcal{K}_z)$: optimized.			
$\alpha_{SI_{wet,dry}}, \alpha_{sn_{wet,dry}}, C_{da,dw}, \mathbf{u}_0, A_{SI_0}, h_{SI_0}, \mathbf{u}_{SI_0}$: same as *it0*			
ν	Leith	Leith (1968)	South of [70,73]°N in [Pacific, Atlantic] sector
	Ah=0.0054	Griffies (2004)	North of [70,73]°N in [Pacific, Atlantic] sector

Table 1. Values of initial ocean and sea ice state, sea ice parameters, and ocean mixing and dissipation for the unconstrained run *it0* and optimized *ASTE_R1* solution. ν is either the biharmonic (m^4/s) or harmonic (m^2/s) viscosity, and Ah is the harmonic viscosity coefficient (Griffies, 2004). Units for the mixing coefficients $\mathcal{K}_{[\sigma,gm,z]}$ are m^2/s

.

2.2 State Estimation Framework

ASTE is formally fit to observations through a gradient-based iterative least-square minimization of the model-data misfit function that takes into account data and model parameter uncertainties (Nguyen et al., 2017). The gradient with respect to a high-dimensional space of uncertain input variables, the "controls", is obtained via the adjoint of the model, derived by means of algorithmic differentiation (AD; Giering et al., 2005; Heimbach et al., 2005). The model-data misfit (or "cost") function is defined as (Wunsch & Heimbach, 2007):

$$\begin{aligned} J \;=\; & \sum_{t=t_0+\Delta t}^{t_f} [\,\mathbf{y}(t) - \mathbf{E}(t)\mathbf{x}(t)\,]^T\,\mathbf{R}(t)^{-1}\,[\,\mathbf{y}(t) - \mathbf{E}(t)\mathbf{x}(t)\,] \\ & + [\,\mathbf{x}_0 - \mathbf{x}(t_0)\,]^T\,\mathbf{B}(t_0)^{-1}\,[\,\mathbf{x}_0 - \mathbf{x}(t_0)\,] \\ & + \sum_{t=t_0}^{t_f-\Delta t} \mathbf{u}(t)^T\mathbf{Q}(t)^{-1}\mathbf{u}(t) \end{aligned} \tag{1}$$

where time $t \in [t_0, t_f]$, t_0 and t_f are the initial and final time, and Δt the time-stepping of the forward model. $\mathbf{y}(t)$ is the observation vector and $\mathbf{x}(t)$ the state vector containing the model ocean (e.g., temperature, salinity, velocities, sea surface height) and sea ice variables (e.g., concentration, ice and snow thickness, velocities) at all grid points (Wunsch & Heimbach, 2007). The combined initial model state $\mathbf{x}_0$ and input parameter adjustments $\mathbf{u}(t)$ collectively comprise the control vector $\boldsymbol{\Omega} \ni \{\mathbf{x}_0,\mathbf{u}(t)\}$. $\mathbf{E}$ is the operator mapping the state variables to the observations. The model-data misfit $\mathbf{y}(t)-\mathbf{E}(t)\mathbf{x}(t)$ is weighted by the inverse error covariance matrix $\mathbf{R}(t)$. This accounts for both observational uncertainty and model representation error, where the latter considers the extent to which real variability cannot be represented at the chosen model resolution (Nguyen et al., 2020a). $\mathbf{B}(t_0)$ and $\mathbf{Q}(t)$ are error covariances of $\mathbf{x}_0$ and $\mathbf{u}(t)$, respectively. Full knowledge of $\mathbf{R}$, $\mathbf{B}$, and $\mathbf{Q}$ is often unattainable (Wunsch & Heimbach, 2007). As a result, the misfit $\mathbf{y}(t)-\mathbf{E}(t)\mathbf{x}(t)$ and variables $\boldsymbol{\delta}\mathbf{x}_0 = \mathbf{x}_0-\mathbf{x}(t_0)$ and $\mathbf{u}(t)$ are often assumed Gaussian, with zero means and standard deviations whose squares fill the diagonal entries of their respective covariance matrices (Wunsch & Heimbach, 2007). In the absence of better information, we resort to the simplified representation of the error covariances, consistent with existing state estimation efforts (e.g., Mazloff, Heimbach, & Wunsch, 2010; Forget et al., 2015a; Fukumori et al., 2018a). These error estimates play an important role in any least squares optimization (both ECCO-related and other data assimilation efforts), and their improved estimation is itself an important area of ongoing research (Wunsch, 2018). We will discuss these further below.

There are three distinct contributions to the misfit cost function, eqn. (1). The first term describes the normalized model-data squared misfit to be minimized. This term sums weighted contributions from all observational data considered. The second term penalizes deviation of the initial state $\mathbf{x}(t_0)$ from the initial guess $\mathbf{x}_0$ (Table 1). Similarly, the third term describes moderation of input parameter adjustments $\mathbf{u}(t)$ so that the adjustment amplitude does not far exceed the uncertainties. The adjoint (or Lagrange multiplier) method consists of augmenting the cost function (eqn. (1)) to a Lagrangian function $\mathcal{L}$ by adding an additional term that enforces the strict adherence of the solution to the model equations. In this manner, the constrained optimization problem (find extrema of J subject the constraint that the model equations be fulfilled exactly) is converted into an unconstrained problem of finding stationary points of the Lagrangian (Wunsch & Heimbach, 2007).

The optimization problem is solved via gradient-based optimization, in which the gradient of the cost function with respect to the control variables informs an iterative minimization algorithm. In our case, this is the quasi-Newton method following Gilbert and Lemaréchal (1989). Once the cost function J is defined, beneficial control adjustments that reduce the misfit are informed by the gradient $\nabla_\Omega J$. This gradient can be efficiently computed for very high-dimensional control spaces using the adjoint model (Wunsch & Heimbach, 2007). These adjusted controls are then used in a new integration of the forward model for the full period (2002–2017), during which model-data misfits are recomputed. At the end of this forward integration, contributions to the cost-function are accumulated, the adjoint model is integrated, and the gradient information is re-computed informing updated control adjustments for the next integration of the forward model. The optimization thus proceeds in an iterative manner, whereby each iteration entails execution of both the forward and adjoint model, providing updated control adjustments to obtain further reduction of the total model-data misfit in successive iterations. The optimization is continued until little further misfit reduction is achieved between successive iterations. This is expected when the state estimate is in agreement with the observations within the error $\mathbf{R}(t)$ (expressed, e.g., in terms of a χ^2 distribution of the squared normalized misfit residuals).

The space of control variables for ASTE, $\{\mathbf{x}_0, \mathbf{u}\} \in \mathbf{\Omega}$, comprises the 3D hydrographic initial conditions, potential temperature and salinity (θ_0, S_0), the time-varying 2D surface atmospheric state variables, spatially-varying but temporally invariant model coefficients of vertical diffusivity ($\mathcal{K}_z$) and parameterized eddy activity ($\mathcal{K}_\sigma, \mathcal{K}_{gm}$), denoting the strength of eddy-induced isopycnal diffusivity and potential energy transfer, respectively (Forget et al., 2015b). The atmospheric state control variables are 2 m air temperature, T_{air}, specific humidity, q_{air}, downward short- and long-wave radiation, R_{sw}, R_{lw}, precipitation, P, and 10 m winds u_w, v_w. Although runoff and evaporation are not control variables, in practice they project onto the precipitation sensitivities, interpreted as the linear combination of net surface freshwater fluxes (evaporation minus precipitation minus runoff, E-P-R).

To ensure the adjustments are physically reasonable, *a-priori* uncertainties (i.e. the square-roots of the diagonal terms of $\mathbf{B}$ and $\mathbf{Q}$) are estimated following Forget and Wunsch (2007); Fenty and Heimbach (2013a); Fukumori et al. (2018b) for oceanic hydrography and Chaudhuri et al. (2013, 2014) for atmospheric forcing. Whilst the estimate from Forget and Wunsch (2007) and Fenty and Heimbach (2013a) quantifies climatological variability, the additional contribution from Fukumori et al. (2018b) accounts for model representation error inferred from a high resolution (1/48°) simulation to estimate unresolved variance in ASTE. Uncertainties in the atmospheric state as derived by Chaudhuri et al. (2013, 2014) are based on the spread between atmospheric reanalysis products, which is particularly large over the Arctic.

The vector $\mathbf{y}(t)$ contains as many available ocean and sea ice observations as we were able to access. The observational backbone of *ASTE_R1* includes the standard ECCOv4r3 suite (Table A1) of in situ and remotely-sensed ocean data: temperature and salinity profiles from Argo, GO-SHIP and other research cruises, instrumented pinnipeds, gliders, and moorings, and ice-tethered profilers; ocean bottom pressure anomalies from GRACE (Watkins et al., 2015; Wiese et al., 2018); sea surface height from Ocean Surface Topography Mission/Jason 2 and Jason 3 (Zlotnicki et al., 2019); Mean Dynamic Topography DTU13 (Andersen et al., 2015); and infrared and microwave-derived sea surface temperature (JPL_MUR_MEaSUREs_Project, 2015). For details on how the data and their uncertainties were obtained and prepared we refer the readers to Fukumori et al. (2018b). In addition to the ECCOv4r3 suite, the data are augmented by updated high latitude in situ profiles, ship-based CTD, and mooring observations at important Arctic gateways and in the Arctic interior (see Table 2, Fig. 4).

The estimation period chosen for ASTE, 2002–2017, leverages the increase in satellite (GRACE, ICESat-1/2, CryoSat-2) and in situ (ITP) observations in the Arctic, as well as the beginning of the quasi-global Argo float deployment. In total, approximately 1.2×10^9 observations were employed to constrain distinct aspects of the modeled ocean

Data Type	**Spatial coverage**	**Temporal coverage**	**Description**	**Source**
		Sea ice		
Velocity[1]	N.Hemis	2002–2012	passive microwave & AVHRR & IABP	*rkwok.jpl.nasa.gov/radarsat/3dayGr_table.html* *nsidc.org/data/docs/daac/nsidc0116_icemotion.gd.html* Kwok and Cunningham (2008), Fowler et al. (2013)
	N.Hemis	2012–2015	ASCAT & SSMI	*ftp.ifremer.fr/ifremer/cersat/products/gridded/psi-drift*
Thickness[1]	N.Hemis	2011–2017	CryoSat-2	*www.meereisportal.de/datenportal.html* & Ricker et al. (2017)
	N.Hemis	2010–2017	SMOS	*icdc.zmaw.de/l3c_smos_sit.html* & Tian-Kunze et al. (2014)
	N.Hemis	2003–2008	ICESat	*rkwok.jpl.nasa.gov/icesat/index.html* & Kwok and Cunningham (2008); Kwok et al. (2009)
Concentration	N.Hemis	2002–2017	SSMI & OSISaf	*osisaf.met.no/p/ice/index.html* & Lavergne et al. (2019)
		Ocean		
ITP (T,S)	Arctic	2004–2017	Profilers	*www.whoi.edu/itp/data/* Krishfield et al. (2008), Toole et al. (2011); Krishfield (2020),
Hydrographic Survey (T,S)	GINs	2002–2006	ASOF	*www.pangaea.de/*
	Beaufort Sea	2003–2017	BGOS	*www.whoi.edu/beaufortgyre/home/*
	Laptev Sea	2002–2003		*doi.pangaea.de/10.1594/PANGAEA.761766* & Bauch et al. (2009)
	East Arctic	2007		*doi.pangaea.de/10.1594/PANGAEA.763451* & Bauch et al. (2011)
	GINs	2002–2013		Våge et al. (2015)
Mooring (T,S,currents)	Fram Strait	2002–2017	ASOF	Fahrbach et al. (2001), Beszczynska-Möller et al. (2012)
	East Arctic	2002–2015	NABOS	*nabos.iarc.uaf.edu/*,Pnyushkov et al. (2013) and
	West Arctic	2002–2015	CABOS	Polyakov et al. (2012)
	Beaufort Gyre	2004–2017	BGOS	*www.whoi.edu/website/beaufortgyre/data*
	Bering Strait	2002–2017		*psc.apl.washington.edu/HLD/Bstrait/Data/* & Woodgate (2018)
	Davis Strait	2004–2015		*iop.apl.washington.edu/data.html*, Curry et al. (2011)
Transports[1] of Vol & Heat & Freshwater	Fram Strait	2002–2017	ASOF	Schauer and Fahrbach (2004) & Beszczynska-Möller et al. (2012)
	Bering Strait	2002–2017	mooring	Woodgate (2018)
T,S	High Latitude	2002–2015	IARC	*oregon.iarc.uaf.edu/dbaccess.html*
			IARC	*climate.iarc.uaf.edu/geonetwork/srv/en/main.home*
			ICES	*ocean.ices.dk/HydChem/HydChem.aspx?plot=yes*
			SBI	*www.eol.ucar.edu/projects/sbi/*
	CAA	2002–2015	BIO	*www.bio.gc.ca/science/data-donnees/base/run-courir-en.php*
	Arctic	2002–2015	ACADIS	*www.aoncadis.org/home.htm*
	Arctic	2002–2015	WHOI	(Krishfield, 2020)

Table 2. Satellite and *in situ* data used to constrain or assess ASTE in addition to the ECCOv4r3 dataset. [1]Datasets that are used only for assessment and not part of the cost function.

and sea-ice state, culminating in the optimized *ASTE_R1* solution. Key among these are satellite-based observations of sea level anomalies (SLA) to aid removal of the precipitation bias in JRA-55, Argo and lower latitude CTD to improve surface and sub-surface hydrography in the North Atlantic and Nordic Seas, and a suite of moorings in the Arctic. This suite includes the Fram Strait mooring array to constrain the boundary current strength and heat flux from the Nordic-Seas into the Arctic, and the combined ITP and Beaufort Gyre moorings to constrain the Canada Basin hydrography. Finally, OSISaf daily sea ice concentration was essential for constraining the ice edge and upper ocean hydrography in the Arctic and its surrounding marginal seas.

The error $\mathbf{R}$ associated with the observations $\mathbf{y}(t)$ is the combined data uncertainty and model representation error. For hydrographic data, the derivation is as described above for the *a-priori* uncertainties $\mathbf{B}$. For satellite data, errors are a combination of the corresponding satellite mission's provided uncertainty and model representation errors, as described in (Fukumori et al., 2018b). These representation errors were derived from the data variance within (and weighted by the area of) ASTE horizontal grid box. They generally exceed the stated mission uncertainty. As seen in eqn. (1), $\mathbf{R}$ plays an important role in weighting the individual model-data misfit terms. Careful assessment of $\mathbf{R}$ is thus required to ensure an appropriate and balanced contribution of the diverse datasets to the total J.

The practical implementation of eqn. (1) follows that described in Forget et al. (2015a). Several approximations to parameterization in the adjoint model were made to ensure stable behaviour. Maximum isopycnal slopes are limited in the GM/Redi parameterization, the vertical mixing scheme (K-Profile Parameterization, Large et al., 1994) is omitted in the adjoint, and increased horizontal and vertical momentum dissipation are employed in the adjoint to suppress fast growth of unstable sensitivity.

The full sea ice adjoint, as described in Fenty and Heimbach (2013a); Fenty et al. (2015), was not used in this study (nor in ECCOv4), due to persistent instability issues. In its place, the sea ice concentration model-data misfit is used to relate air-sea fluxes to the enthalpy of the integrated surface ocean-sea ice system as follows. Where the model has an *excess/deficiency* of sea ice, extra heat is added to, or removed from the system to bring the sea surface to above or below the freezing temperature. In these two cases, the pseudo-sea ice cost function contributions $J_{\mathtt{seaice\_conc\_[ex,de]}}$ are in enthalpy units rather than normalized model-data misfits. Normalization is chosen to obtain amplitudes comparable to other model-data misfits J_i contributing to the total cost function J, so that these terms play an active role in the optimization. Lastly, convergence – if achievable for these two pseudo-sea ice costs – is when they approach zero and not unity.

After 62 iterations, a substantial reduction in model-data misfit has been achieved compared to the unconstrained simulation, such that the solution is deemed suitable as ASTE first release. The initial conditions of the optimized state, ASTE Release 1 (*ASTE_R1*), are derived by adding the adjustments $[\,\Delta\theta,\,\Delta S\,]_{i62}$ to the first guess fields $[\,\theta,\,S\,]_{i0}$. The same holds for the optimized mixing fields and surface atmospheric state (see Table 1). Adjustments to the uncertain control variables obtained as a result of the gradient-based optimization enable the improvement in the model fit to observations while retaining dynamical consistency. Fig. 5 shows the uncertainty and adjustments for four of the seven surface atmospheric state variables, T_{air}, R_{sw}, R_{lw}, and v_w. The uncertainty, derived from Chaudhuri et al. (2013, 2014), shows some of the largest disagreements amongst the atmospheric reanalyses to be in the Arctic (Fig. 5a1–a4). The percentile (pctl) thresholds indicate that for these four fields the adjustments are within the uncertainty. Overall, the 99-pctl adjustments are within $2\,\sigma$ for all time-dependent atmospheric variables except downward shortwave where it is within $3\,\sigma$.

The full monthly mean state of *ASTE_R1* is distributed via the ECCO & ASTE data portal at the Texas Advanced Computing Center (TACC). In addition, the model

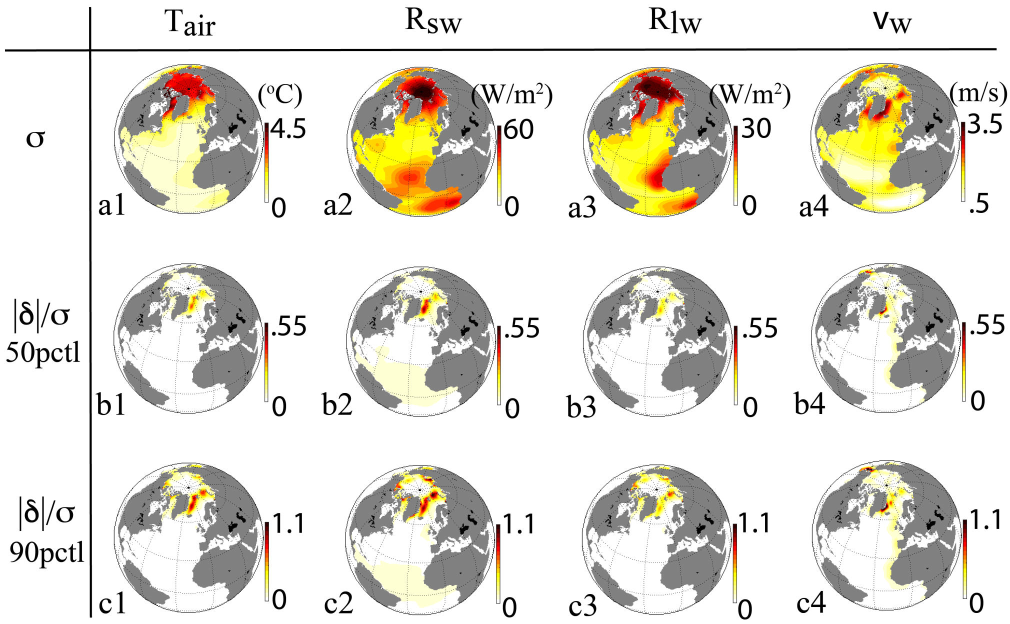

Figure 5. The atmospheric forcing field (a1–a4) uncertainty σ and (b1–b4) the 50-percentile and (c1–c4) 90-percentile normalized adjustment magnitudes $|\delta|/\sigma$. The uncertainty fields have units given above the color scale for a1–a4. Note that the reciprocal of the squared value of these uncertainties are entries in the weight matrix **Q**. The normalized adjustment magnitudes are dimensionless.

configuration, required input fields and code are distributed to enable reruns (see Appendix A). Since the focus of ASTE is on the North Atlantic and the Arctic Ocean, we restrict both the discussion presented below and the distributed *ASTE_R1* fields to latitudes above 10°N. As for ECCOv4r3, the mass, salt, and heat budgets in *ASTE_R1* are accurately closed when computed using the distributed standard ECCO diagnostics that we provide. In Appendix B, we show how lateral transports may be accurately computed and provide estimates for the errors incurred in offline calculations using the *ASTE_R1* monthly mean diagnostics.

2.3 Making Meaningful Model-Observation Comparisons

A meaningful assessment of *ASTE_R1* through comparison with observations is nontrivial and requires careful consideration. One of the biggest challenges is properly accounting for the sparse spatio-temporal sampling and the potential for aliasing. For example, measurements might only be taken at a discrete location (e.g. a mooring) or along-track (i.e., with high along-track coverage and drastically lower resolution in the cross-track direction) or only during summer months (e.g., ship-based CTD). "Averages" of these measurements (e.g., average Argo or ITP data over 1 month or 1 year) incur aliasing in both space and time as well as potential spatial or seasonal biases. "Averages" of *ASTE_R1* outputs at the smallest spatial scale (grid cell size), on the other hand, are over a spatial area of ~ 200 km^2. Unless observations are well sampled over this grid-area, a direct comparison between observations and *ASTE_R1* can be problematic. Furthermore, *ASTE_R1* does not resolve eddies in the Arctic and GIN Seas. As a result, we should neither expect nor demand a perfect fit to discrete (in space/time) measurements. As is common in data assimilation (Janjić et al., 2017) the ECCO framework utilizes "representation errors" - described above - in the weighting of the model-data misfits, eqn. (1), to safeguard against over-fitting and facilitate more meaningful model-data comparison (Wunsch & Heimbach, 2007). However, these representation errors are themselves highly uncertain, often relying on unconstrained high-resolution model runs from which they are inferred (see Nguyen et al., 2020a, for a more detailed discussion).

In Section 3 we present both normalized misfit reductions as well as comparisons of dimensional transports and heat/freshwater contents. For the dimensional quantities, we encounter several potential challenges related to resolution and bias issues, which we briefly discuss in the following. A serious challenge stems from the need to compare watermasses in the presence of hydrographic biases. From observations, watermasses are often defined in temperature, salinity, and density (T, S, σ) space with tight thresholds/bounds reflecting the measurement precision (e.g. to the first or second decimal place). These definitions can be problematic to adopt in *ASTE_R1* , where we are averaging over grid-cell areas of $\sim$200 km^2 and thicknesses of 10–500 m. Furthermore, in some regions the model representation errors may be up to an order of magnitude larger than measurement precision. In these regions, the normalized misfit can be within acceptable range, but *ASTE_R1* can still possess notable absolute (T, S, σ) biases if the representation errors are large. For this reason, a watermass is likely to exist in *ASTE_R1* but with modified thresholds/bounds. Where appropriate, we analyzed *ASTE_R1* carefully in (T, S, σ) space to identify suitable classifications for calculation of watermass transports. Details on the modified bounds are provided in Appendix C.

A second challenge is related to the region over which derived quantities are computed. In cases where these regions are defined with geographic bounds based on availability of observations rather than dynamical regimes, the equivalent derived quantities in *ASTE_R1* can be highly sensitive to small shifts in bounding region, especially when the grid resolution and uncertainties in the control input parameters (e.g., forcing, internal mixing) are taken into account. For this reason, we also explore the sensitivity of area/volume integrals to choice of geographical bounds in Appendix C.

Lastly, comparison of (dimensional) integrated transports can be problematic due to spatial sampling issues and representation error, preventing precise estimation of narrow boundary currents in *ASTE_R1* . An example is at Fram Strait, where the *ASTE_R1* grid cannot resolve the e-folding scale of the West Spitsbergen Current (Beszczynska-Möller et al., 2012). Enforcing fit to the observed mooring velocity would likely result in an overestimation of the net inflow volume transport here. In *ASTE_R1* , velocities at gateways were not employed as active constraints but were used for offline assessment of the derived transports. Ultimately, however, the spacing between discrete moorings offers incomplete information on the total volume transports across a given gateway, and existing observation-based estimates generally require various assumptions on spatial/temporal correlations in order to interpolate between the mooring measurements. As a result, our direct comparisons of *ASTE_R1* and observation-based transports presented below seeks consistency in terms of sign and order of magnitude rather than exact agreement of amplitude. This is especially true for assessment of *ASTE_R1* heat and freshwater transports, computed relative to the wide range of reference values used in the literature.

3 Model-data misfit reduction and residuals

In what follows, we will assess the *ASTE_R1* solution in the context of existing observation-based estimates of the circulation and hydrography in the Arctic. We first compare *it0* and *ASTE_R1* using the online and offline cost metrics described in Section 2 and listed in Table 3, and summarize the reduction in the integrated model-data misfits and costs achieved in the production of *ASTE_R1* . We then expand this discussion, considering the *ASTE_R1* fit to constraints in the Arctic, GIN Seas, and Subpolar North Atlantic (sections 3.1-3.3). Note that assimilation aids – but by no means guarantees – model-data consistency due

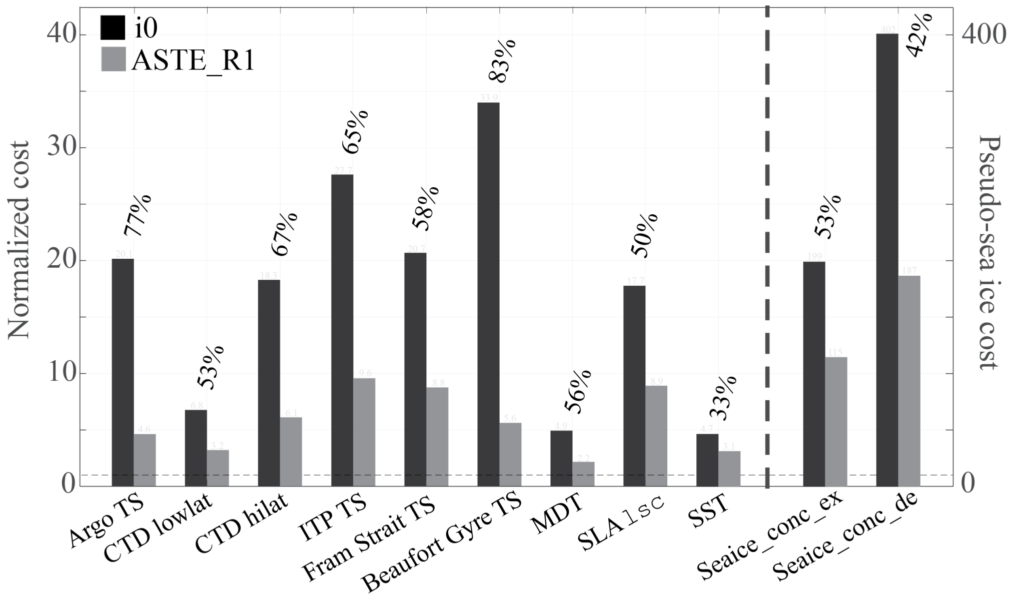

Figure 6. Aggregated cost reductions calculated from key data sets that were used in the optimization. The numbers listed above each data set are the percentage of cost reduction in *ASTE_R1* compared to *it0* . The magnitudes of the two pseudo-sea ice costs are indicated on the right abscissa.

to errors and/or deficiencies in the data, model, and/or state estimation framework. This point will be revisited in our discussion in section 5. We refer to "misfit" as the dimensional model minus data difference, "normalized misfit" as misfit scaled by the respective uncertainty (dimensionless), and "normalized cost" or "cost" as the square of the normalized misfit (dimensionless). The overall cost reductions in *ASTE_R1* have been grouped into several categories as shown in Fig. 6 and summarized in Table 3.

3.1 Arctic

3.1.1 Sea ice

Improved representation of sea ice extent in *ASTE_R1* (compared to the unconstrained simulation) is indicated by a significant reduction of $J_{\texttt{seaice\_conc}[\texttt{ex,de}]}$ by 53% and 42%, respectively (Table 3, Fig. 6). Fenty and Heimbach (2013b) showed that these improvements can be effectively achieved through small adjustments of atmospheric controls, within their uncertainty range. These improvements are independently confirmed by the reduction in offline misfits for sea ice area ($J_{\texttt{seaice\_area15}}$, 64%) and extent ($J_{\texttt{seaice\_extent15}}$, 83%) (Table 3). The largest improvements occur in the seasonal ice zones e.g., Greenland and Barents Seas and Southern Beaufort Gyre (Fig. 7a) associated with a systematic decrease in total simulated area/extent without alteration of the seasonal cycle (Fig. 7b).

The improved sea ice edge representation in *ASTE_R1* (Fig. 7e,h) is accompanied by a reduction in the offline misfits for sea ice velocities ($J_{\texttt{seaice\_vel}}$, Table 3), primarily in locations where nonzero ice velocities in *it0* were accompanied by observations of zero ice concentration and vice versa. Unlike velocity, however, the sea ice thickness costs $J_{\texttt{seaice\_thickness}}$ did not decrease (Table 3), primarily because the pseudo-sea ice adjoint does not contain physics relating ice thickness to the atmospheric forcing or ocean interaction from below. We will return to this in section 6.

Cost name	Normalized cost *it0*	Normalized cost *ASTE_R1*	Percentage reduction (%)
$J_{\texttt{Argo\_TS}}$	20.1	4.6	77
$J_{\texttt{CTD\_lowlat}}$	6.8	3.2	53
$J_{\texttt{CTD\_hilat}}$	18.3	6.1	67
$J_{\texttt{ITP}_{\texttt{TS}}}$	27.7	9.6	65
$J_{\texttt{FramStrait}_{\texttt{TS}}}$	20.7	8.8	58
$J_{\texttt{BeaufortGyre\_TS}}$	33.9	5.6	83
$J_{\texttt{BeringStrait\_TS}}$	6.3	4.2	33
$J_{\texttt{DavisStrait\_TS}}$	3.8	4.3	-11
$J_{\texttt{NABOS\_TS}}$	43.1	25.3	41
$J_{\texttt{StAnnaTrough\_TS}}$	22.9	7.2	69
$J_{\texttt{seaice\_conc\_ex}}$	402	187	53
$J_{\texttt{seaice\_conc\_de}}$	199	115	42
$J_{\texttt{SST\_[Reynolds+TMI/AMSRE]}}$	4.7	3.1	33
$J_{\texttt{MDT}}$	4.9	2.2	56
$J_{\texttt{SLA\_[gfo+ers+tp]}}$	2.7	1.4	49
$J_{\texttt{SLA\_lsc}}$	17.7	8.9	50
$J^{(o)}_{\texttt{seaice\_area15}}$	1.0	0.36	64
$J^{(o)}_{\texttt{seaice\_extent15}}$	1.0	0.17	83
$J^{(o)}_{\texttt{seaice\_thickness}}$	22.0	25.8	-17
$J^{(o)}_{\texttt{seaice\_UV}}$	2.1	1.6	23
$J^{(o)}_{\texttt{FramStrait\_vNorth}}$	1.3	1.0	26
$J^{(o)}_{\texttt{NABOS\_mmpUV}}$	2.0	1.6	23
$J^{(o)}_{\texttt{OSNAP\_TS}}$	6.3	3.5	44
$J^{(o)}_{\texttt{lineW\_TS}}$	3.3	2.5	26

Table 3. Active and offline costs and reductions in *ASTE_R1* compared to *it0* . The quantities listed above the triple horizontal lines contribute directly to the total J in eqn. (1), i.e., contribute to the gradient-based minimization, whereas those listed below the triple horizontal lines ($J^{(o)}$) are purely diagnostic, i.e. are used only for offline assessment and do not influence the optimization. The offline sea ice area and extent (both defined using the common 15% cutoff threshold) costs are normalized by the Arctic Mediterranean's area.

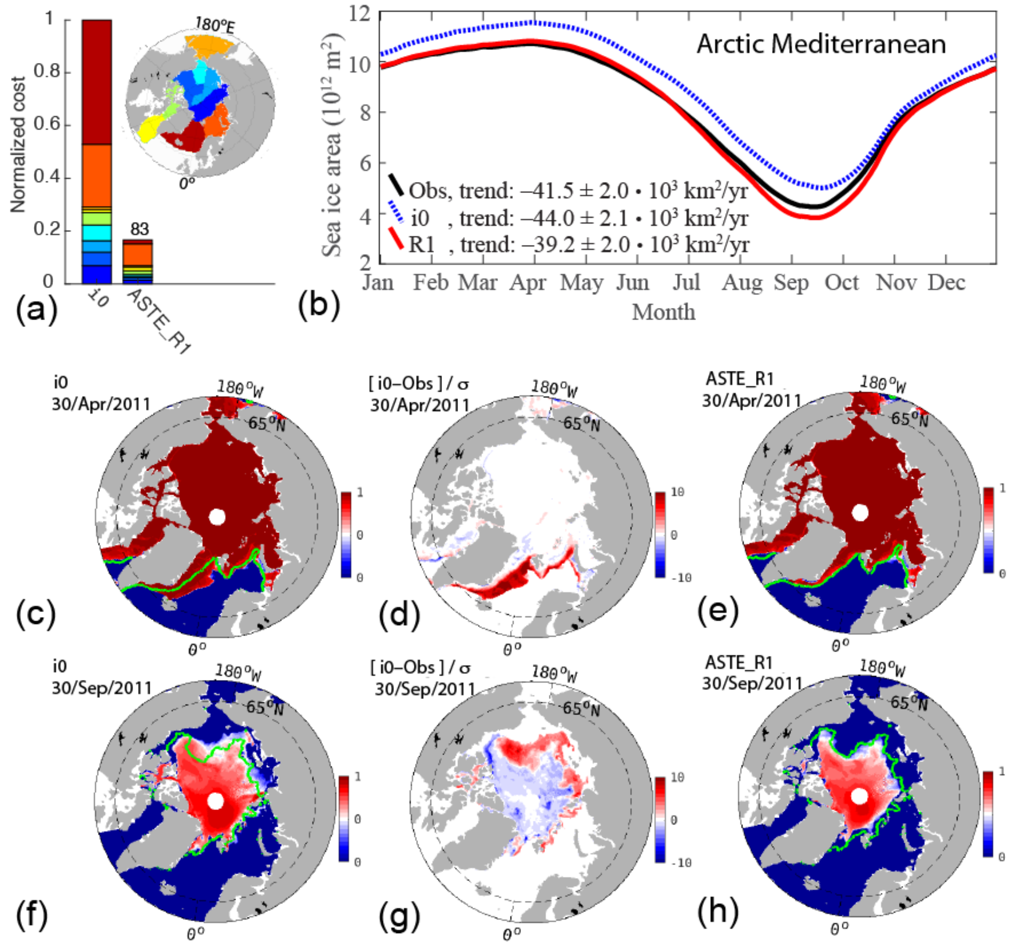

Figure 7. Comparison of sea ice misfits in the Arctic Mediterranean, for the unconstrained *it0* and the optimized *ASTE_R1* solution, assuming the standard 15% cutoff threshold for both total ice area and extent. (a) Comparison of cost (misfit squared) to observed sea ice extent, $J^{(o)}_{\texttt{seaice\_extent15}}$, showing contributions from individual basins. (b) Comparison of 12-month climatology of sea ice area, also showing observation-based climatology from OSSISaf (black). The climatology and the trends listed in the legend were derived from the 01/Jan/2002–31/Dec/2017 time-series. Comparison of daily sea ice concentration between *it0* (c,f), and *ASTE_R1* (e,h), for days selected at times of maximum (c,e) and minimum (f,h) ice extent. The green contour in panels (c,e,f,h) delineates the observed sea ice concentration from OSSISaf at the indicated dates. The optimization acts to reduce concentration at the ice margin where notable biases exist in *it0* . These biases are shown normalized by uncertainty in the OSSISaf observations for (d) 30/Apr/2011 and (g) 30/Sep/2011.

3.1.2 Fram Strait

The dynamics in the vicinity of Fram Strait are highly complex, governed by strong air-ice-ocean interaction, vigorous generation of eddies associated with highly sheared boundary currents and their recirculations in the presence of significant topographic steering (Beszczynska-Möller et al., 2012; de Steur et al., 2014; von Appen et al., 2015a, 2015b; Hattermann et al., 2016). Given the complexity and challenge to realistically simulate watermass properties and transports across this gate (e.g., Nguyen et al., 2011; Ilicak et al., 2016; Docquier et al., 2019) the Fram Strait moorings provide an invaluable constraint.

In view of the importance of AW for the wider Arctic region, we paid particular attention to skillfully represent AW inflow at Fram Strait as follows. Early in the development of *ASTE_R1* and prior to the gradient-based optimization, we compared the simulated volume transport to daily-average moored velocity (available for the years 2002–2011) at various depths along the entire array (Beszczynska-Möller et al., 2011, 2012). The model viscosity was prescribed (section 2.1, Table 1) to ensure we obtained a representative volume transport across the strait. During the iterative optimization, the mooring temperature and salinity were included in the active costfunction (J) to directly constrain T/S at the strait. Via these steps, indirect constraint of the tracer transports (i.e., $v * T$ and $v * S$) and their constituents (e.g., "inflow/outflow of AW") at Fram Strait was achieved, as shown by comparison to additional data for the years 2012–2017 (von Appen et al., 2015b) that were withheld from the optimization for offline evaluation.

Fig. 8 shows the unconstrained *it0* and *ASTE_R1* misfits to moored T, S, and northward velocity, as a function of longitude. For the region occupied by AW inflow, the normalized misfit in temperature is reduced by 71% compared to the unconstrained *it0* simulation (Fig. 8a). On the continental shelf, west of 4°W, *ASTE_R1* has a warm bias compared to the observations, which resulted in higher misfits here (red bar between longitude 8.1°W and 4.1°W in Fig. 8a). The reduction in misfits for inflow of the AW, however, is more important for the large-scale Arctic hydrography, as AW passing through this important gateway propagates along the entire boundary of the Eastern Arctic and into the Canada Basin. Here its properties can be compared to ITP data, which serve as the main constraint on subsurface T/S over the entire pathway from the Fram Strait (see section 3.2.3). The misfit reduction can be seen for one example mooring at approximately 8°E (Fig. 8d–f) at multiple depths. The significant improvement in salinity at the surface (dashed blue in Fig. 8e) is related to the improved ice edge (see also Fig. 7c–e). Another significant improvement is in the AW core temperature at depth ~ 250 m (solid blue and red lines in Fig. 8d).

3.1.3 Canada Basin hydrography

Once the AW, via the West Spitsbergen Current, crosses Fram Strait and traverses the Eastern Arctic along the continental slope (Rudels, 2015; Pnyushkov et al., 2018; Polyakov et al., 2017), the watermass properties (e.g., current strength and direction, density, temperature) are not as well constrained due to extreme data paucity in the Eastern Arctic. In particular, along the boundary current path (shoreward of the red contour in Fig. 9a), only 1% of the total 2004–2016 ITP data are acquired within the Nansen Basin; only 4.5% are acquired in the combined Amundsen and Makarov Basins (Fig. 9b–d). The majority of the ITP data (71%) are within the Canada Basin (Fig. 9e).

Fig. 10 shows the misfit reduction between the unconstrained *it0* and *ASTE_R1* as a function of basins and depths. The reduction is throughout the upper 800 m of the water column. Seawater density in the Arctic is primarily controlled by salinity, whereas temperature behaves more like a passive tracer and can be more flexibly impacted by the optimization procedure. As a result, the reduction in *ASTE_R1* temperature misfits greatly exceeds the reduction in salinity misfits in the Arctic, with the most notable

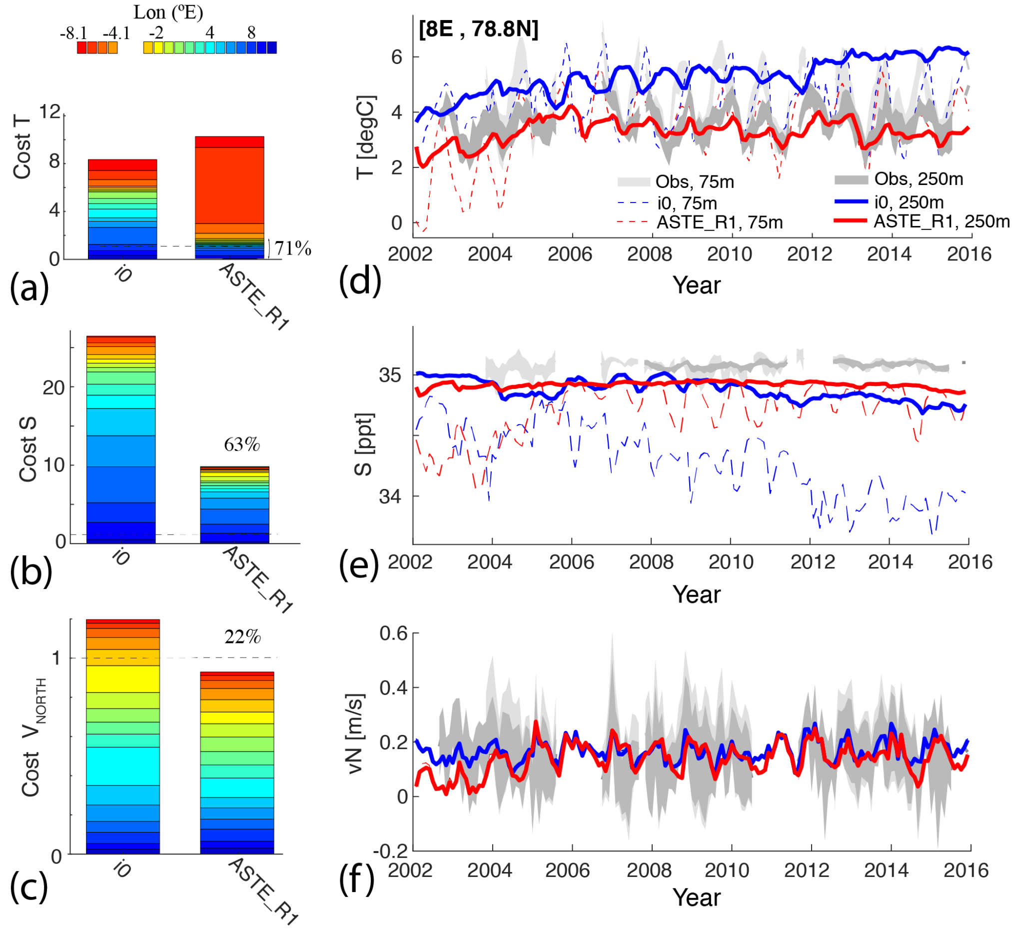

Figure 8. Normalized cost at Fram Strait for (a) temperature, (b) salinity, and (c) northward velocity between moored observations and unconstrained *it0* and *ASTE_R1* solutions, plotted as a function of longitude. Time series of (d) temperature, (e) salinity, and (f) northward velocity at one example mooring at [8°E,78.8°N] for depths 75 m and 250 m show that these properties are improved over the entire observed record. Grey envelopes in (d,e,f) show observed monthly-mean ± monthly-std values, with monthly values derived from the daily-mean values for each observed variable. Dashed lines in (a–c) delineate the normalized cost value of 1, targeted during the iterative optimization. Percentages listed in (a–c) are the cost reduction in (a) temperature, (b) salinity and (c) northward velocity. For (b-c) salinity and velocity, these cost reductions are summed across all longitudes, reflecting improvements across the entire mooring array. For (a) temperature, we see a degradation of the solution at the western end of the array during production of *ASTE_R1* , with a net cost increase of 23%. In this case, the 71% reduction in normalized cost cited is computed using only the eastern moorings, reflecting important improvements in the incoming Atlantic Water carried by the West Spitsbergen Current.

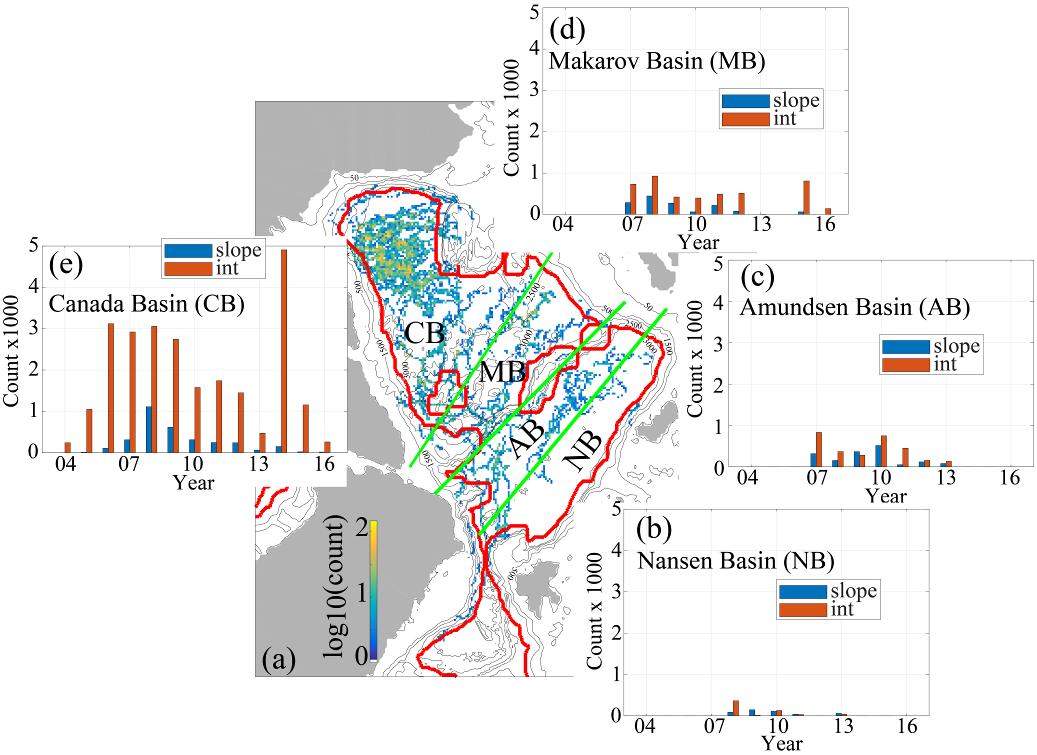

Figure 9. Distribution of ITP data as a function of year and geography. In (a), the red contour serves as a proxy for the separation between the continental shelf/slope (slope) and basin interior (int). It is defined as ∼100 km offshore of the 300 m isobath. The thick green lines approximately separate the Nansen Basin (NB), Amundsen Basin (AB), Makarov Basin (MB) and Canada Basin (CB). In (b)–(e), histograms of the number of ITP profiles for the continental shelf/slope (blue) and Arctic interior (orange) are normalized by the maximum number available for the Canada Basin (5000). The years of ITP data coverage are 2004–2016. There are a total of 39,904 ITP profiles.

improvement occurring within the AW core (120–450 m, Fig. 10a-c). The remaining notable temperature misfits in *ASTE_R1* are at depths occupied by the mixed layer (10–65 m) and below the AW core (450–800 m, Fig. 10c). Large salinity misfits also persist in the mixed layer and in the halocline (120–250 m, Fig. 10d–f). The optimization has, nevertheless, significantly narrowed the misfit distribution, eliminating the largest amplitude biases throughout the water column in temperature and especially below 400 m depth in salinity. The overall reduction is 85% for temperature and 56% for salinity.

An example of how temperature misfits are reduced in the water column is shown in Fig. 11 for ITP #55, whose trajectory began in the Canada Basin interior (red circle in Fig. 11a) and ended at the slopes of the Chukchi Plateau (green square). In the observations several watermasses can be seen, including the surface cold layer above ∼30 m, warm Pacific Summer Water (PSW) at ∼40–100 m, Cold Halocline Waters at ∼110–250 m, and the Atlantic Water core at depths ∼300–750 m (Fig. 11b). In the unconstrained *it0* , both the AW boundary current and the halocline are too warm, the AW layer is too thick, and the PSW is too cold. In *ASTE_R1* , closer consistency is obtained with temperature observations for all watermasses. We emphasize that we have not applied direct adjustments to the time-varying simulated ocean state to achieve this fit (i.e., no “analysis increments” were applied). Instead, it is achieved through adjustments of the con-

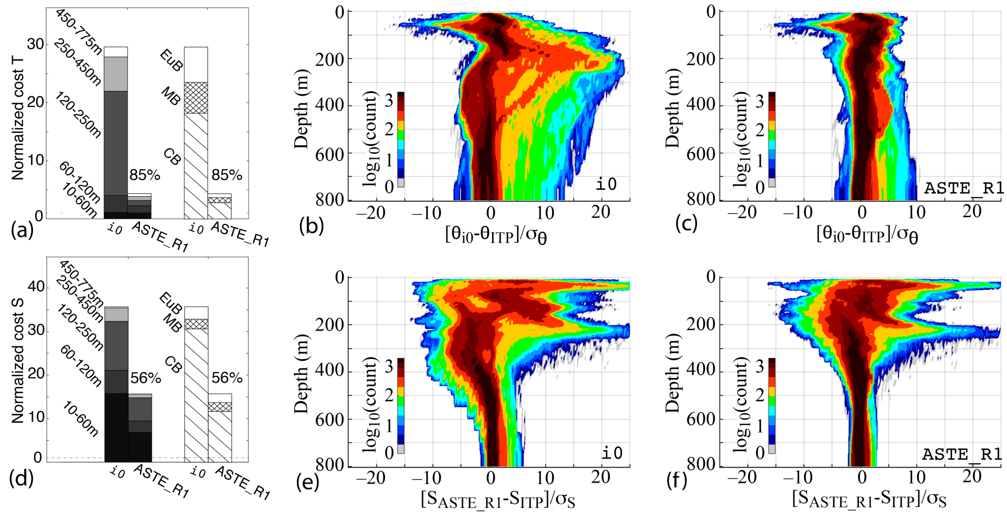

Figure 10. Normalized cost for ITP (a–c) temperature and (d–f) salinity. Costs to all ITP data are grouped by depth range and basin in (a) and (d). For the Canada Basin, histograms as a function of depths (b–c, e–f) show a narrowing of the misfit distributions for both temperature and salinity, especially in the AW layer below 250 m.

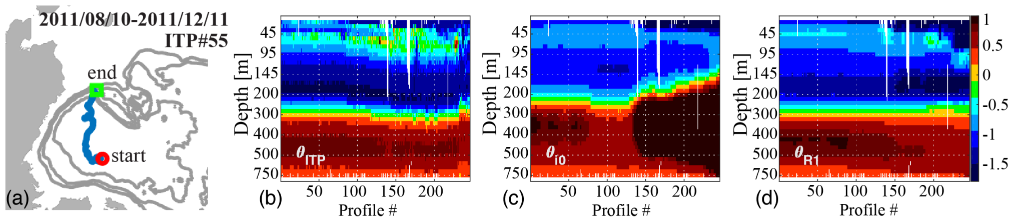

Figure 11. ITP #55 (a) trajectory, (b) potential temperature θ for all observed profiles along the trajectory, and the model equivalent for (c) *it0* and (d) *ASTE_R1* . In (a), the red circle and green square mark the first and last profile positions.

trol variables, i.e., the initial hydrography in 2002, time-averaged internal mixing parameters, and surface atmospheric forcing. As a result, a "near-perfect" fit, such as that of the WOA18 hydrography to the mean ITP data seen in Fig. 1, is not possible for this under-determined problem. The fit is, nevertheless, within the specified temperature and salinity uncertainties, with improved watermass representation for all ITP data (e.g., Fig. 11), Beaufort Gyre Moorings, NABOS moorings, and Fram Strait moorings.

3.2 The Greenland Iceland Norwegian Seas

The Greenland-Iceland-Norwegian (GIN) Seas are defined here as bounded to the south by the Greenland-Scotland Ridge (GSR) and to the north and north east by the Fram Strait and the Barents Sea Opening, respectively (see Fig. 12b). The sea ice near Fram Strait and along the East Greenland coast is seasonal and the largest misfits in *it0* were due to excessive ice here, including the Odden ice tongue (Wadhams et al., 1996) reaching further to the east during winter months (Fig. 7c–d and Fig. 12a). Surface winds and air temperature have been found to play an important role in controlling the eastern extent of the ice edge in this region (Germe et al., 2011; Moore et al., 2014). Adjustments

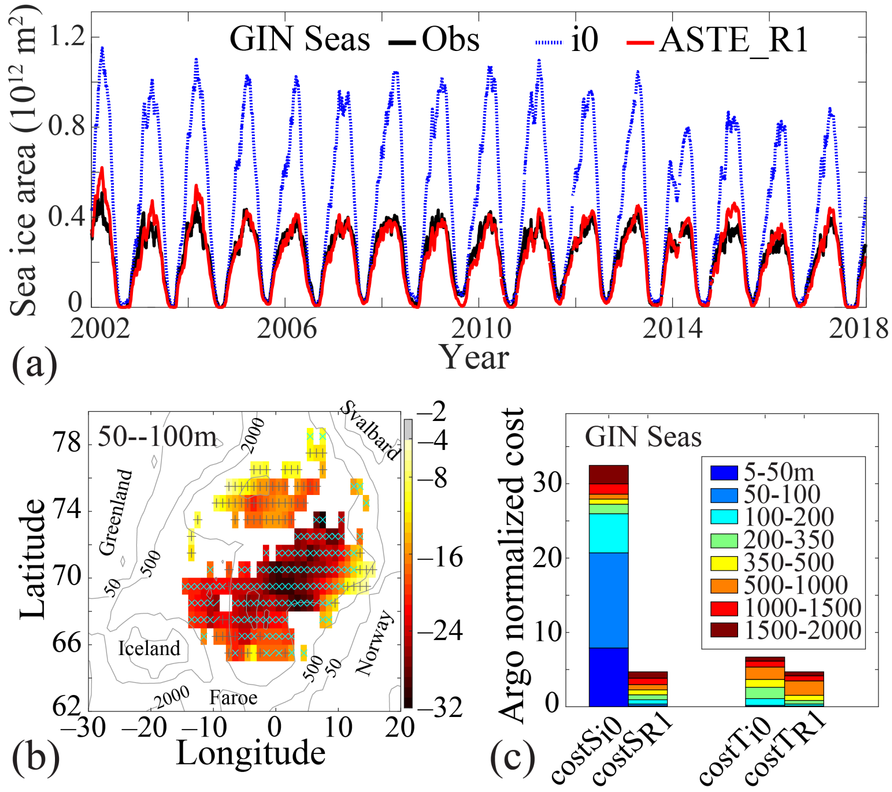

Figure 12. Improvements in GIN Seas sea ice and hydrography in *ASTE_R1* compared to *it0* . (a) Time-series of daily sea ice area for OSSISaf observations (black), *it0* (blue) and *ASTE_R1* (red). (b) Normalized misfits in salinity in the GIN Seas at depths 50–100 m, defined as $(S_m - S_o)/\sigma_S$, where "m" and "o" are model and observed Argo. For *it0* , which has a large negative bias, dimensionless misfits are indicated by the color scale ranging from -32 to -2. For *ASTE_R1* , in which the negative bias still persists but at significantly reduced amplitudes, the dimensionless misfits are indicated by symbols, with "x" and "+" corresponding to ranges $[-6,-2]$ and $[-2,0]$, respectively. The breakdown of cost reductions for all other depth ranges are shown in (c) for the GIN Seas, with overall reductions of costs of 81% and 19% in salinity and temperature relative to Argo data.

of these atmospheric state variables during the optimization, within their specified uncertainties, drove a reduction in sea ice area (Fig. 12a) to improve the model-data fit.

The Nordic Seas host the interaction of several important watermasses. Warm and salty Atlantic water enters across the GSR along three major branches, meeting locally modified water recirculating in the Lofoten, Greenland and Iceland Basins, and the southward flowing cold, fresh East Greenland Coastal Current (Hansen & Østerhus, 2000). This region is characterized by very weak stratification, resulting in a very small deformation radius of 4–7 km throughout the region (Nurser & Bacon, 2014), which further challenges realistic representation of watermass distribution in models (Drange et al., 2005; Heuzé & Årthun, 2019) and *ASTE_R1* . Nevertheless, the improvements obtained in *ASTE_R1* are substantial, with overall reductions of ∼85% and 30% for salinity and temperature costs, respectively, through the 2000 m water column (Fig. 12c). The largest improvements are associated with reduction of a fresh bias in the upper 100 m (Fig. 12b–c), across

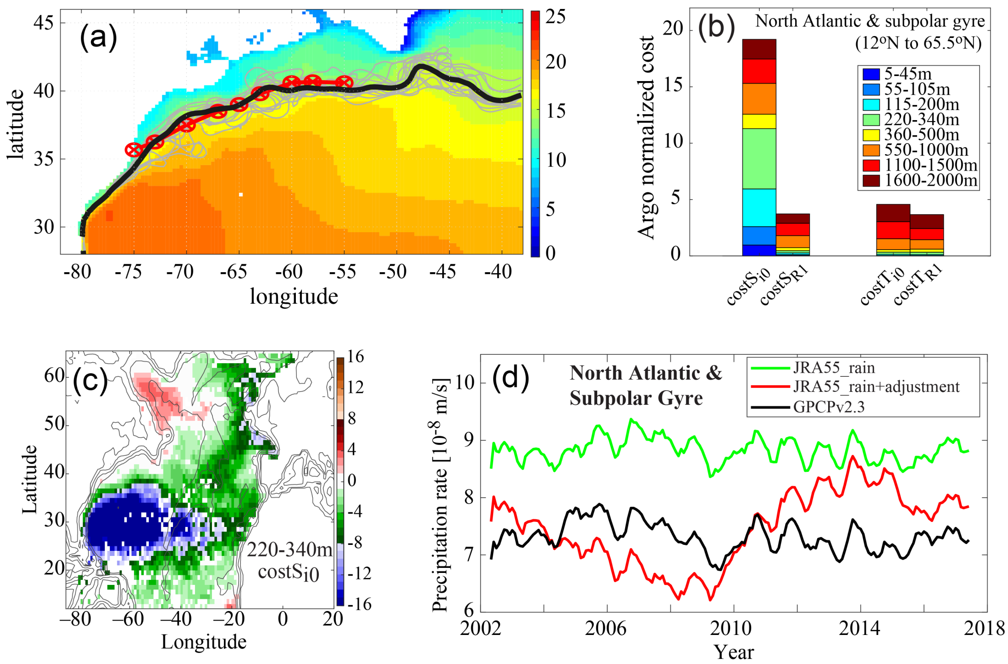

Figure 13. (a) The 2002–2017 mean proxy path of the Gulf Stream in *ASTE_R1* (black) and the World Ocean Atlas 2009 mean 15°C isotherm at 200 m depth (red, Wolfe et al. (2019)). The gray lines are the paths in *ASTE_R1* for each year. (b) Normalized cost for salinity and temperature in the North Atlantic and subpolar gyre region (latitudes 12°N–65.5°N) for *it0* and *ASTE_R1* as a function of depth range. (c) Normalized misfits in *it0* (relative to observed Argo salinity) in the water column at depth range 220–340 m. (d) Net precipitation into the North Atlantic and subpolar Gyre from JRA55 (Kobayashi et al., 2015), observational based product GPCPv2.3 (Adler et al., 2018), and adjusted rain used to force *ASTE_R1* .

the Lofoten, Iceland, and Greenland basins, which are important regions for deep water formation.

3.3 The Subpolar Gyre and North Atlantic

Although the primary focus of the study is on the assessment of *ASTE_R1* in the Arctic Mediterranean, the North Atlantic ocean serves as both the source of near surface heat and salt to the Arctic and the sink of dense deep water and surface freshwater from the Arctic Mediterranean, and so will be briefly assessed here.

One of the greatest challenges in modeling the North Atlantic is to correctly simulate the observed Gulf Stream pathway. Capturing a realistic Gulf Stream separation is non-trivial in z-level numerical models (Ezer, 2016; Chassignet & Xu, 2017). In ASTE, a combination of coastal biharmonic and off-shore Leith viscosity as described in Section 2.1 was used to achieve an observationally-consistent mean Florida Strait transport of ≈ 32 Sv (Baringer & Larsen, 2001; Johns et al., 2002) and a separation near Cape Hatteras. After separation, the Gulf Stream path can be approximately tracked using a proxy of the 15°C isotherm at 200 m depth (from the WOA13, Wolfe et al., 2019). Fig. 13a shows this proxy of the Gulf Stream path for the years 2002–2017 in *ASTE_R1* compared to that derived from WOA13.

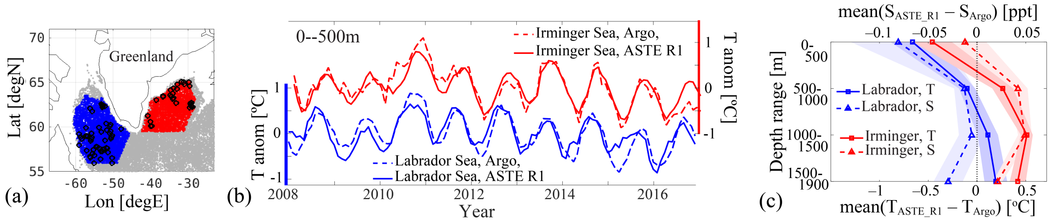

Figure 14. (a) Distribution of Argo data in the Irminger Sea (red dots) and Labrador Sea (blue dots) for the full period 2002–2017. To provide an impression of temporal coverage, black circles show data acquired within the month of January 2016. (b) Upper 500 m ocean mean temperature anomalies for the Labrador Sea (blue) and Irminger Sea (red) from Argo observations (dashed) and *ASTE_R1* . Anomalies are defined as the full time-series minus its respective mean, showing that *ASTE_R1* captures both the seasonal and interannual ocean temperature variability in both the Irminger and Labrador Seas. The biases are shown in (c) for temperature and salinity at various depth ranges sampled by Argo.

The dynamical mechanisms underlying the transports of warm AW from the Gulf Stream extension to the subpolar North Atlantic (SPNA) and into the GIN Seas across the GSR is poorly understood and its representation in state-of-the-art models remains a great challenge (Heuzé & Årthun, 2019). Compared with Argo data, the eastern SPNA hydrography (south of the GSR) contains large biases in *it0* (Fig. 13b–c) but is significantly improved in *ASTE_R1* , with a net reduction of misfit over the entire North Atlantic (north of 12°N) of ∼80% and ∼21% in salinity and temperature, respectively (Fig. 13b). Closer inspection reveals that, just south of the GSR, in the Irminger and Labrador Seas, *ASTE_R1* can reliably reproduce the observed hydrographic variability (Fig. 14a–b). However, the solution exhibits a widespread systematic warm bias between 500–2000 m underlying a cold bias in the upper ∼500 m over the subpolar region (shown for the Labrador and Irminger Seas in Fig. 14c). Overall, salinity is biased fresh in the Labrador Sea, whereas a salty bias characterizes the Irminger Sea (Fig. 14c) and the wider eastern subpolar North Atlantic region (not shown).

In the subtropical North Atlantic, a large fraction of the salinity misfit in *it0* is due to an excess freshwater flux from the atmosphere. Comparison to the independent Global Precipitation climatology Project version 2.3 product (GPCPv2.3, Adler et al., 2018) reveals an excess precipitation bias in JRA55, that is most pronounced in the North Atlantic and subpolar gyre region of the ASTE domain (Fig. 13d), and that resulted in a large fresh bias in the upper ∼500 m of the unconstrained *it0* solution (Fig. 13c). The adjoint-based optimization provided a systematic approach for removing this excess precipitation bias, such that after approximately 12 iterations the misfits to Argo salinity in the upper ocean reduced to within the observed uncertainty (Fig. 13b). Consequently, this improvement also yields better agreement in the mean with an independent GPCPv2.3 data set (Fig. 13d). It is important to stress again that these adjustments are made whilst retaining the ocean model dynamical and kinematical consistency.

4 Transports through Key Oceanic Gateways and Regional Storage

Complementing the assessment of *ASTE_R1* in terms of residual model-data misfit (previous section), we provide in the following an initial comparison of widely used oceanographic indices, including volume, heat, and freshwater transports across important Arctic and GIN Seas gateways (Table 4, Fig. 15–17) to all known observation-based estimates (Skagseth et al., 2008; Schauer & Beszczynska-Möller, 2009; de Steur et al., *Transports*

Gate	Volume [Sv]	Heat [TW]	FW [mSv]
(1)Bering Strait	1.11 ± 0.35	4.70 ± 7.25	54.24 ± 20.62
(2)CAA	−1.72 ± 0.39	7.95 ± 2.99	−94.19 ± 31.60
(3)Fram Strait	−1.50 ± 0.66	54.15 ± 13.24	−84.83 ± 23.29
(4)Svalbard–FJL[1]–SZ[2]	2.04 ± 0.64	−0.85 ± 8.03	45.23 ± 31.14
(5)Barents Sea Opening	1.98 ± 0.66	62.33 ± 15.06	−3.25 ± 3.30
(6)Davis Strait	−1.72 ± 0.39	25.40 ± 4.71	−103.32 ± 19.59
(7)Denmark Strait	−2.00 ± 0.76	11.92 ± 7.81	−42.61 ± 12.21
(8)Iceland–Faroe	2.26 ± 0.90	119.11 ± 24.09	−0.29 ± 0.69
(9)Faroe–Shetland	0.71 ± 1.30	95.00 ± 38.12	6.25 ± 4.29
(10)Newfoundland-Gr	−1.74 ± 0.38	67.30 ± 17.41	−110.67 ± 23.44
(11)48.3°N	−1.39 ± 0.36	449.66 ± 75.75	−111.60 ± 22.80

Heat Budget [TW]

Domain	Lateral conv	Vertical conv	Tendency	Bounded Gates
Arctic	65.95 ± 13.57	−39.53 ± 39.48	26.39 ± 41.34	1,2,3,4
CAA	17.46 ± 5.84	−18.08 ± 12.55	−0.63 ± 15.60	2,6
Barents	63.18 ± 19.94	−63.63 ± 37.27	−0.45 ± 47.98	4,5
GINs	109.55 ± 34.28	−110.06 ± 60.55	2.19 ± 78.36	3,5,7,8,9
Labrador Sea	41.90 ± 16.81	−49.40 ± 39.83	−7.50 ± 47.30	6,10
East SPNA	156.33 ± 96.91	−146.97 ± 92.94	6.65 ± 165.61	7,8,9,10,11

FW Budget [mSv]

Domain	Lateral conv	Vertical conv[a]	Tendency	Bounded Gates
Arctic	−79.55 ± 40.31	74.57 ± 10.28	−9.45 ± 35.83	1,2,3,4
CAA	−9.13 ± 26.29	5.78 ± 2.86	−0.51 ± 22.68	2,6
Barents	−48.48 ± 30.96	57.54 ± 7.89	−4.17 ± 30.29	4,5
GINs	51.43 ± 23.16	34.52 ± 17.74	1.20 ± 16.89	3,5,7,8,9
Labrador Sea	−7.35 ± 23.15	20.55 ± 9.58	4.56 ± 22.35	6,10
East SPNA	35.72 ± 16.92	93.94 ± 26.42	2.41 ± 20.32	7,8,9,10,11

Table 4. *ASTE_R1* budgets of volume, heat ($\theta_r = 0°$C), and FW (S_r=34.8 ppt) for the combined ocean and ice system for the period 2006–2017. All uncertainties provided are given in terms of standard deviations based on monthly estimates after the seasonal climatology has been removed. FW transport is computed using eqn. (B3.2) of Appendix B. [a]The vertical convergence of FW, from air-ice-sea fluxes, is the same as that for volume and is exact. Lateral convergence and tendency of FW, however, are approximate. As a result, the budget for FW is not fully closed (see Appendix B). [1] Franz Josef Land, [2] Severnaya Zemlya.

2009; Beszczynska-Möller et al., 2011; Curry et al., 2011, 2014; Hansen et al., 2015; Woodgate, 2018; Rossby et al., 2018; Østerhus et al., 2019). Where available, we also assess *ASTE_R1* transports against previously published estimates from coordinated modeling studies (Q. Wang et al., 2016b, 2016a; Ilicak et al., 2016; Heuzé & Årthun, 2019), ocean reanalyses (Uotila et al., 2019), and an independent inverse estimate (Tsubouchi et al., 2018).

The published literature offers notable differences in tracer reference values employed in the computation of reported heat, freshwater and volumetric watermass transports. These range from regional basin means (Smedsrud et al., 2010; Beszczynska-Möller et al., 2012; de Steur et al., 2018; Tesdal & Haine, 2020) to gateway and surface means (Tsubouchi et al., 2018) to freezing temperature in the Arctic (Beszczynska-Möller et al., 2012; Woodgate, 2018). In some cases, transports were computed along a particular range of isopycnals (Tsubouchi et al., 2018). Heat transport computed in *ASTE_R1* assumes a reference temperature $\theta_r = 0°$C (most accurate numerically, see Appendix B). For the Bering Strait, we also compute heat transport referenced to the freezing temperature of seawater $\theta_r = -1.9°$C to facilitate comparison with published estimates. For the computation of freshwater transports, we assume a reference salinity $S_r = 34.8$ ppt and integrate from the surface down to the reference isohaline. We refer the reader to Appendix B for details on potential errors incurred when computing transports using non-zero reference values. Due to the difference in reference values employed here and in some of the studies listed above, we seek consistency in terms of comparable transport magnitudes as opposed to exact agreement.

To provide a useful comparison of *ASTE_R1* mean transports with those reported in the literature, it is important to note whether published estimates are based on historic data or more recent acquisitions, given how fast the high latitudes are observed to be changing. In the first four years of the *ASTE_R1* period, 2002–2005, transports in both the North Atlantic and the Arctic exhibit distinctly different characteristics compared to the period 2006–2017. This transition of hydrographic properties and circulation patterns around 2005–2006 has been extensively discussed, with studies noting a strong increase in volume and heat transports into the Barents Sea (Skagseth et al., 2008), increased salinity and density in the lower halocline in the Eastern Arctic (Dmitrenko et al., 2011), abrupt changes in North Atlantic heat (Piecuch et al., 2017; Foukal & Lozier, 2018) and freshwater (Dukhovskoy et al., 2019) content, and rapid freshening of the Nordic Seas (Tesdal & Haine, 2020). To avoid averaging over these two apparently distinct regimes, we chose to report all mean transports for the most recent period, following the abrupt transition. Reported associated standard deviations to the 2006–2017 mean transports are computed based on the monthly values after the seasonal cycle has been removed. Details of the calculation of *ASTE_R1* transports are given in Appendix B, and watermass definitions are given in Appendix C.

4.1 Volume Transports

Østerhus et al. (2019) summarized existing estimates of volume transports across the main Arctic–Nordic Seas gateways, including the Bering Strait (BS), Davis Strait (DaS), and the Greenland-Scotland Ridge (GSR). The latter comprises the Denmark Strait (DS), Iceland-Faroe channel (IF) and Faroe-Shetland channel (FSh). Time-mean transports in *ASTE_R1* are given in Table 4 and Fig. 15, listed alongside previously published estimates from observations (Beszczynska-Möller et al., 2012; de Steur et al., 2014; Beszczynska-Möller et al., 2011; Woodgate, 2018; Curry et al., 2014; Skagseth et al., 2008; Hansen et al., 2015), and modeling studies (Tsubouchi et al., 2018; Heuzé & Årthun, 2019; Ilicak et al., 2016). In addition to net transports, we also provide estimates of transports of important watermasses at Fram Strait (as defined in Beszczynska-Möller et al., 2011) and through the GSR (as defined in Hansen & Østerhus, 2000; Østerhus et al., 2019). For the in/outflow transport estimates given in Fig. 15, we follow watermass definitions of Beszczynska-Möller et al. (2012) for Fram Strait and Østerhus et al. (2019) for the GSR.

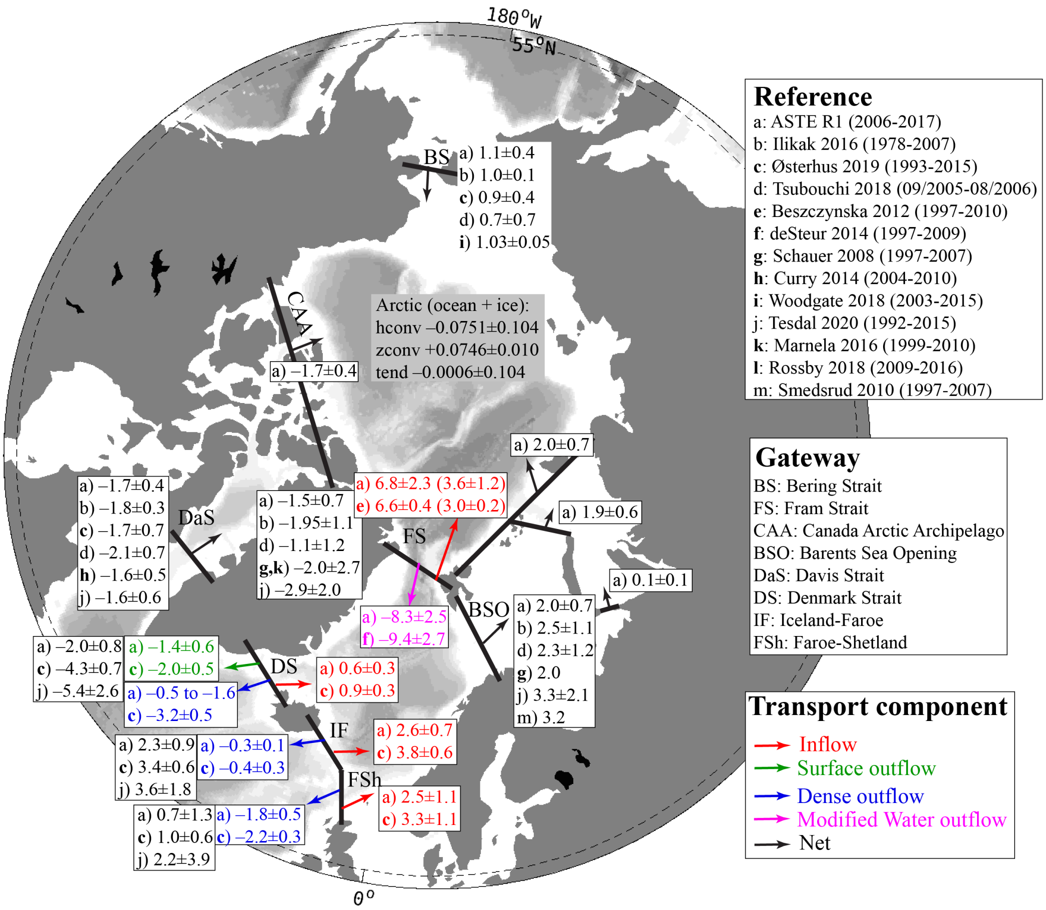

Figure 15. Volume transports across important Arctic and Nordic Seas gateways listed for (a) *ASTE_R1* and (b-m) published estimates referenced in the legend. Net transports across the full width and depth of each section are written in black; transport component contributions to this total are written in color for (red) total inflow, (green) surface outflow, (blue) dense outflow, and (magenta) modified water outflow, where arrows show the direction ascribed to in/outflow. Positive (negative) transport indicates Northward and Eastward (Southward and Westward). Quantities listed are 2006–2017 mean and standard deviation after the seasonal cycle has been removed. All net transports in *ASTE_R1* are diagnosed online, while separate transport components through FS, DS, IF, and FSh are diagnosed offline using archived monthly advection terms. See text and Appendix C for further discussion on watermass identification used in determining the in/outflow transport components. For Fram Strait infow, the two provided estimates are for the West Spitsbergen current only, and we give both the total current transport and, in parenthesis, the fraction above 2°C (Beszczynska-Möller et al., 2011). Numbers in parentheses in the Reference legend refer to the period covered by the respective studies.

All uncertainties provided are given in terms of standard deviations based on monthly estimates after the seasonal climatology has been removed.

The net volume transport of approximately 1.1 ± 0.4 Sv across the Bering Strait is northward into the Arctic. Across the Davis Strait, there is a southward transport of freshwater near the surface and northward transport of warm water from the Irminger Current (Curry et al., 2014). At this gate, *ASTE_R1* estimates a net volume transport of 1.7 ± 0.4 Sv, consistent with observed values of 1.6 ± 0.5 and 1.7 ± 0.7 from Curry et al. (2014) and Østerhus et al. (2019), respectively. Across the GSR, there is a net near-surface northward transport of AW across the Denmark Strait (DS), Iceland-Faroe (IF) and Faroe-Shetland (FSh) channels (shown in red in Fig. 15), southward surface flow of freshwater across DS and dense overflow across the entire ridge (green and blue color in Fig. 15).

Watermass definitions for surface outflow, dense outflow, modified water, and inflow AW in *ASTE_R1* can differ from Østerhus et al. (2019) and Hansen and Østerhus (2000) for the reasons outlined in Section 2.3. Our choice for σ_θ is justified in Appendix C. For the overflow through DS, the range of $27.4 \leq \sigma_\theta \leq 27.8$ used in *ASTE_R1* is associated with southward transports of -1.6 ± 0.9 to -0.5 ± 0.3 Sv (shown in blue in Fig. 15), corresponding to 16%–50% of the observed estimate using $\sigma_\theta = 27.8$ from Østerhus et al. (2019). Similar considerations for σ_θ of dense overflow water across the IF and FSh ridges (Appendix C) yield -0.3 ± 0.1 Sv and -1.8 ± 0.5 Sv, respectively, in *ASTE_R1* , compared to -0.4 ± 0.3 Sv and -2.2 ± 0.3 Sv of water with $\sigma_\theta \geq 27.8$ in Østerhus et al. (2019). For surface outflow, *ASTE_R1* underestimates the observed estimate at the DS by approximately 30%. In total, the net volume transport across DS in *ASTE_R1* is about 47% of that reported by Østerhus et al. (2019).

For the Arctic Ocean and GIN Seas heat and freshwater budgets, transports through Fram Strait (FS) and the Barents Sea Opening (BSO) are also important. Across FS, the inflow of warm AW along the West Spitsbergen Current (red color in Fig. 15) is 6 ± 1 Sv in *ASTE_R1* , with 3.4 ± 1.1 Sv carrying the core AW water warmer than $2°C$. This is consistent with corresponding estimates of 6.6 ± 0.4 and 3.0 ± 0.2 from Beszczynska-Möller et al. (2012) based on observations from an earlier period of 1997–2010. The outflow across FS includes freshwater carried by the East Greenland Current at the surface and return of modified AW at depth (magenta color in Fig. 15, Beszczynska-Möller et al., 2011). For the southward return of modified AW, *ASTE_R1* estimates a flux of of -8.3 ± 2.5 Sv over the period 2006–2017, consistent with -9.4 ± 2.7 Sv from de Steur et al. (2014) for the period 1997–2009. Across the BSO, volume transport is dominated by the eastward Norwegian Coastal Current and the Atlantic inflow which carries warm AW into the Barents Sea (Smedsrud et al., 2010). The net eastward volume transport in *ASTE_R1* of 2.0 ± 0.7 Sv is consistent with observation-based estimate of $\sim$2.0 Sv from Smedsrud et al. (2010).

4.2 Heat Transports

All *ASTE_R1* net heat transports are northward into the Arctic Basin. Time-mean transports across key gateways are consistent with observation-based estimates, a result that is aided – although by no means guaranteed – by constraining the state estimate using mooring T/S data (Table 4, Fig. 16).

At Bering Strait ASTE_R1 heat transport is 14 ± 8 TW (referenced to T_r=-1.9°C), consistent with the 11.6 TW to 14.3 TW range determined by Woodgate (2018). At Davis Strait, the *ASTE_R1* estimate of 20 ± 4 TW is consistent with 20 ± 9 TW obtained by Curry et al. (2011). Across the GSR, heat transport is in good agreement with previous published estimates across the two eastern channels (IF and FS, Fig. 16), but is underestimated across the Denmark Strait. Here, the total poleward diffusive heat flux dominates and opposes the equatorward advective term in *ASTE_R1* . This diffusive dom-

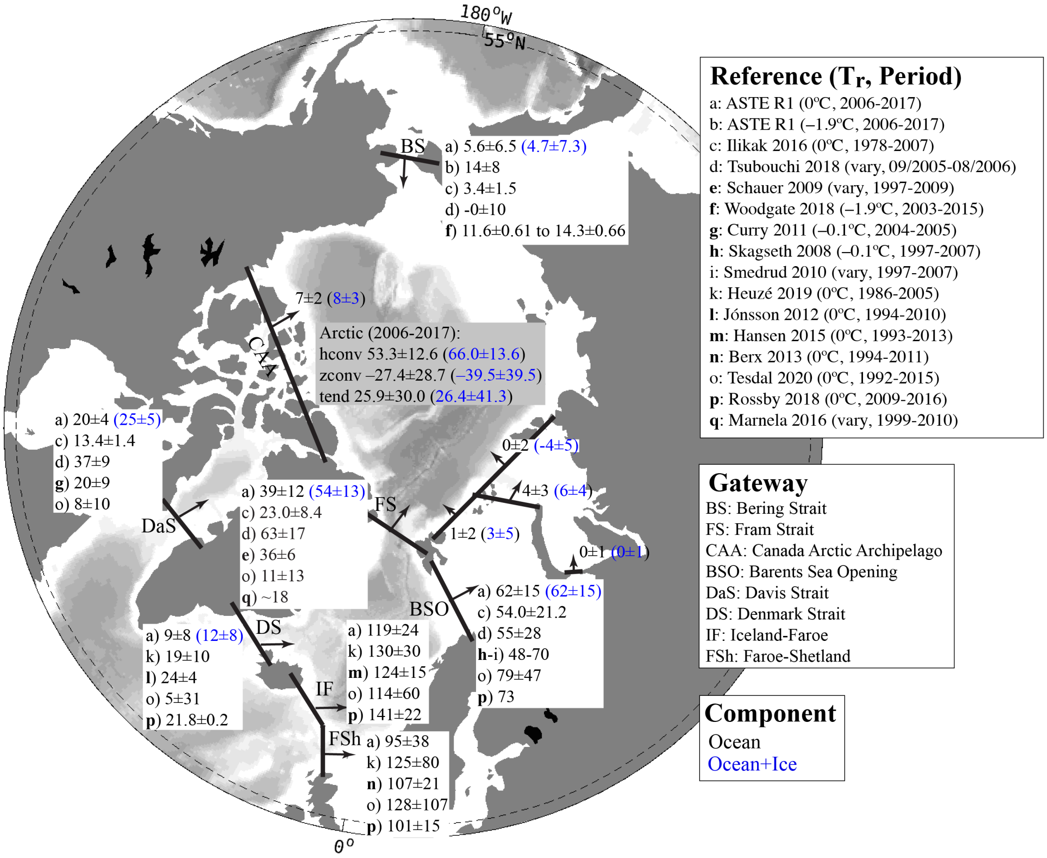

Figure 16. As for Fig. 14 but showing net ocean heat transport across important Arctic and Nordic Seas gateways. For select gateways the combined ocean+ice heat transport is also given (in blue). *ASTE_R1* transports (listed under (a)) are computed assuming a reference temperature T_r=0°C. For the Bering Strait we also provide *ASTE_R1* transports computed using T_r=−1.9°C (listed under (b)). Since previously published estimates (c-q) vary in their choice of T_r (see main text) we assess agreement between estimates as consistency in order of magnitude. Positive (negative) transport indicates Northward and Eastward (Southward and Westward) flow. Quantities listed are 2006–2017 mean and standard deviation after the seasonal cycle has been removed. Numbers in parentheses in the Reference legend refer to the T_r used and the period covered by the respective studies.

inance has also been suggested using heat budget analyses in ECCOv4 (Buckley et al., 2015). A more detailed discussion of the full time-series and contributions of advective and diffusive fluxes to the total transport is given in Appendix B.

Further north, at Fram Strait, *ASTE_R1* poleward heat transport is 39 ± 12 TW (referenced to T_r=0°C), consistent with 36 ± 6 TW from Schauer and Beszczynska-Möller (2009) and Beszczynska-Möller et al. (2011). The Fram Strait heat transport is increased by approximately one third (15 TW) on accounting for sea ice advection. Heat transport into the Barents Sea across BSO of 62 $\pm$ 15 TW is consistent with observation-based estimates of between 48 TW and 73 TW (Skagseth et al., 2008; Smedsrud et al., 2010; Rossby et al., 2018). Most of this heat is lost via air-sea exchange in the Barents and Kara Seas (Lind et al., 2018), yielding negligible heat transports from this shallow region into the Arctic Basin (Fig. 16). Air-sea exchange also accounts for significant loss

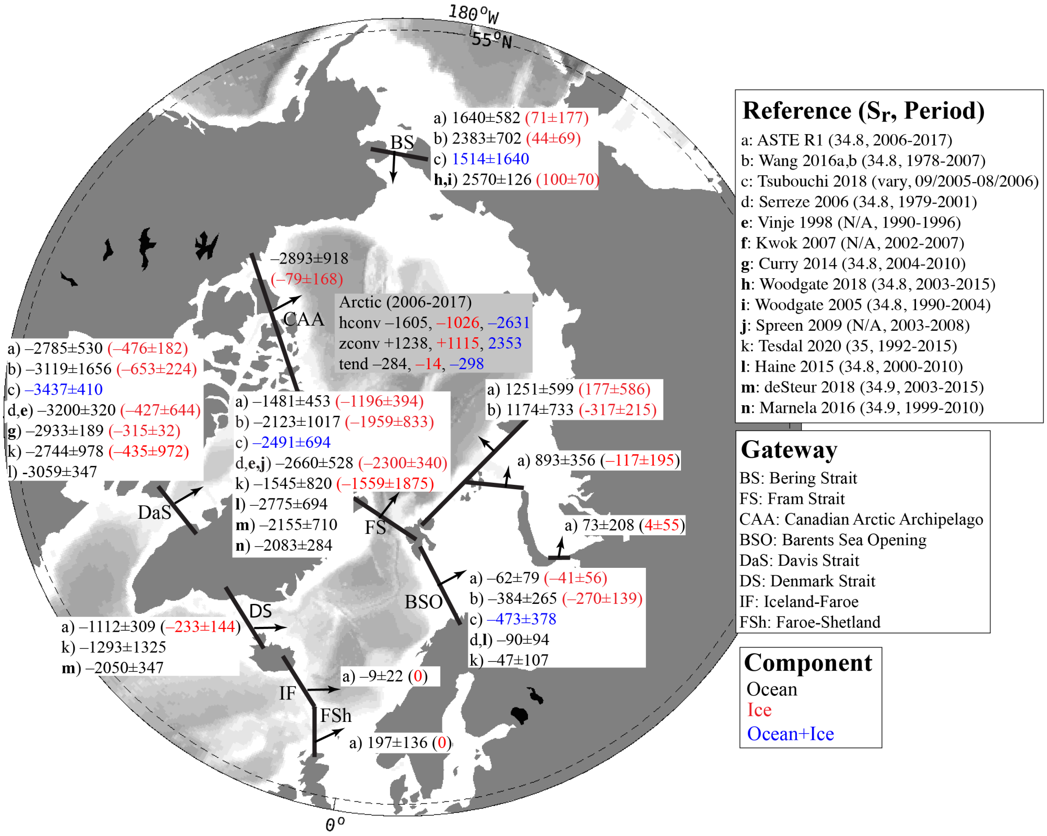

Figure 17. FW flux across important Arctic and Nordic Seas gateways from (a) *ASTE_R1* and (b-n) published estimates. Units are in km^3 yr^{-1}. S_r=34.8 ppt is used in *ASTE_R1* calculations for all FW transports and content/tendency terms for the ocean. A fixed salinity S_i=4 ppt is used for sea ice transports and tendency terms. Positive (negative) values indicate Northward and Eastward (Southward and Westward) transports. Quantities listed are 2006–2017 mean and standard deviation after the seasonal cycle has been removed. Numbers in parentheses in the Reference legend refer to the S_r used and the period covered by the respective studies.

of heat in the Canadian Arctic Archipelago, such that only ∼35% of the amount transported across the Davis Strait reaches the Arctic Basin.

There is a large spread amongst existing observation- and model-based studies with significant disagreements even after accounting for uncertainty (Fig. 16), due in part to the lack of common data period and reference temperature used in the calculations. Overall, nevertheless, the poleward heat transports in *ASTE_R1* are in good agreement with previous estimates (Fig. 16).

4.3 Freshwater Transports

The practice of reporting ocean freshwater (FW) transport/content in place of absolute salt transport/content is ubiquitous in the literature, but plagued by the need to specify a reference salinity, S_r, and to choose the vertical extent over which the integral is computed (i.e., full depth versus to the depth of the reference salinity, z_{S_r}). No unique choice emerges from consideration of seawater physics. Instead, S_r is selected inconsistently between studies. As cautioned by Schauer and Losch (2019), this not only complicates comparisons but can give very different impressions of the changing ocean state, due to strong sensitivity to the choice of S_r. Acknowledging this issue, we nevertheless elect to report FW transport below (as did Tesdal and Haine (2020) in their recent study focusing on the subpolar North Atlantic and Nordic Seas), in order to conduct our assessment of *ASTE_R1* hydrography in the context of existing estimates. To the best of our knowledge no published observational estimates report Arctic salt transports that would provide a basis for comparison (the modeling study by Treguier et al., 2014 is one known exception). We proceed with caution and flag comparisons for which calculations differ. *ASTE_R1* FW fluxes are reported using a reference salinity of S_r=34.8 ppt and integrated down to z_{S_r}. Our calculation uses monthly averages of both the Eulerian velocity and salinity. In Appendix B we provide a detailed discussion of the potential errors in FW calculations with these choices, along with errors incurred in omitting bolus and diffusive terms. Salt transport or salt content changes in *ASTE_R1* will be revisited in future work.

Similar to our assessment of volume and heat transports, we start by examining FW transports across the gates into the Arctic Mediterranean. At the Bering Strait, *ASTE_R1* combined liquid and solid FW import of 1711 ± 608 km^3/yr is lower than the 2670 ± 144 km^3/yr estimated by Woodgate et al. (2015) and Woodgate (2018). There are several candidates to explain this $\sim$960 km^3/yr FW transport deficit at this gate. Most importantly, the river runoff climatology used in *ASTE_R1* has likely not taken into account potential increased discharge from the Yukon River into the Bering Sea just upstream of the strait (Toohey et al., 2016; Holmes et al., 2012). Another likely candidate is any remaining error in the wind forcing. Nguyen et al. (2020b) showed that wind stress in both the Pacific and Arctic sectors play an important role in controlling the Bering Strait volume transports and reliably modelling the transport trends observed in Woodgate (2018), which are not present in the volume and FW transport here in *ASTE_R1* (Nguyen et al., 2020b).

At Davis Strait, *ASTE_R1* liquid and solid FW exports of -2785 ± 530 km^3/yr and -476 ± 182 km^3/yr are consistent with estimates of -2933 ± 189 km^3/yr and -315 ± 32 km^3/yr from Curry et al. (2014), on accounting for uncertainty/variability. Freshwater transports across the Iceland-Faroe and Faroe-Shetland channels are negligible. At Denmark Strait, *ASTE_R1* estimate of -1112 ± 309 km^3/yr is approximately half of the value reported by Marnela et al. (2016) of -2050 ± 347 km^3/yr. This is consistent with the 50% underestimation of both volume and heat transports in *ASTE_R1* across this gate compared to independent observations.

Further north, at Fram Strait, the liquid and solid FW exports of -1465 ± 463 km^3/yr and -1195 ± 394 km^3/yr in *ASTE_R1* are lower than the -2150 ± 710 km^3/yr liquid and -2300 ± 340 km^3/yr solid FW exports estimated by de Steur et al. (2009) and Spreen et al. (2009), respectively. A main reason for the lower (by $\sim$1800 km^3/yr) liquid plus solid export in *ASTE_R1* across Fram Strait is the lower (by $\sim$960 km^3/yr) net FW import through the Bering Strait relative to observations. An additional inconsistency is the use of a runoff climatology in *ASTE_R1* , which fails to account for Greenland solid/liquid discharge and its observed recent increase into the Arctic sector by approximately 105 km^3/yr (Bamber et al., 2012), as well as increased river outputs (as reported in Bamber et al., 2012; Proshutinsky et al., 2020). With respect to the latter, *ASTE_R1* has a deficit of $\sim$ 220 km^3/yr. The climatology also does not account for Greenland FW (combined solid and liquid) discharge into the GIN Seas and Baffin Bay of nearly 150 km^3/yr and 250 km^3/yr, respectively (Bamber et al., 2012). In the Canadian Arctic Archipelago, *ASTE_R1* has a FW flux deficit of $\sim$226 km^3/yr from land ice (Carmack et al., 2016). These omissions likely contribute to the underestimation of southward FW transports across both the Denmark Strait (by $\sim$940 km^3/yr) and Davis Strait (by $\sim$150 km^3/yr).

The net lateral convergence of the combined liquid and solid freshwater flux in *ASTE_R1* of -2510 ± 1272 km^3/yr is nearly balanced by the net vertical convergence of $2353 \pm$

324 km^3/yr, yielding a net tendency of -298 ± 1131 km^3/yr. For the liquid flux alone, the tendencies are -1484 ± 1123 for lateral convergence, 1238 ± 2478 vertical convergence, and -284 ± 2169 km^3/yr total tendency.

4.4 Heat and Freshwater Storage

Complementing the transport estimates, we conclude our initial assessment of *ASTE_R1* with an overview of derived basin-scale 2002-2017 time-mean and time-variable heat and freshwater budgets, focusing on comparisons between *ASTE_R1* and existing estimates. A full assessment of the mechanisms underlying Arctic Mediterranean and subpolar North Atlantic heat and freshwater content change over the *ASTE_R1* period will be addressed in a separate study. As noted earlier, decisions made in our tracer transport/budget calculations facilitate these comparisons but are non-unique. For freshwater transports/budgets this introduces ambiguity that is best resolved prior to detailed dynamical investigation.

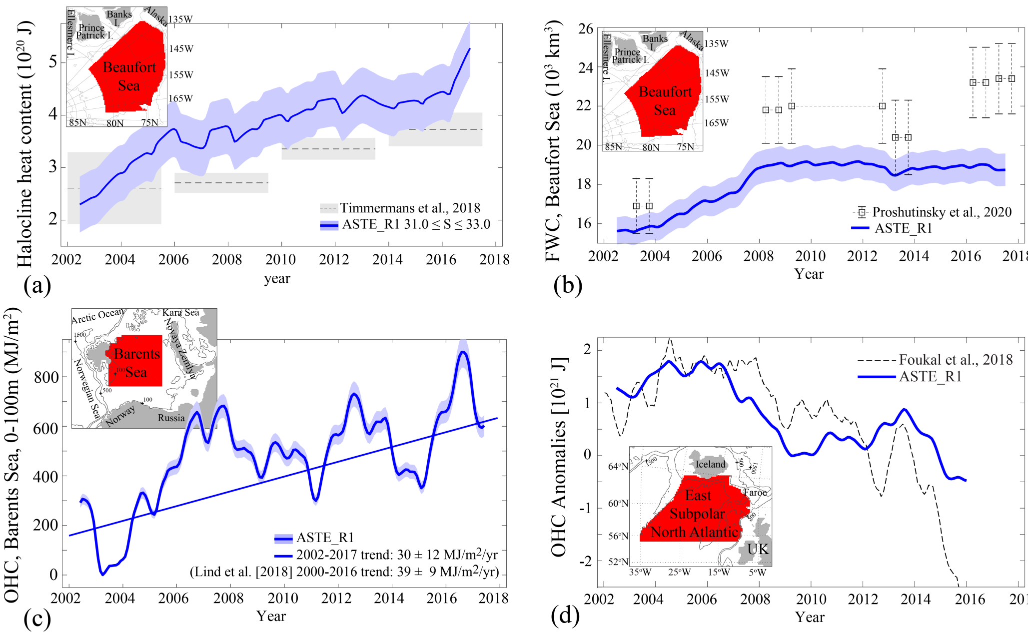

Figure 18. Comparison of *ASTE_R1* (a) Beaufort Sea halocline (defined as $31.0 \leq S \leq 33.0$) heat content, (b) Beaufort Sea freshwater content above the 34.8 ppt isohaline, (c) Barents Sea 0–100 m heat content and, (d) East Subpolar North Atlantic full-depth heat content with existing observational-based estimates, as given in the legend of each panel. Insets show the spatial mask defining each region. A 12-month running mean has been applied to filter the seasonal cycle from the *ASTE_R1* time-series, facilitating comparison with observed trends. Shading in *ASTE_R1* time-series indicate the sensitivity of the (a,c) heat content to a 5% change in (a) the northern and (c) eastern spatial mask, or the sensitivity of the (b) freshwater content to a 0.5 ppt change in the lower limit employed in the halocline watermass definition (see Appendix C).

4.4.1 Heat Content

Considering the Arctic region of *ASTE_R1* in its entirety, the net heat input from convergence of horizontal (ocean plus ice) heat transports (53.3 ± 12.0 TW) exceeds the net heat loss due to local air-ice-sea fluxes (-27.4 ± 28.7 TW) by a factor $\sim$2, yielding a net heating rate of 25.9 ± 30.0 TW when averaged over the period 2006–2017 (Table 4). Relative to horizontal convergence, vertical exchange at the air-ice-sea interface is significantly less well constrained due to large uncertainties in atmospheric reanalyses at high northern latitudes (Beesley et al., 2000; Chaudhuri et al., 2014; C. Wang et al., 2019). Partitioned by basins, similar enthalpy gains are estimated for both the western (14.0 ± 24.3 TW) and eastern (12.5 ± 14.0 TW) Arctic region. In the water column, heat gain is concentrated mainly in the AW layer (240–1000 m) in both the western (9.3 ± 2.7 TW) and eastern (6.4 ± 4.6 TW) Arctic. In the upper 60 m of the water column, the tendency is negligible but with large variability (0.2 ± 25.3 TW) due to mixed layer processes and exchange with the atmosphere.

Warming since the early 2000s has been reported in the Arctic, documented alongside enhanced "Atlantification" in the Eastern Arctic (Polyakov et al., 2017, 2020) and a fivefold increase in solar obsorption by near surface waters in the Western Arctic (Jackson et al., 2010; Timmermans et al., 2018). This warming proceeds at a sustained rate, with recent studies suggesting a doubling of OHC in the Beaufort Gyre halocline between 2003 and 2013 (Timmermans et al., 2018).

Fig. 18a shows a comparison of the time-series of the halocline heat content in *ASTE_R1* and estimates based on ITP and mooring data in the Beaufort Sea. As discussed in Section 2.3, adopting exact watermass classifications from observational studies may be inappropriate for model analysis, due to representation error of subgrid scales. Thus in addition to the salinity limits used to identify the upper halocline layer of $31.0 \leq S \leq 33.0$ in Timmermans et al. (2018), we also compute the heat content sensitivity to the salinity bounds. By changing the near-surface lower salinity bound within the range 31–31.5 ppt, the mean halocline heat content changes by 2–3% per 0.1 ppt increment, but the variability and trend remain unchanged. This confirms that despite the systematic warm bias, the positive trend in halocline heat content is well-captured in the *ASTE_R1* solution.

In the Canada Basin, *ASTE_R1* exhibits a warming rate of 9.3 ± 2.7 TW for the period 2006–2017 (Fig. 16). There are insufficient observations to validate this directly, but we can corroborate our estimate with a back of the envelope calculation as follows. Recent ITP acquisitions report core AW temperatures in this region $\sim$0.5°C warmer than the PHC climatology (Fig. 19a), where the latter is representative of the second half of the 20th century. Since ITPs only measure to $\sim$800 m depth, we conservatively assume a depth-average warming of 0.20–0.25°C over the 170–1000 m range in the Western Arctic basin interior (area 4400×10^3 km^2), yielding a warming rate of $\sim$5.7–7.2 TW, about two thirds of the rate estimated in *ASTE_R1* . Compared to ITP data, *ASTE_R1* shows a positive bias of $\sim$0.15°C in the core AW temperature in the Western Arctic basin, which accounts for the higher tendency here. However, we note that this *ASTE_R1* bias is within the combined data and representative error σ_T, which is not the case for the PHC bias (Fig. 19b).

The Eastern Arctic suffers from an extreme paucity of data, such that even back of the envelope estimates of basin-wide heat content (and its tendency) are not possible. Instead, we turn to recent observations for evidence of warming in this basin. Pulsed injection of AW at Fram Strait has been documented by Polyakov et al. (2011). A notable warm anomaly pulse of $\sim$1°C entered the Arctic in 2004. It has subsequently been observed crossing the NABOS section at 126°E, and has been recorded further downstream at numerous sections along the eastern basin's rim (Polyakov et al., 2011). In addition, the seasonal amplitude within the halocline has been observed to increase by 0.75°C between 2004 and 2015 (Dmitrenko et al., 2009; Polyakov et al., 2017; Baumann et al., 2018). These observations provide evidence for a warming Eastern Arctic and a weakened halocline. The latter is accompanied by shoaling of the AW layer toward the bottom of the mixed layer and increasing heat ventilation (Polyakov et al., 2020). This is a mechanism by which heat along the AW pathway is removed instead of being sequestered at depth. To determine the relative importance of these two mechanisms (ventilation ver-

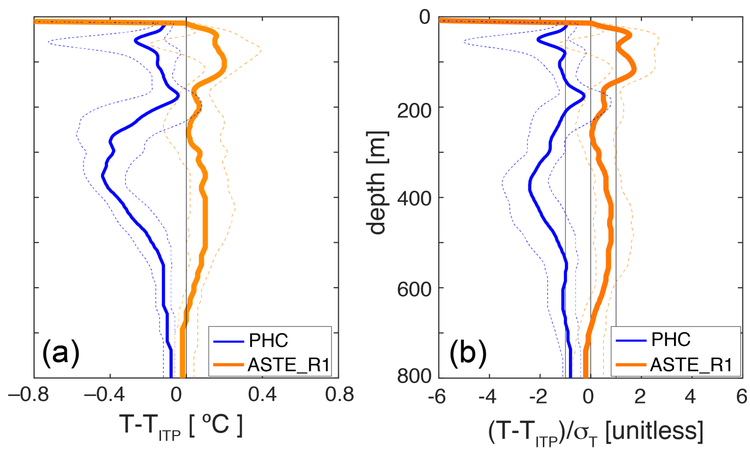

Figure 19. Comparison between all ITP-derived temperature profiles in the Canada Basin and PHC (blue) and *ASTE_R1* (orange). Panel (a) shows the normalized 50th percentile difference (dimensionless) and (b) the 50-percentile difference (°C). The two vertical black lines in (b) at ± 1 indicate the limits within which the difference is within the uncertainty σ_T. The dotted lines show the 30th and 70th percentile differences.

sus sequestration) in contributing to the positive heat content tendency at different depths and throughout the Arctic in *ASTE_R1* , a more detailed analysis of AW circulation and ventilation will be needed in future work.

In the Barents Sea, Lind et al. (2018) documented pronounced increases in decadal mean OHC in the upper 100 m of the water column, which they attributed to an increase in AW inflow through the Barents Sea Opening. In Fig. 18c we compare OHC trend (upper 100 m) from Lind et al. (2018) with *ASTE_R1* illustrating that *ASTE_R1* captures the 2002–2016 positive trend. Further south, Piecuch et al. (2017) and Foukal and Lozier (2018) have quantified OHC trends in the SPNA (between 46°N and 65°N) using SST, ECCOv4r3 and OHC derived from the Hadley Centre EN4 gridded product. The comparison between Foukal and Lozier (2018) and *ASTE_R1* (Fig. 18d) shows good quantitative agreement, with an increase in OHC between 2002–2005, a decrease in OHC between 2005–2009, and a hiatus between 2009–2014, followed finally by a further decrease in OHC after 2014.

4.4.2 Freshwater Content

Based on observations, predominantly from satellite altimetry and ITPs in the Beaufort Sea, the liquid freshwater content (FWC) in the Arctic has been estimated to be increasing (Proshutinsky et al., 2019). Proshutinsky et al. (2020) summarized recent works attributing this FWC increase to several factors, including shifts in atmospheric circulation, increased FW fluxes through the Bering Strait, and increased runoff from the MacKenzie river. A comparison between *ASTE_R1* and Proshutinsky et al. (2019) estimates for FWC in the Beaufort Gyre shows that *ASTE_R1* captures the observed increase in FWC between the 2004 to 2008. With the exception of a small decrease in 2015 – also seen in the observations – the Beaufort Gyre FWC in *ASTE_R1* remains relatively constant for the period 2008–2017 (Fig. 18b). Proshutinsky et al. (2019) report an increase from 2015–2017 which is likely missing from *ASTE_R1* due to the omission of both increased river runoff and land ice discharge in our forcing climatology and absence of the observed increase in FW import through the Bering Strait as previously discussed (Fig 17).

The connection between the Arctic FWC increase and circulation changes in the GIN Seas and North Atlantic has been the subject of several investigations (Dukhovskoy et al., 2016; Carmack et al., 2016; Tesdal & Haine, 2020). A recent review by Haine et al. (2015) summarized Arctic exchanges with the Canadian Arctic Archipelago (north of Davis Strait) and the Barents Sea (east of the Barents Sea Opening). These estimates heavily rely upon atmospheric reanalyses (for the provision of surface fluxes) and unconstrained model output (for tracer content change). Further south, Dukhovskoy et al. (2019) investigated the redistribution of increased Greenland freshwater discharge (solid and liquid) in the Subpolar North Atlantic (SPNA) and the GIN Seas, highlighting large uncertainty due both to lack of constraint and acute dependency of transports on model resolution (see also Weijer et al., 2012).

5 Discussion

A preliminary discussion of how the optimization acts to bring the model into consistency with the available observations focuses on the question of which control variables played a dominant role in achieving a reduction in misfit (Section 5.1). A second point of discussion highlights known issues with this first release of ASTE and suggestions on how to improve future releases (Section 5.2).

5.1 Identifying Key Control Adjustments

Experiment 1		**Experiment 2**	
Ensemble Member	optimized control(s) *added*	Ensemble Member	optimized control(s) *withheld*
1	$[\theta_0^{R1}, S_0^{R1}]$	1	$[\theta_0^{i0}, S_0^{i0}]$
2	$[\mathcal{K}_\sigma^{R1}, \mathcal{K}_{gm}^{R1}]$	2	$[\mathcal{K}_\sigma^{i0}, \mathcal{K}_{gm}^{i0}]$
3	$\mathcal{K}_z^{R1}$	3	$\mathcal{K}_z^{i0}$
4	$[u_w^{R1}, v_w^{R1}]$	4	$[u_w^{i0}, v_w^{i0}]$
5	T_{air}^{R1}	5	T_{air}^{i0}
6	q_{air}^{R1}	6	q_{air}^{i0}
7	$[R_{sw}^{R1}, R_{lw}^{R1}]$	7	$[R_{sw}^{i0}, R_{lw}^{i0}]$
8	P^{R1}	8	P^{i0}

Table 5. Ensemble members for each of the two ensemble experiments. In experiment 1, the control variables listed in column #2 were *added* to unoptimized *it0* ; in experiment 2, the control variables listed in column #4 were *withheld* from optimized *ASTE_R1* .

Production of the *ASTE_R1* solution was achieved by gradient-based optimization, which iteratively adjusts a set of control variables (Section 2.2). Our control space ($\mathbf{\Omega}$) comprises 3D fields of initial (i.e., 01/01/2002) temperature and salinity (θ_0, S_0), time-mean spatially varying ocean mixing coefficients ($\mathcal{K}_\sigma, \mathcal{K}_{gm}$, and $\mathcal{K}_z$), and time-varying 2D fields of near-surface atmospheric state variables ($T_{air}, q_{air}, u_w, v_w, R_{sw}, R_{lw}$, and P). We now seek to identify which of these control variable adjustments had the largest impact on reducing the model-data misfit in *ASTE_R1* relative to the unoptimized *it0* .

To proceed, we performed two forward ensemble experiments, each experiment consisting of eight members. In the first experiment, individual optimized control variables from *ASTE_R1* were substituted into *it0* , which was then re-run. Each ensemble member is characterized by containing one of the *ASTE_R1* optimized control variables or variable pairs listed in Table 5 (left two columns). Note that there are 8 variables that come in pairs, thus making 4 total pairs: the optimized initial conditions (θ_0^{R1}, S_0^{R1}), the optimized diffusivities for the eddy mixing parameterization ($\mathcal{K}_\sigma^{R1}, \mathcal{K}_{gm}^{R1}$), the two components of the wind speed (u_w^{R1}, v_w^{R1}), and the net downward radiation (R_{sw}^{R1}, R_{lw}^{R1}). For any given ensemble member, large reductions in misfit indicate that the substituted optimized control plays an important role in the *ASTE_R1* solution.

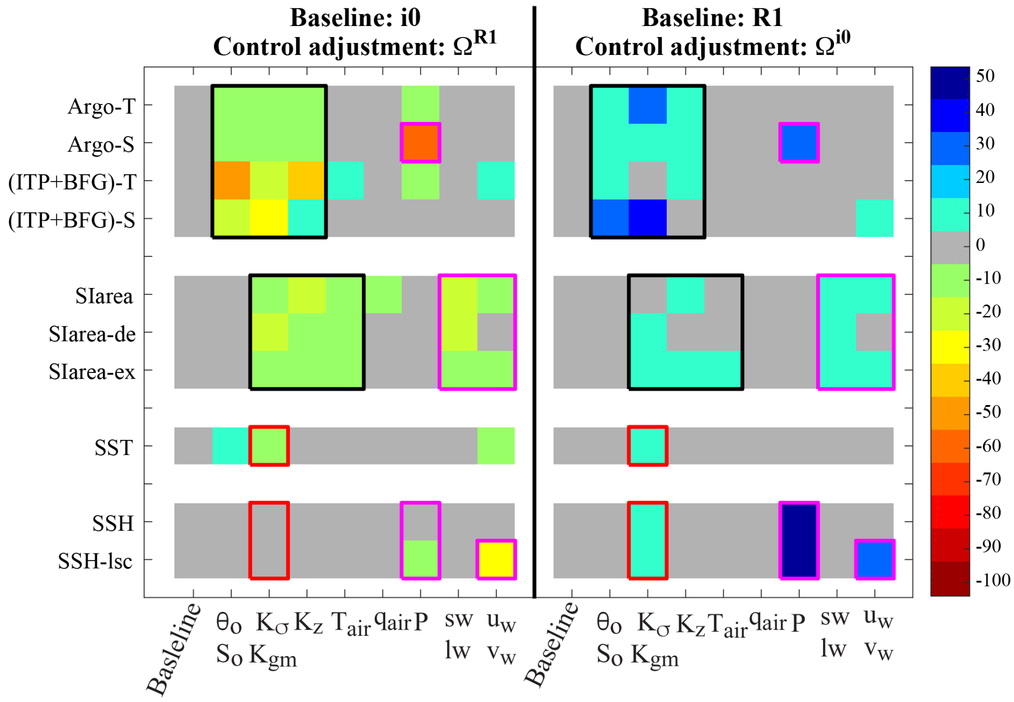

Figure 20. Percentage change (color) in cost with respect to the constraint listed on the ordinate, attributable to the control substitutions given on the abscissa. The left group are ensemble members of perturbation experiment 1, for which optimized controls $\mathbf{\Omega}^{R1}$ are substituted into the *it0* re-runs. The right group are ensemble members of experiment 2, for which non-optimized controls $\mathbf{\Omega}^{i0}$ are substituted into the *ASTE_R1* re-runs. On the left half of the plot, negative values indicate an improved solution i.e., a cost reduction with respect to *it0* , implying that the optimized controls are important for reducing the misfit. On the right half, positive values indicate deterioration of the solution i.e., a cost increase with respect to *ASTE_R1* , implying that these control adjustments are critical for obtaining the optimized *ASTE_R1* state. Colored rectangular outlines highlight patterns of most impactful control variables (e.g., precipitation is important for the reduction of costs to Argo salinity and SSH).

However, a note of caution is needed. The control variables are not fully independent (e.g., some of the atmospheric state variable controls are related via bulk formulae or shared physics), and as a result, it is not possible to determine their full impact in isolation. For this reason, we performed a second set of experiments, reversing the sense of the substitutions, such that the non-optimized controls from *it0* were substituted into *ASTE_R1* , which was then re-run (i.e., the optimized control variables were reset to their first guesses). In this experiment, each ensemble member is characterized by containing one of the *it0* non-optimized control variables or variable pairs listed in Table 5 (right two columns). This second experiment lends confidence to our assessment as follows: an optimized control is highly likely to be an important ingredient of the *ASTE_R1* solution if its incorporation notably improves the *it0* re-run (first ensemble) while its omission notably degrades the *ASTE_R1* re-run (second ensemble).

In Fig. 20 we examine the impact of the control substitutions on the costs in both ensemble experiments. We show only normalized costs with respect to the following aggregated data sets: Argo, ITP, Beaufort Gyre moorings, and satellite-based observations of SST, SSH and sea ice concentration. This choice enables a more focused discussion whilst also informing the large-scale quality of the solution near the ocean surface in the Atlantic Ocean (where the majority of SSH and SST data were acquired) and throughout the upper ocean in the North Atlantic, GIN Seas, and Labrador Sea interior (from Argo T and S data) and in the western Arctic (from ITP and Beaufort Gyre moorings). Lastly, costs for sea ice concentration indicate performance of modelled air-sea fluxes and mixed layer properties in marginal ice zones (see Fig. 7 and related discussion).

Our analysis, based on Fig. 20, reveals the importance of precipitation (P) adjustments in obtaining realistic subsurface salinity distributions in the North Atlantic through the removal of the systematic excess rain bias discussed in Section 3.3 (Fig. 13d). Specifically, inclusion of the optimized precipitation P^{R1} in the *it0* re-run (column under "P" on the left half of Fig. 20) reduced the cost with respect to Argo salinity by 56% (orange square at row "Argo-S" and column "P" corresponding to large negative, i.e., cost reduction, values between -50 and -60 as indicated in the color scale). A 31% increase in this cost was seen on omission of the optimized precipitation in the *ASTE_R1* re-run (blue square at row "Argo-S" and column "P" on the right half of Fig. 20, corresponding to positive, i.e., cost increase, values between $+30$ to $+40$ in color scale). Large improvements in SSH can also be attributed in part to corrected precipitation, as well as surface winds. Amongst other atmospheric forcing variables, surface air temperature, downward radiative forcing, and winds all have important impact on the sea ice cover (collective average of 17% improvement to *it0* and 5% degradation to *ASTE_R1*).

Adjustments to the initial conditions, vertical diffusivity and eddy mixing are also found to be important for improving subsurface hydrography throughout the *ASTE_R1* domain. Optimized eddy mixing-related controls ($\mathcal{K}_{\sigma}^{R1}, \mathcal{K}_{gm}^{R1}$) alone result in a 14% improvement (and 14% degradation) of the Arctic hydrography misfit when included (omitted) from the *it*0 (ASTE_R1) re-runs, respectively. These adjustments to the eddy mixing parameters also improve SST and SSH, and – in addition to the adjustments made to the vertical diffusivity and atmospheric conditions – are also seen to be critical for improved representation of sea ice cover.

5.2 Known Issues and Future Directions

During production of *ASTE_R1* we have striven to utilize all constraints known to us and that the state estimation machinery could handle. This comprises O(10^9) observations from diverse data sources (Table 2). Despite this effort, some systematic biases remain in the *ASTE_R1* solution. As the optimization is ongoing and ASTE is still converging, we anticipate the costs listed in Table 3 will continue to reduce and some of the remaining biases will be removed. In certain cases, due to model structural errors or nonresolved physics, full convergence might not be attainable (Wunsch & Heimbach, 2007). Here we discuss notable issues remaining in the *ASTE_R1* solution and possible future directions for developing the next ASTE release with improved model physics.

Eastern Arctic hydrography: One of the largest remaining systematic biases is found in the Eurasian Basin, where subsurface constraints comprise sparse ITP sampling of the basin interior alone. Although the inflow is constrained by moorings at Fram Strait, downstream observation of the circulation, eddy-induced stirring and vertical mixing in the Eurasian Basin along the shelf-basin slope and interior are limited (Fig. 21a). The serious implications of this paucity of data are highlighted by considering that the AW inflow takes ∼6-10 years to transit this region, during which there are no local observa-

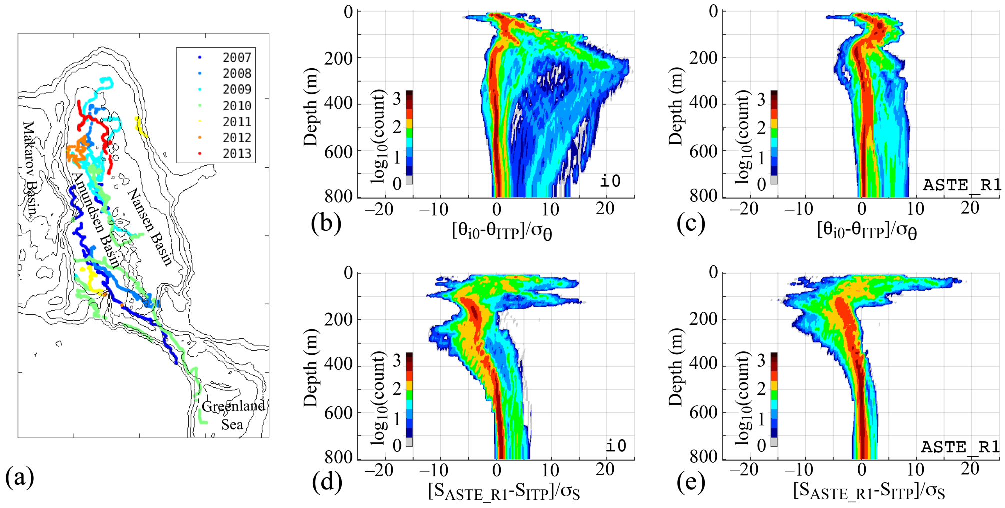

Figure 21. (a) Spatial distribution of ITP data used to constrain *ASTE_R1* in the Eurasian Basin; colors distinguish acquisition year. Histograms of normalized misfit to ITP (b,c) temperature and (d,e) salinity as a function of depth in the Eurasian Basin for (b,d) *it0* and (c,e) *ASTE_R1* .

tional constraints. As a result, the inverse problem is highly under-determined. In practice, under-determination allows non-unique pathways to misfit minimization. For *ASTE_R1* , we find that the AW layer in the Eastern Arctic spreads to occupy a greater depth range towards the end of the estimation period. This problem was also present in *it0* and has been partly ameliorated during the optimization, as reflected in the removal of the largest positive temperature misfits with respect to ITP data (Fig. 21b-c). This thickening of the AW layer is also a common problem in many state-of-the-art Arctic Ocean models (Holloway et al., 2007; Ilicak et al., 2016; Docquier et al., 2019; Uotila et al., 2019).

As it is unlikely that widespread observation of 3-D velocity and mixing will be made in the foreseeable future, we anticipate that AW watermass representation in the Eurasian basin will remain an issue for both the next generation of state-of-the-art Arctic Ocean models and the next ASTE release. Although we do not expect large gains from planned changes to the ocean observing system in the near future, we do anticipate improvements in sea ice state, mixed layer representation, and shelf-basin exchanges in the next ASTE release, due to recent improvements to the stability of the adjoint of the sea ice thermodynamics (Bigdeli et al., 2020). This will enable a more complete use of sea ice observations as active contributions to the cost function reduction J (eqn. 1). The sensitivity of the associated model-data misfits to the control space can then be used to better adjust atmospheric forcings. This will allow us to fully leverage the constraint from satellite-based observations of the sea-ice state, which could only be partly exploited in the pseudo sea ice adjoint employed for construction of *ASTE_R1* . Inclusion of the sea ice thermodynamics adjoint could potentially improve AW upward ventilation (Ivanov et al., 2012; Polyakov et al., 2020) and preserve a more stable AW layer thickness, both in the Eurasian Basin and further downstream in the Western Arctic.

Arctic Circumpolar Current: In the Laptev Sea it is thought that the circumpolar circulation of AW splits at ∼145°E, with a fraction returning to Fram Strait along the Lomonosov Ridge (Rudels, 2015) and the remainder continuing along the basin's rim into the Western Arctic, although the exact partitioning is not well constrained. In the Western Arctic it is typically assumed that the AW continues to circulate cyclonically along the basin boundary, although both *ASTE_R1* (Grabon, 2020) and a modeling effort informed by observed radionuclide distributions (Karcher et al., 2012) suggest a weak anticyclonic circulation during the last decade. Recent work analyzing all available current meters (updated from Baumann et al. (2018)) has yielded velocity probability distributions for the Arctic region. This will be investigated as a novel approach to constrain ocean velocities within the AW circulation in the next ASTE release. In addition, a more detailed examination of the momentum and vorticity budgets along the circumpolar current will offer insights into the role of viscous dissipation and eddies in maintaining the cyclonic sense of circulation (Yang, 2005; Spall, 2020).

Arctic river runoff and Greenland discharge: FW transports and content in the late 2010s are low in *ASTE_R1* relative to independent observations (Section 4.3 and 4.4.2). Near the surface in the Arctic and along the Greenland coast, recent increases in river (Shiklomanov et al., 2020) and tundra runoff (Bamber et al., 2012), surface solid and subsurface glacial discharge (Bamber et al., 2012, 2018) have been observed. This increase was not included in the *ASTE_R1* forcing. Meaningful application of these FW fluxes as model forcings, especially in the Arctic marginal seas, requires careful consideration of the following factors. Sub-glacial discharge is observed to enter the outlet glacier fjord at depths near the grounding line instead of at the surface of the fjord's exit to the continental shelf (Straneo & Cenedese, 2015; Sciascia et al., 2013). Mixing and entrainment of this FW with the surroundings creates modified water whose property is prohibitively difficult to continuously track downstream from the source using observed T/S (Beaird et al., 2018). Consequently, the pathways of FW redistribution are highly uncertain. Numerical simulations with Greenland discharge distributed at the surface yield pathways from the source into the interior of SPNA and GIN seas that vary substantially with model resolution and representation of mean currents (Weijer et al., 2012; Dukhovskoy et al., 2016). The depth to which this FW is mixed down also varies highly with resolution (Dukhovskoy et al., 2016), causing near surface over-freshening in certain cases and a 30–50% decrease in the North Atlantic Meridional Overturning Circulation (AMOC) at time-scales varying between 3–50 years (Weijer et al., 2012). Similarly, preliminary sensitivity experiments in *ASTE_R1* with observed Greenland discharge applied at the surface show over-freshening of the upper ocean in the Greenland Sea and a decrease in the AMOC at 55°N by 40% within 5 years, inconsistent with observations (not shown). Prior to the next ASTE release, a dedicated study will be required to implement updated estimates of Greenland discharge as a subsurface freshwater forcing, consistent with observations (Straneo & Cenedese, 2015). This will entail incorporation of a melt water plume parameterization into the ASTE framework. Lastly, instead of being absorbed into net surface freshwater flux $E-P-R$, a new control variable for runoff could be introduced to isolate and fully interrogate sensitivity to subsurface forcing from subglacial discharge.

Subpolar North Atlantic hydrography: A warm bias in *ASTE_R1* at 500–2000 m depth persists both in the Irminger Sea (Fig. 14c) and throughout the eastern SPNA (not shown), and is associated with a weaker poleward transport of Atlantic warm water across the GSR (Fig. 15). Poor representation of AW inflow across the GSR is a common problem in coarse to medium resolution ocean models (Heuzé & Årthun, 2019). Specifically, these models produce lower volume and heat transports across the GSR compared to observations (Heuzé & Årthun, 2019). Since the resolution of *ASTE_R1* is $\sim$18 km in the subpolar gyre, we anticipate incomplete representation of both eddy/diffusive mechanisms – estimated to be important across the shallow Denmark Strait and Iceland-Faroe Ridge (Buckley et al., 2015) – and watermass transformations in the *ASTE_R1* solution. Thus, although *ASTE_R1* can capture the mean transports of volume and heat between Iceland and Scotland (Fig. 15–17), the remaining warm bias across Denmark Strait and south of the GSR likely impacts our estimate of heat content in both the eastern SPNA and Nordic Seas and alters the optimized air-sea heat flux in both regions. Recent data from the Overturning in the Subpolar North Atlantic Program (OSNAP) observing system (Lozier et al., 2017, 2019) mooring array (deployed in 2014) will provide important information in the subpolar region, and an especially valuable constraint on the boundary currents and overflow waters, not captured by Argo.

6 Summary and Outlook

We have presented the first release of the Arctic Subpolar gyre sTate Estimate, *ASTE_R1* , a data-constrained and dynamically consistent ocean-sea ice synthesis spanning the period 2002–2017. *ASTE_R1* is produced using the ECCO adjoint-based state estimation framework, in which an ocean general circulation model, the MITgcm serves as a dynamical interpolator, spreading the influence of O(10^9) incorporated observations through space and time by way of linearized adjustment processes encapsulated in an adjoint model. Importantly, the model-data misfit is reduced via iterative adjustments to the initial hydrographic conditions, atmospheric forcing and model mixing parameters alone, ensuring adherence to the governing equations throughout the entire estimation period. This distinguishes our approach from ocean reanalysis, in which violation of conservation laws complicates application for climate research (Stammer et al., 2016). The ability to assess closed tracer and momentum budgets in *ASTE_R1* is a key strength of the product. As all sources and sinks are accounted for, full heat, salt and momentum (or vorticity) budgets can be analyzed to identify dominant sources contributing to the observed changes. These closed budget analyses can also be performed in T, S, σ space following R. P. Abernathey et al. (2016), enabling diagnosis of watermass evolution and destruction in the *ASTE_R1* solution. In addition, the adjoint modeling infrastructure allows for linear sensitivity studies using *ASTE_R1* for investigation of causal mechanisms underlying variability in key quantities of climate interest (e.g., Bigdeli et al., 2020; Nguyen et al., 2020b; Pillar et al., 2016).

During production of *ASTE_R1* we have strived to utilize all observational constraints known to us and that the state estimation machinery can handle. *ASTE_R1* thus arguably represents the biggest effort undertaken to date with the aim of producing a specialized Arctic ocean-ice estimate, freely available to the research community. This complements existing global ECCO solutions (Forget et al., 2015a; Fukumori et al., 2018a), the Southern Ocean State Estimation (SOSE, (Mazloff et al., 2010)) and other global and regional ECCO derivatives (e.g., Köhl & Stammer, 2008; Gopalakrishnan et al., 2013; Zaba et al., 2018; Köhl, 2020).

For this initial assessment of *ASTE_R1* , we have focused on comparison to available observational constraints. Many of these were actively employed in the optimization procedure, but some (e.g., all volume and tracer transport estimates) were withheld, allowing independent verification. The optimized solution serves as a significant improvement from the unconstrained state, achieving consistency with the majority of incorporated observations, including both the set used in the optimization and that retained for post-validation (Table 3).

The most substantial misfit reduction in *ASTE_R1* are sea ice cover in the marginal ice zone, western Arctic hydrography, and subtropical North Atlantic sea level anomaly and subsurface salinity (Table 3, Fig. 6). In the Arctic Mediterranean, using only a proxy sea ice adjoint, *ASTE_R1* achieves a 83% reduction in misfit to satellite-derived sea ice concentration constraints, mainly via improved representation of the sea-ice edge (Fig. 7). The solution faithfully reproduces both the observed seasonal cycle and low frequency trend of sea-ice extent.

At Fram Strait, the mooring array is crucial to constraining the important AW inflow and local hydrographic properties. At this important Arctic gateway, *ASTE_R1* exhibits a 58% misfit reduction through the water column across the strait relative to the unconstrained simulation. In the Arctic interior, ITPs provide unique information on the subsurface hydrography. Because 71% of the ITP profiles are located within the upper

5–800 m in the Canada Basin interior, the most significant misfit reduction was seen here (85% in T and 62% in S, Fig. 10). In the remaining Arctic basin, low data coverage, combined with large uncertainty in the mean circulation and mixing parameters, resulted in less notable improvement (reductions of 89% in T and 31% in S), but biases persist, especially at depth below the AW core (Fig. 21).

Accompanying improved fit to hydrographic data used to constrain the solution, we find improvements in basin-scale heat and freshwater content. Interannual variability and low frequency trends in both heat and FW content are well represented in the Arctic Mediterranean and SPNA of *ASTE_R1* . In the Beaufort Sea, *ASTE_R1* captures the observed steady increase in upper halocline heat content from 2004–2017. Both the observed heat content increase in the upper water column within the Barents Sea and the heat content decrease in the east SPNA are also consistently captured (Fig. 18).

We have been careful to clearly outline the notable biases remaining in the *ASTE_R1* solution. These include a warm bias below the AW core in the eastern Arctic and in the east SPNA. The cause is a combination of lack of constraint here for the hydrography, mean circulation, and the adjustable initial condition and parametric controls. Additional biases exists in FW transports and contents in the Arctic Mediterranean due to the omission of increased runoff from Arctic rivers and Greenland freshwater discharge.

An advantage of our approach is that the use of a dynamical interpolator can improve spectral representation of the estimated state compared to gridded products produced using statistical interpolations (e.g., Verdy et al., 2017). This has not been addressed here, but it is a useful avenue for future ASTE assessments and ongoing development.

Looking toward the next *ASTE_R1* release, we expect the greatest progress will be made by incorporating new model physics. In particular, improving the stability of the sea ice thermodynamic adjoint (Bigdeli et al., 2020) will enable its use in ASTE, providing stronger constraint of air-ice-sea exchanges and ocean ventilation. Future efforts will target hydrographic improvements along the Arctic shelf-basin slope in the eastern Arctic to reduce the *ASTE_R1* AW layer warm bias. Additionally, updated estimates of runoff and calving fluxes and inclusion of a parameterization of sub-glacial discharge will enable improved estimate of freshwater redistribution and interbasin exchange. New constraints, including datasets from the OSNAP mooring array (Lozier et al., 2017, 2019), sea surface salinity (Vinogradova & Ponte, 2012; Fournier et al., 2019), and sea ice thickness (Tian-Kunze et al., 2014; Ricker et al., 2017) will also be fully utilized in the production of a further improved next ASTE release.

Appendix A *ASTE_R1* Product Distribution

A1 Configuration set up

The model configuration and all necessary inputs, including the optimized control adjustments, required for *ASTE_R1* re-runs are available to the public, as discussed in the next section. The code base employed for *ASTE_R1* production was MITgcm checkpoint c65q. *ASTE_R1* was built using the full state estimation infrastructure, including specialized packages for misfit and adjustment evaluation, developed for ECCOv4r1 (Forget et al., 2015a). In addition, two code developments specific to ASTE include the implementation of a vertical diffusivity power control ($\log_{10}\mathcal{K}_z$) and the capability to switch between daily and monthly SSH costs.

To ensure numerical stability during *ASTE_R1* production, the following model choices were important: (a) a staggered time-step for momentum advection and Coriolis terms; (b) third-order advection for tracers (scheme code 30 in Table 2.2 in Adcroft et al., 2018), (c) linear free surface approximation, and (d) application of freshwater forcing via a virtual salt flux (i.e., no accompanying change in mass). These choices permitted a time-step of 1200 s. After 62 iterations, better model choices were used for the final forward run that produces more accurate physics in the distributed version of *ASTE_R1* . These include (i) seventh order advection for tracers (scheme code 7 in Table 2.2 in Adcroft et al., 2018); (ii) nonlinear free surface with scaled z^* coordinates (Adcroft & Campin, 2004), and (iii) application of freshwater forcing via a real freshwater flux (i.e., with accompanying change in mass, Campin et al., 2004). These choices required a shorter time-step of 600 s. The *ASTE_R1* solution described and assessed in this paper is from the re-run of iteration 62 with the model choices (i)–(iii) described above.

In the distributed code, at compile and run-time, the user has the choice to use the more stable set up with a time-step of 1200 s or employ the more accurate numerics and physics with a time-step of 600 s as described above. We found that these small changes in the model configuration for the final forward run did not have a significant impact on the solution. This result is consistent with published studies suggesting small differences in ocean dynamics between LFS vs NLFS in combination with virtual salt or real freshwater flux (Roullet & Madec, 2000; Campin et al., 2004; Yin et al., 2010). The advantage of their application here is in enabling more accurate physical interpretation of mass and freshwater budgets. However, since these options also require a shorter timestep (for the nonlinear free surface) and a larger stencil (for the higher order advection), their use demands significantly more computational resources (twice the wallclock time). For this reason, it was not feasible to employ these options until the final stages of *ASTE_R1* development.

A2 Distribution of the *ASTE_R1* solution

The full *ASTE_R1* solution is publicly available through the NSF Arctic Data Center as follows:

a. Time varying fields as monthly averages and monthly snapshots (Nguyen et al., 2021a);
b. Depth-integrated time varying fields as monthly averages and monthly snapshots (Nguyen et al., 2021b);
c. Selected time varying state variables as daily averages (Nguyen et al., 2021c);
d. 12-month climatological averages (Nguyen et al., 2021d);
e. In situ profiles and model-equivalent (Nguyen et al., 2021e);
f. *ASTE_R1* Grid files, Documentations (user guide, domain layout) and MATLAB toolbox to help analyze the output fields (Nguyen et al., 2021f);
g. Compile time and run time inputs necessary to reproduce *ASTE_R1* with the MITgcm (Nguyen et al., 2021g).

All model output fields are available here as NetCDF files. In addition to being archived at the Arctic Data Center, *ASTE_R1* NetCDF data are also mirrored at the UT-Austin ECCO portal at: `https://web.corral.tacc.utexas.edu/OceanProjects/ASTE/`, which is provided by the Texas Advanced Computing Center (TACC). Alternative to NetCDF format, the monthly mean fields are additionally hosted in a compressed format on Amazon Web Services (AWS) servers, provided by TACC at `http://aste-release1.s3-website.us-east-2.amazonaws.com/`. These files are meant to be accessed with the `llcreader` module of the open source python package `xmitgcm` (R. Abernathey et al., 2020), which allows users to analyze the data without the need to actually download it. An interactive demonstration of this capability, which shows some sample calculations enabled by `xgcm` (R. P. Abernathey et al., 2020) and ECCOv4-py (`github.com/ECCO-GROUP/ECCOv4-py`), is available through the Binder Project (Project Jupyter et al., 2018) at `github.com/crios-ut/aste` (T. Smith, 2021). This repository additionally contains environment files so that any user can reproduce the computing environment necessary to analyze *ASTE_R1* , for instance on their own laptop.

A3 Observational constraints from ECCOv4r3 standard suite

As described in Section 2.1, the observational constraints used in ASTE include the standard ECCOv4r3 suite (Fukumori et al., 2018b) and additional high-latitude data as listed in Table 2. For a quick reference, we list the data from the ECCOV4r3 suite in Table A1 and refer the readers to Fukumori et al. (2018b) for further details on the data description and preparation.

Variable	Observations
Sea level	TOPEX/Poseidon (1993-2005), Jason-1 (2002-2008), Jason-2 (2008-2015), Geosat-Follow-On (2001-2007), CryoSat-2 (2011-2015), ERS-1/2 (1992-2001), ENVISAT (2002-2012), SARAL/AltiKa (2013-2015)
Temperature profiles	Argo floats (1995-2015), XBTs (1992-2008), CTDs (1992-2011), Southern Elephant seals as Oceanographic Samplers (SEaOS; 2004-2010), Ice-Tethered Profilers (ITP, 2004-2011)
Salinity profiles	Argo floats (1997-2015), CTDs (1992-2011), SEaOS (2004-2010)
Sea surface temperature	AVHRR (1992-2013)
Ocean bottom pressure	GRACE (2002-2014), including global mean ocean mass
TS climatology	World Ocean Atlas 2009
Mean dynamic topography	DTU13 (1992-2012)

Table A1. The standard ECCOv4r3 data suite used to constrain *ASTE_R1* . The entries in this table are duplicates from Table 1 in Fukumori et al. (2018b).

Appendix B Transport Calculation with Referenced θ/S

Here we describe heat and freshwater transport calculations used in *ASTE_R1* with respect to reference values of potential temperature (θ_r) and salinity (S_r), respectively. This serves to (1) provide calculation details for comparison to those used by previously published estimates (supplementing results presented in section 4), and (2) expose where calculation differences may prevent meaningful comparisons (following discussion in section 2.3). For budget calculations, we refer the readers to detailed descriptions provided in Piecuch (2017) and Forget et al. (2015a).

In the literature, transports are often computed with nonzero referenced values θ_r/S_r. In section 4 we provided online transport estimates for *ASTE_R1* made using non-zero references (e.g., for the heat flux through the Bering Strait). We emphasize that all offline transport calculations made using available diagnostics from *ASTE_R1* (and all standard configurations of the MITgcm) will be exact only with $\theta_r = 0$ and $\mathrm{S}_r = 0$, as these are the values used in all online tracer equations. To support users seeking to compute *ASTE_R1* transports offline assuming nonzero references, we now examine the loss of accuracy that will be incurred. This loss of accuracy depends on the amplitude of various missing terms (e.g., bolus transports and diffusive fluxes) relative to the contributions (e.g., Eulerian advection) contained in the available diagnostics. By deriving these approximations here and comparing their magnitudes with the accurate online values across important Arctic and GIN Seas gateways, we aim to identify which transports reported in Fig. 16-17 are reliable and which ones require caution for interpretation.

B1 Accurate transport calculations

The horizontal transports of volume, heat, and freshwater (FW) across the Arctic Mediteranean gateways are calculated by summing the total horizontal convergence in the mass, heat, and salinity budgets, respectively, (Piecuch, 2017) as follows,

$$
\begin{aligned}
F_V &= \int_L \int_{-D}^{\eta} \mathbf{u}_E \cdot \hat{\mathbf{n}}\ dz\ dl && \text{(B1.0)}\\
F_H &= \rho_0 C_p \int_L \int_{-D}^{\eta} (\theta - \theta_r)(\mathbf{u}_E + \mathbf{u}_b) \cdot \hat{\mathbf{n}}\ dz\ dl + \rho_0 C_p F_{\theta,dif} + F_{H_i,adv} + F_{H_{sn},adv} \\
&= F_{H_\theta,adv} + F_{H_\theta,dif} + F_{H_i,adv} + F_{H_{sn},adv} && \text{(B2.0)}\\
F_{FW} &\approx \int_L \int_{-z_{S_r}}^{\eta} \frac{(S_r - S)}{S_r}(\mathbf{u}_E + \mathbf{u}_b) \cdot \hat{\mathbf{n}}\ dz\ dl + \left(1 + \frac{\eta}{D}\right)\frac{F_{S,dif}}{S_r} + \int_L \left(\frac{S_r - S_i}{S_r}\frac{\rho_i}{\rho_0} h_i \mathbf{u}_i + \frac{\rho_{sn}}{\rho_0} h_{sn} \mathbf{u}_{sn}\right) \cdot \hat{\mathbf{n}}\ dl \\
&= F_{FW_S,adv} + F_{FW_S,dif} + F_{FW_i,adv} + F_{FW_{sn},adv} && \text{(B3.0)}
\end{aligned}
$$

where t is the time, $\mathbf{u}_E, \mathbf{u}_b$ the (partial-cell-weighted) ocean resolved Eulerian and unresolved bolus velocities, and $\mathbf{u}_i, \mathbf{u}_{sn}$ the sea ice and snow Eulerian velocities. For each gateway across which the transports are computed, $\hat{\mathbf{n}}$ is the normal direction at each model grid point along the transport gate and L the section length along the gate. Vertical integration is between η the sea surface and $-D$ the ocean floor depth for volume and heat transports. Constants $\rho_0 = 1029, \rho_i = 910$ and $\rho_{sn} = 330$ are the seawater, sea ice, and snow densities in kg/m^3. $C_p = 3996$ J°C^{-1}kg^{-1} is the specific heat capacity of sea water, θ_r the reference temperature, $S_r = 34.8$ ppt the reference salinity, and $S_i = 4$ ppt the constant sea ice salinity used in ASTE. θ and S are the ocean potential temperature and salinity in °C and ppt, respectively; h_i and h_{sn} are the thickness of sea ice and snow in m. $F_{\theta,dif}$ and $F_{S,dif}$ are the parameterized diffusive flux of potential temperature and salinity $\theta_r = 0$ and $S_r = 0$. For both advective and diffusive contributions to freshwater transports (eqn. B3.0), vertical integration is only down to the depth of the reference isohaline $-z_{S_r}$.

Exact closure of heat budgets (see equations in Forget et al. (2015a) and Piecuch (2017)) and exact (to within numerical precision) calculation of heat transports (eqn. B2.0) can be achieved when $\theta_r = 0$ and all diagnostics terms are computed online. Near exact freshwater budgets (see equations in Forget et al. (2015a) and Tesdal and Haine (2020)) and transports (eqn. B3.0) can be achieved with $S_r = 0$. Additionally the vertical integral must be computed every time step, continuously updating the time-evolving z_{S_r}.

B2 Approximations for nonzero θ_r/S_r

When using nonzero reference values (e.g., $\theta_r = -0.1$°C or $S_r = 34.8$ ppt as in Østerhus et al., 2019), neither heat nor freshwater diffusion terms are available in the offline diagnostics. To gauge orders of magnitudes, however, we approximate the diffusion term for FW using $F_{S,dif}$ scaled by the non-linear free-surface factor $(1+\frac{\eta}{D})$ following Piecuch (2017), then further scale by $\frac{1}{S_r}$. For the advection terms, the long-term mean transport can be derived exactly for heat and approximated for FW using a combination of readily available offline diagnostics for volume and heat/salt budgets as follows:

$$\begin{aligned}\left\langle F_{H_\theta,adv}\right\rangle &= \rho_0 C_p \Big\langle \int_{-D}^{\eta}\int_L \Big((\theta-\theta_r)(\mathbf{u}_E+\mathbf{u}_b)\Big)\cdot\hat{\mathbf{n}}\;dz\;dl\Big\rangle \\ &= \rho_0 C_p \Big\langle \int_{-D}^{\eta}\int_L \theta(\mathbf{u}_E+\mathbf{u}_b)\cdot\hat{\mathbf{n}}\;dz\;dl\Big\rangle - \rho_0 C_p\theta_r \Big\langle \int_{-D}^{\eta}\int_L \mathbf{u}_E\cdot\hat{\mathbf{n}}\;dz\;dl\Big\rangle \end{aligned} \tag{B2.1}$$

$$\begin{aligned}\left\langle F_{FW_S,adv}\right\rangle &\approx \Big\langle \int_{-z_{S_r}}^{\eta}\int_L \frac{(S_r-S)}{S_r}(\mathbf{u}_E+\mathbf{u}_b)\cdot\hat{\mathbf{n}}\;dz\;dl\Big\rangle \\ &\approx \Big\langle \int_{-z_{S_r}}^{\eta}\int_L \Big(\frac{S_r}{S_r}(\mathbf{u}_E+\mathbf{u}_b) - \frac{S}{S_r}(\mathbf{u}_E+\mathbf{u}_b)\Big)\cdot\hat{\mathbf{n}}\;dz\;dl\Big\rangle \\ &\approx \Big\langle \int_{-z_{S_r}}^{\eta}\int_L \mathbf{u}_E\cdot\hat{\mathbf{n}}\;dz\;dl\Big\rangle - \frac{1}{S_r}\Big\langle \int_{-z_{S_r}}^{\eta}\int_L S(\mathbf{u}_E+\mathbf{u}_b)\cdot\hat{\mathbf{n}}\;dz\;dl\Big\rangle \end{aligned} \tag{B3.1}$$

where the $\langle\cdot\rangle$ is the multi-year mean which ensures $\langle \mathbf{u}_b\rangle \equiv 0$ by definition. The approximation in $F_{FW_S,adv}$ is due, again, to the reliance in the offline average of $\langle S\rangle$ in determining $-z_{S_r}$.

B3 Approximations using monthly mean θ, S and $\mathbf{u}_E$,

Lastly, we note that due to disk space and I/O restrictions, it is typical for modelling studies to save and subsequently provide only monthly-averaged Eulerian velocity $\langle \mathbf{u}_E\rangle$ and tracers $\langle\theta\rangle$ and $\langle S\rangle$ for offline calculations of heat/FW transports and contents (e.g., Jahn et al., 2012; Kinney et al., 2014; Q. Wang et al., 2016b, 2016a; Ilicak et al., 2016; Heuzé & Årthun, 2019). In this case, the calculation for the advective terms in heat and FW transports are further approximated due to the cross-terms involving the bolus velocity $S\mathbf{u}_b$ and $\theta\mathbf{u}_b$ being excluded:

$$F_{H_\theta,adv} \approx \rho_0 C_p \int_{-D}^{\eta}\int_L (\theta-\theta_r)\;\mathbf{u}_E\cdot\hat{\mathbf{n}}\;dz\;dl \tag{B2.2}$$

$$F_{FW_S,adv} \approx \int_{-z_{S_r}}^{\eta}\int_L \frac{(S_r-S)}{S_r}\mathbf{u}_E\cdot\hat{\mathbf{n}}\;dz\;dl \tag{B3.2}$$

As before, inaccuracies will be incurred when z_{S_r} is determined using the monthly mean $\langle S\rangle$. This is the case for all results shown for FW because no diagnostics pertinent to FW, including those of $S - S_r$ or z_{S_r}, are available standard MITgcm diagnostic outputs.

B4 Interpretation of Transports: Confidence and Caution

Fig. B1-B2 show time-series of heat and FW transports for key gateways using both the most accurate online method and approximated offline method described above. The diffusion terms for both heat and FW are at least two orders of magnitude smaller than the advection terms and can be ignored almost everywhere. The exception is at the Denmark Strait and Iceland-Faroe channels where omission of the diffusive contribution to the total heat transport leads to large errors of 30% and 100%, respectively. This shows that the estimates of tracer transports across these two gates should be interpreted with caution when computed offline using only model monthly outputs of the Eulerian velocity and tracer averages.

For FW, as all methods are approximated, the largest error is likely due to not tracking the time-evolving depth of the reference isohaline z_{S_r}. Since there is no exact calculation for comparison, it is not possible to conclude which method, "adv" using the online advective term (eqn. B3.0) or "off" using the monthly mean Eulerian velocity and tracers (eqn. B3.2, is "more" correct in Fig. B2 and Table B1. It is likely that for gates where these two methods provide almost identical estimates (e.g., Bering, Davis and Fram Straits) we have higher confidence in our estimated FW transport. Across the CAA and the GSR the FW transport calculation depends strongly on the method employed and caution should be used in confidently reporting FW fluxes and comparing between different studies.

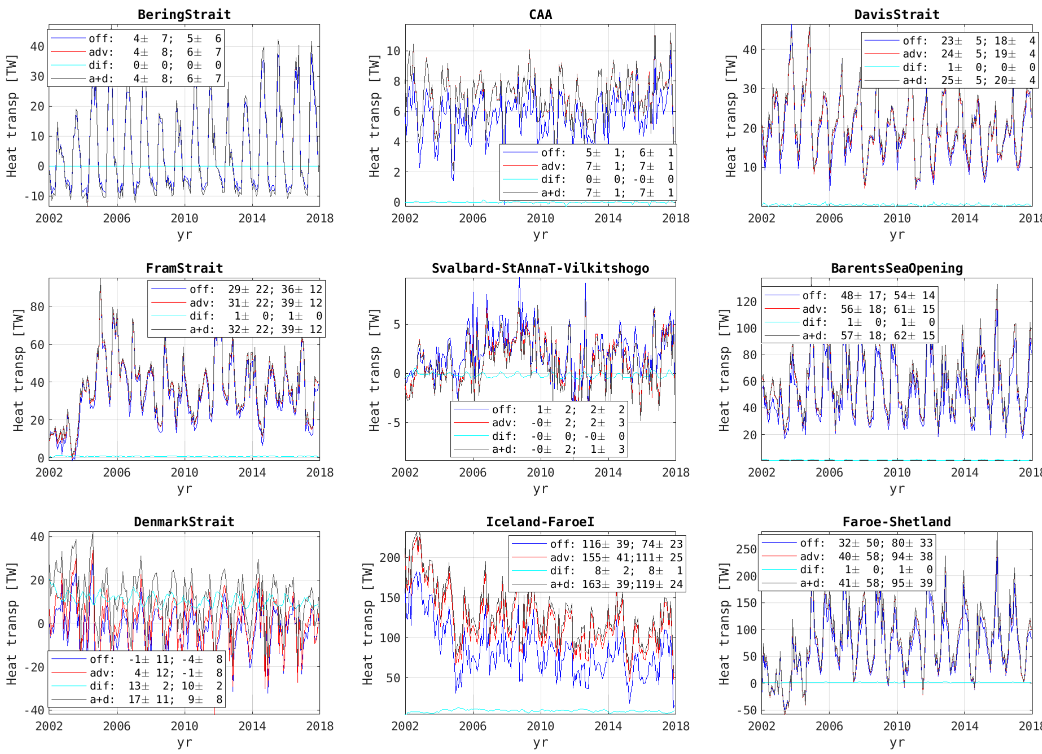

Figure B1. Time series of ocean heat transports (assuming a reference potential temperature θ_r=0) across important Arctic Mediterranean gateways using online (eqn. B2.0) and offline methods ("off", eqn. B2.2), with the latter using outputs of monthly-averaged Eulerian velocity $\langle \mathbf{u}_E \rangle$ and potential temperature $\langle \theta \rangle$. "adv" and "dif" are online calculations of the advective ($F_{H_\theta,adv}$) and diffusive ($F_{H_\theta,dif}$) terms for ocean transports on the RHS of eqn. (B2.0), and their sum is given by "a+d". The quantities listed in the legend are the 2002–2006 and 2007–2017 means and month-to-month variability. The variability is computed after the seasonal cycle has been removed. As explained in the main text, statistics are reported separately for these two periods due to large observed changes in the Arctic around 2006/2007.

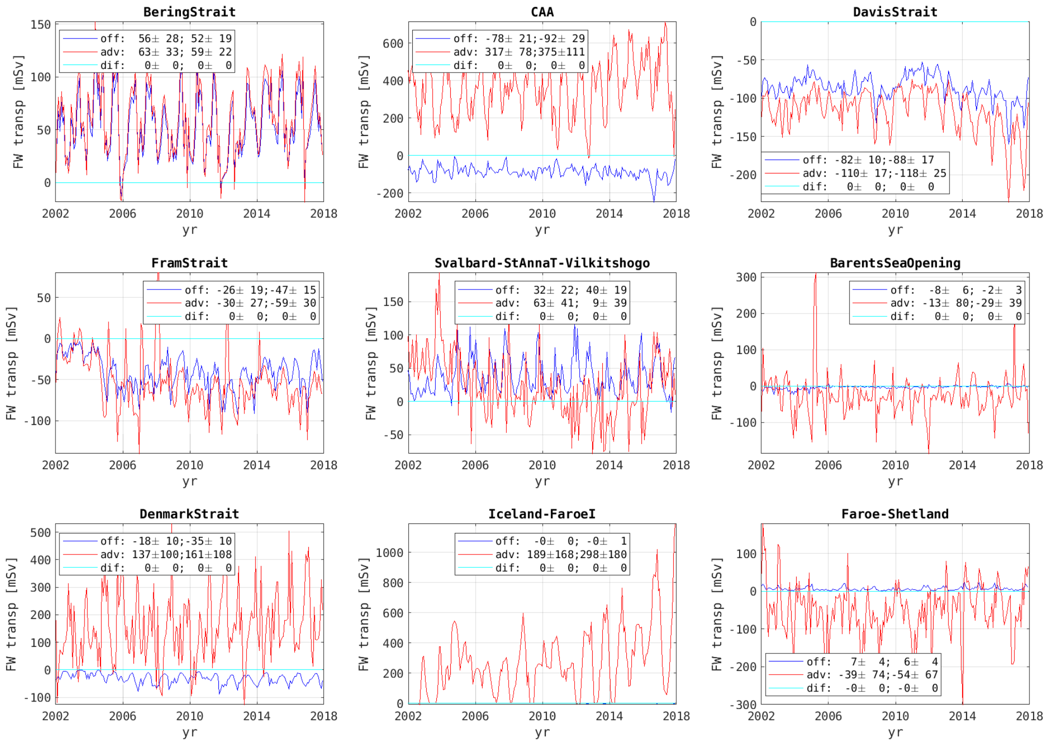

Figure B2. Time series of ocean freshwater transports (assuming a reference salinity $S_r = 34.8$) across important Arctic Mediterranean gateways using online (eqn. B3.0) and offline (eqn. B3.2) methods. Both methods incur errors due to reliance of the monthly $\langle S \rangle$ for determining the depth of the reference isohaline z_{S_r} serving as the integral limit. “off” refers to eqn. (B3.2) which computes the transport offline using outputs of monthly-averaged Eulerian velocity $\langle \mathbf{u}_E \rangle$ and salinity $\langle S \rangle$. “adv” and “dif” are the approximated online calculations of advective ($F_{FW_S,adv}$) and diffusive ($F_{FW_S,dif}$) terms on the RHS of eqn. (B3.0). The quantities listed in the legend are the 2002–2006 and 2007–2017 means and month-to-month variability. The variability is computed after the seasonal cycle has been removed. Note that “adv” is consistently larger than “off” (and with larger variability), but it is not possible to conclude that the online calculation is superior due to imperfect treatment of z_{S_r}. Instead, we assume higher confidence in both our FW flux estimation and our FW flux comparisons where “adv” and ”off” converge.

Gate	FW Transports [mSv]	
(1)Bering Strait	$^{a}61.32 \pm 23.82$	$^{b}54.24 \pm 20.62$
(2)CAA	372.06 ± 109.98	-94.19 ± 31.60
(3)Fram Strait	-96.56 ± 34.85	-84.83 ± 23.29
(4)Svalbard–FJL[1]–SZ[2]	14.60 ± 43.37	45.23 ± 31.14
(5)Barents Sea Opening	-30.15 ± 38.18	-3.25 ± 3.30
(6)Davis Strait	-133.47 ± 26.66	-103.32 ± 19.59
(7)Denmark Strait	153.85 ± 106.71	-42.61 ± 12.21
(8)Iceland–Faroe	297.85 ± 178.35	-0.29 ± 0.69
(9)Faroe–Shetland	-53.61 ± 64.84	6.25 ± 4.29
(10)Newfoundland-Gr	-441.55 ± 242.66	-110.67 ± 23.44
(11)48.3°N	-119.30 ± 38.67	-111.60 ± 22.80

Table B1. *ASTE_R1* Transports of freshwater (S_r=34.8 ppt) for the combined ocean and ice system for the period 2006–2017. FW fluxes are estimated using ^{a}eqn. (B3.0) and ^{b}eqn. (B3.2). [1] Franz Josef Land, [2] Severnaya Zemlya.

.

Appendix C Watermass definition in *ASTE_R1*

Suitable specification of the characteristic salinity, potential temperature and density (S, θ, σ) defining known watermasses can differ between observations and models due to model biases, as shown in Fig. 14 in the main text for water properties in the Irminger and Labrador Seas. Watermasses can be clearly identified in *ASTE_R1* as large volumes with a common formation history and distinct properties from surrounding waters, consistent with their definition in the literature. However in regions of hydrographic bias, these watermasses will not be identified – or correctly quantified – as their observed counterparts if they are tracked following the observed values too strictly. In this appendix, we summarize the choices made in determining watermass and explore the sensitivity to these choices where appropriate.

C1 Volume transports of watermass

Table C1 lists the watermass properties at Fram Strait (FS) and across the Greenland-Scotland Ridge (GSR) used to identify the transports reported in Fig. 15 in the main text. At the FS, the mean transports can be decomposed approximately into the West Spitsbergen Current (WSC, east of 5°E, Beszczynska-Möller et al., 2012), recirculated Atlantic Water (AW) (between 3.2°W and 5°E), and the East Greenland Current (EGC, west of 3.2°W, $S \leq 34$ ppt, $T \leq 1$°C). At the GSR definitions of watermasses such as the surface outflow, dense outflow, modified water, and inflow AW from Østerhus et al. (2019) and Hansen and Østerhus (2000) can be problematic when strictly applied to grid-scale average quantities. For example, the densewater in the outflow through Denmark Strait (DS) is defined in Østerhus et al. (2019) as having density anomaly $\sigma_\theta >$ 27.8, but in *ASTE_R1* outflow at the lowest depths of the strait are characterized by a lower bound of σ_θ ranging between 27.28 and 27.81. For this range, the corresponding southward transports are -1.6 ± 0.9 to 0.5 ± 0.3 Sv (see Fig. 15, blue color text). Similarly, over the Iceland-Faroe (IF) ridge, the southward transports of densewater defined by $\sigma_\theta \geq 22.44$ or $\sigma_\theta \geq 27.55$ in *ASTE_R1* yield a range of -0.4 to -0.3 Sv, compared to -0.4 ± 0.3 Sv of water with $\sigma_\theta \geq 27.8$ in Østerhus et al. (2019). Similar considerations applied also to dense water properties at the Faroe-Shetland (FSh) ridge ($\sigma_\theta \geq$ 27.81 in *ASTE_R1* compared to 27.8 in Østerhus et al., 2019). For the northward flow, in addition to salinity thresholds (S $\geq$ [34.8,35,35.25] ppt), temperature thresholds of $\theta \geq$

[5,4,5]°C are used in *ASTE_R1* to identify the warm AW across the DS, IF, and FSh channels.

Gate	Watermass	Properties		Reference
		Obs	ASTE	
FS	WSC	lon $> 5°$E, $T \geq 2°$C, $\sigma_\theta \sim 27.97$ kg/m^3	lon≥4°E, T≥2°C	Beszczynska-Möller et al. (2012), Schauer and Beszczynska-Möller (2009)
	Recirc AW	$-2.5°$E<lon<5°E	$-3.2°$E<lon<4°E, T≥ 1°C, S>34 ppt	Beszczynska-Möller et al. (2012)
	deep AW return flow	lon< $-3°$E	$-3.2°$E<lon<4°E, T<1°C, S>34 ppt	Beszczynska-Möller et al. (2012)
	EGC	lon< $-1°$E	lon< $-3.2°$E S<34 ppt T≤1°C	de Steur et al. (2014)
DS	inflow AW	–	S>34.8 ppt T>5	Østerhus et al. (2019)
	dense outflow	σ_θ >27.8 kg/m^3	S>34.5,34.8 ppt T<3.5°C σ_θ >27.44,27.81 kg/m^3	
	surface outflow	σ_θ <27.8 kg/m^3	S≤34.5 ppt	
IF	inflow AW	–	S>35 ppt T>5°C	Østerhus et al. (2019)
	dense outflow	σ_θ >27.8 kg/m^3	35≥S>34.5,34.7 ppt T≤4,5°C σ_θ >27.44,27.55 kg/m^3	
FSh	inflow AW	–	S>35.25 ppt T>5°C σ_θ >27.87 kg/m^3	Østerhus et al. (2019)
	dense outflow	σ_θ >27.8 kg/m^3	35≥S>34.8 ppt T≤2°C σ_θ >27.81,27.97 kg/m^3	

Table C1. Watermass at important Arctic Mediterranean gateway defined based on observations and in *ASTE_R1* .

C2 Heat content of upper halocline watermass

The upper halocline watermass, defined by Timmermans et al. (2018) as a layer within lower and upper salinity bounds of S_l=31.0 ppt and S_u=33.0 ppt, respectively, was identified based on subsurface in situ observations with fine vertical sampling resolution. In *ASTE_R1* , with vertical grid spacing of 15–20 m within the water column depths 50–160 m, average salinity in the water column changes more abruptly than in the observations. For more accurate estimation of halocline-integrated quantities one approach is to "interpolate" the salinity in the vertical to a finer grid to find the exact depths at which salinity fits within the given bounds. Though this is often done during model-data comparisons (e.g., Grabon, 2020), the interpolation introduces additional information that was not strictly solved for by the model. An alternate approach is to vary the salinity bounds to gauge the sensitivity of the heat content within this watermass to the vertical discretization in the model. As an example, Fig. C1 shows a vertical section in *ASTE_R1* through the Beaufort Gyre region as defined in Timmermans et al. (2018), with the watermass bounded between a temperature maximum at depths ∼50–60 m (Pacific Summer Water, PSW, S_l=31 salinity contour) and a temperature minimum at depths ∼150 m (Pacific Winter Water, PWW, S_u=33). In *ASTE_R1* , negligible sensitivity is found with changes to S_u, but the heat content within the upper halocline in this region changes by approximately 1–2.5% per 0.1 ppt change in S_l. A change in S_l of ∼0.5 ppt corresponds approximately to one depth level in *ASTE_R1* , and the heat content change associated with this is shown in shade in Fig. 18 in the main text.

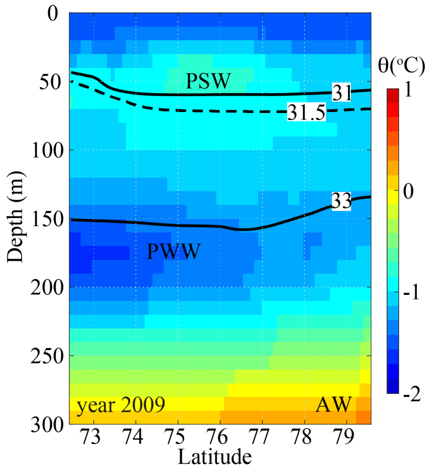

Figure C1. Vertical mean temperature for the year 2009 in a section across the Beaufort Gyre. Salinity contours are shown in black with white label, with the upper halocline watermass defined based on Timmermans et al. (2018) as bounded by S_l=31 ppt (through the temperature maximum associated with the Pacific Summer Water PSW) and S_u=33 ppt (through the temperature minimum associated with the Pacific Winter Water PWW). A change of S_l by 0.5 ppt corresponds approximately to 1 vertical depth level change in *ASTE_R1* .

Acknowledgments

This work was supported by NSF-OPP-1603903, NSF-OPP-1708289, and NSF-OCE-1924546. Additional funding was provided from the ECCO project through a JPL/Caltech subcontract. Computing resources were provided by the University of Texas at Austin Texas Advanced Computing Center (TACC) and NASA Advanced Supercomputing Division at the Ames Research Center. Adjoint code was generated using the TAF software tool, created and maintained by FastOpt GmbH (http://www.fastopt.com/). The *ASTE_R1* model configuration, inputs, and monthly and daily outputs are available at the Arctic Data Center https://arcticdata.io and mirrored at https://web.corral.tacc.utexas.edu/OceanProjects/ASTE/ and Amazon Web Services provided by TACC at http://aste-release1.s3-website.us-east-2.amazonaws.com/. Author ATN thanks M.-L. Timmermans and N. Foukal for providing heat content time-series for the Arctic halocline and eastern SPNA, and W. von Appen for the 2012–2017 processed Fram Strait mooring data used for ASTE post validation. We thank three anonymous reviewers for comments that greatly improved the manuscript.

References

Abernathey, R., Dussin, R., Smith, T., Bourgault, P., Bot, S., Doddridge, E., . . . Losch, M. (2020, November). *Mitgcm/xmitgcm: v0.5.0.* Zenodo. Retrieved from `https://doi.org/10.5281/zenodo.4288974` doi: 10.5281/zenodo.4288974

Abernathey, R. P., Busecke, J., Smith, T., Bot, S., Banihirwe, A., Zhang, C., . . . Rath, W. (2020, October). *xgcm/xgcm: v0.5.1.* Zenodo. Retrieved from `https://doi.org/10.5281/zenodo.4097223` doi: 10.5281/zenodo.4097223

Abernathey, R. P., Cerovecki, I., Holland, P. R., Newsom, E., Mazloff, M., & Talley, L. D. (2016). Water-mass transformation by sea ice in the upper branch of the Southern Ocean overturning. *Nature Geoscience*. doi: 10.1038/NGEO2749

Adcroft, A., & Campin, J.-M. (2004). Rescaled height coordinates for accurate representation of free-surface flows in ocean circulation models. *Ocean Modelling*, *7*(2004), 269–284. doi: 10.1016/j.ocemod.2003.09.003

Adcroft, A., Campin, J.-M., Dutkiewicz, S., Evangelinos, C., Ferreira, D., Forget, G., . . . Molod, A. (2018). *MITgcm user manual.* doi: 1721.1/117188

Adcroft, A., Campin, J.-M., Hill, C., & Marshall, J. (2004). Implementation of an atmosphere-ocean general circulation model on the expanded spherical cube. *Mon. Wea. Rev.*, *132*(12), 2845–2863.

Adcroft, A., Hill, C., & Marshall, J. (1997). Representation of topography by shaved cells in a height coordiate ocean model. *Mon. Wea. Rev.*, *125*, 2293–2315.

Adler, R., Sapiano, M. R. P., Huffman, G. J., Wang, J.-J., Gu, G., Bolvin, D., . . . Shin, D.-B. (2018). The Global Precipitation Climatology Project (GPCP) Monthly Analysis (New Version 2.3) and a Review of 2017 Global Precipitation. *Atmosphere*, *9*(138). doi: https://doi.org/10.3390/atmos9040138

Andersen, O. B., P., K., & L., S. (2015). The DTU13 MSS (Mean Sea Surface) and MDT (Mean Dynamic Topography) from 20 Years of Satellite Altimetry. In J. S. & B. R. (Eds.), *Igfs 2014. international association of geodesy symposia.* Springer, Cham. doi: 10.1007/1345_2015_182

Antonov, J. I., Seidov, D., Boyer, T. P., Locarnini, R. A., Mishonov, A. V., Garcia, H. E., . . . Johnson, D. R. (2010). Volume 2: Salinity. In S. Levitus (Ed.), . NOAA Atlas NESDIS 68, U.S. Government Printing Office, Washington, D.C.

Årthun, M., & Eldevik, T. (2016). On anomalous ocean heat transport toward the Arctic and associated climate predictability. *J. Clim.*, *29*, 689–704. doi: 10.1175/JCLI-D-15-0448.1

Asbjørnsen, H., Årthun, M., Skagseth, Ø., & Eldevik, T. (2019). Mechanisms of ocean heat anomalies in the norwegian sea. *Journal of Geophysical Research: Oceans*, *124*(4), 2908-2923. Retrieved from `https://agupubs.onlinelibrary.wiley.com/doi/abs/10.1029/2018JC014649` doi: 10.1029/2018JC014649

Balmaseda, M. A., Hernandez, F., Storto, A., Palmer, M. D., Alves, O., Shi, L., . . . Gaillard, F. (2015). The Ocean Reanalyses Intercomparison Project (ORA-IP). *Journal of Operational Oceanography*, *8*(sub1), s80–s97. doi: 10.1080/1755876X.2015.1022329

Bamber, J. L., Tedstone, A. J., King, M. D., Howat, I. M., Enderlin, E. M., van den Broeke, M. R., & Noel, B. (2018). Land ice freshwater budget of the Arctic and North Atlantic Oceans: 1. Data, methods, and results. *Journal of Geophysical Research*, *123*, 1827–1837. doi: 10.1002/2017JC013605

Bamber, J. L., van den Broeke, M., Ettema, J., Lenaerts, J., & Rignot, E. (2012). Recent large increases in freshwater fluxes from greenland into the North Atlantic. *Geophys. Res. Lett.*, *39*. doi: 10.1029/2012GL052552

Baringer, M. O., & Larsen, J. C. (2001). Sixteen years of Florida Current transport at 27°N. *Geophys. Res. Lett.*, *28*(16), 3179–3182. doi: 10.1029/2001GL013246

Bauch, D., Dmitrenko, I. A., Wegner, C., Hölemann, J., Kirillov, S. A., Timokhov, L. A., & Kassens, H. (2009). Exchange of laptev sea and arctic ocean halocline waters in response to atmospheric forcing. *J. Geophys. Res.*, *114*(C05008). (doi:10.1029/2008JC005062)

Bauch, D., van der Loeff, M. R., Andersen, N., Torres-Valdes, S., Bakker, K., & Abrahamsen, E. (2011). Origin of freshwater and polynya water in the arctic ocean halocline in summer 2007. *Progress in Oceanography*, *91*, 482–495. (doi:10.1016/j.pocean.2011.07.017)

Baumann, T. M., Polyakov, I. V., Pnyushkov, A. V., Rember, R., Ivanov, V. V., Alkire, M. B., ... Carmack, E. C. (2018, 06). On the seasonal cycles observed at the continental slope of the eastern Eurasian Basin of the Arctic Ocean. *Journal of Physical Oceanography*, *48*(7), 1451-1470. Retrieved from `https://doi.org/10.1175/JPO-D-17-0163.1` doi: 10.1175/JPO-D-17-0163.1

Beaird, N. L., Straneo, F., & Jenkins, W. (2018). Export of strongly diluted Greenland meltwater from a major glacial fjord. *Geophysical Research Letters*, *45*, 4163–4170. doi: 10.1029/2018GL077000

Bebieva, Y., & Timmermans, M.-L. (2016). An examination of double-diffusive processes in a mesoscale eddy in the Arctic Ocean. *Journal of Geophysical Research*, *121*, 457–475. doi: 10.1002/2015JC011105

Beesley, J. A., Bretherton, C. S., Jakob, C., Andreas, E. L., Intrieri, J. M., & Uttal, T. A. (2000). A comparison of cloud and boundary layer variables in the ECMWF forecast model with observations at Surface Heat Budget of the Arctic Ocean (SHEBA) ice camp. *J. Geophys. Res.*, *105*(D10), 12337–12349.

Bengtsson, L., Hagemann, S., & Hodges, K. I. (2004). Can climate trends be calculated from reanalysis data? *Journal of Geophysical Research: Oceans*, *109*(D11111). doi: 10.1029/2004JD004536

Beszczynska-Möller, A., Fahrbach, E., Schauer, U., & Hansen, E. (2012). Variability in Atlantic water temperature and transport at the entrance to the Arctic Ocean, 1997–2010. *ICES Journal of Marine Science*. doi: 10.1093/icesjms/fss056

Beszczynska-Möller, A., Woodgate, R. A., Lee, C., Melling, H., & Karcher, M. (2011). A synthesis of exchanges through the main oceanic gateways to the Arctic Ocean. *Oceanography*, *24*(3), 82–99. doi: http://dx.doi.org/10.5670/oceanog.2011.59

Bigdeli, A., Loose, B., Nguyen, A. T., & Cole, S. T. (2017). Numerical investigation of the Arctic ice-ocean boundary layer and implications for air-sea gas fluxes. *Ocean Sci.*, *13*, 61–75. doi: 10.5194/os-13-61-2017

Bigdeli, A., Nguyen, A. T., Pillar, H. R., na, V. O., & Heimbach, P. (2020). Atmospheric warming drives growth in Arctic sea-ice: A key role for snow. *Geophysical Research Letters*. (submitted)

Buckley, M. W., Ponte, R. M., Forget, G., & Heimbach, P. (2014). Low-frequency SST and upper-ocean heat content variability in the North Atlantic. *J. Climate*, *27*(13), 4996–5018. doi: 10.1175/JCLI-D-13-00316.1

Buckley, M. W., Ponte, R. M., Forget, G., & Heimbach, P. (2015). Determining the origins of advective heat transport convergence variability in the North Atlantic. *J. Climate*, *28*, 3943–3956. doi: 10.1175/JCLI-D-14-00579.1

Campin, J.-M., Adcroft, A., Hill, C., & Marshall, J. (2004). Conservation of properties in a free-surface model. *Ocean Modelling*, *6*, 221–244. doi: 10.1016/S1463-5003(03)00009-X

Carmack, E. C., Yamamoto-Kawai, M., Haine, T. W. N., Bacon, S., Bluhm, B. A., Lique, C., ... Williams, W. J. (2016). Freshwater and its role in the Arctic marine system: Sources, disposition, storage, export, and physical and biogeochemical consequences in the Arctic and global oceans. *Journal of Geophysical Research: Biogeosciences*, *121*(3), 675-717. doi: 10.1002/2015JG003140

Carton, J. A., Penny, S. G., & Kalnay, E. (2019, 04). Temperature and salinity variability in the SODA3, ECCO4r3, and ORAS5 ocean reanalyses, 1993–2015. *Journal of Climate*, *32*(8), 2277-2293. Retrieved from `https://doi.org/`

10.1175/JCLI-D-18-0605.1 doi: 10.1175/JCLI-D-18-0605.1

Chassignet, E. P., & Garraffo, Z. D. (2001). Viscosity parameterization and the Gulf Stream separation. In P. Muller & D. Henderson (Eds.), *From stirring to mixing in a stratified ocean* (pp. 37–41).

Chassignet, E. P., & Marshall, D. P. (2013). Gulf stream separation in numerical ocean models. In *Ocean modeling in an eddying regime* (p. 39-61). American Geophysical Union (AGU). doi: 10.1029/177GM05

Chassignet, E. P., & Xu, X. (2017). Impact of horizontal resolution (1/12° to 1/50°) on Gulf Stream separation, penetration, and variability. *Journal of Physical Oceanography*, *47*, 1999–2021. doi: 10.1175/JPO-D-17-0031.1

Chaudhuri, A. H., Ponte, R. M., Forget, G., & Heimbach, P. (2013). A Comparison of Atmospheric Reanalysis Surface Products over the Ocean and Implications for Uncertainties in Air–Sea Boundary Forcing. *J. Climate*, *26*(1), 153–170. doi: 10.1175/JCLI-D-12-00090.1

Chaudhuri, A. H., Ponte, R. M., & Nguyen, A. T. (2014). A comparison of atmospheric reanalysis products for the Arctic Ocean and implications for uncertainties in air–sea fluxes. *J. Climate*, *27*(14), 5411–5421. doi: 10.1175/JCLI-D-13-00424.1

Cole, S. T., Timmermanns, M.-L., Toole, J. M., Krishfield, R. A., & Thwaites, F. T. (2014). Ekman veering, internal waves, and turbulence observed under Arctic sea ice. *J. Phys. Oceanogr.*, *44*, 1306–1328.

Curry, B., Lee, C., & Petrie, B. (2011). Volume, freshwater, and heat fluxes through Davis Strait, 2004–05. *Journal of Physical Oceanography*, *41*, 429–436. doi: 10.1175/2010JPO4536.1

Curry, B., Lee, C., Petrie, B., Moritz, R. E., & Kwok, R. (2014). Multiyear volume, liquid freshwater, and sea ice transports through Davis Strait, 2004–10. *Journal of Physical Oceanography*, *44*, 1244–1266. doi: 10.1175/JPO-D-13-0177.1

Dee, D. P., Uppala, S. M., Simmons, A. J., Berrisford, P., Poli, P., Kobayashi, S., ... Vitart, F. (2011). The ERA-Interim reanalysis: configuration and performance of the data assimilation system. *Q. J. R. Meteorol. Soc.*, *137*(656), 553–597.

Dengg, J. (1993). The problem of Gulf Stream separation: A barotropic approach. *Journal of Physical Oceanography*, *23*(10), 2182-2200. doi: 10.1175/1520-0485(1993)023⟨2182:TPOGSS⟩2.0.CO;2

de Steur, L., Hansen, E., Gerdes, R., Karcher, M., Fahrbach, E., & Holfort, J. (2009). Freshwater fluxes in the East Greenland current: A decade of observations. *Geophys. Res. Lett.*, *36*(L23611). doi: 10.1029/2009GL041278

de Steur, L., Hansen, E., Mauritzen, C., Beszczynska-Möller, A., & Fahrbach, E. (2014). Impact of recirculation on the East Greenland Current in Fram Strait: Results from moored current meter measurements between 1997 and 2009. *Deep Sea Res.*, *92*, 26–40. doi: 10.1016/j.dsr.2014.05.018

de Steur, L., Peralta Ferriz, C., & Pavlova, O. (2018). Freshwater export in the East Greenland Current freshens the North Atlantic. *Geophysical Research Letters*, *45*(24), 13359–13366. doi: 10.1029/2018GL080207

Dmitrenko, I. A., Ivanov, V. V., Kirillov, S. A., Vinogradova, E. L., Torres-Valdes, S., & Bauch, D. (2011). Properties of the Atlantic derived halocline waters over the Laptev Sea continental margin: Evidence from 2002 to 2009. *J. Geophys. Res.*, *116*(C10024). doi: 10.1029/2011JC007269

Dmitrenko, I. A., Kirillov, S. A., Ivanov, V. V., Woodgate, R. A., Polyakov, I. V., Koldunov, N., ... Timokhov, L. A. (2009). Seasonal modification of the Arctic Ocean intermediate water layer off the eastern Laptev Sea continental shelf break. *Journal of Geophysical Research: Oceans*, *114*(C6). Retrieved from https://agupubs.onlinelibrary.wiley.com/doi/abs/10.1029/2008JC005229 doi: 10.1029/2008JC005229

Docquier, D., Grist, J. P., Roberts, M. J., Roberts, C. D., Semmler, T., Ponsoni, L., ... Fichefet, T. (2019). Impact of model resolution on Arctic sea ice and

North Atlantic Ocean heat transport. *Climate Dynamics*, *53*, 4989–5017. doi: 10.1007/s00382-019-04840-y

Drange, H., Gerdes, R., Gao, Y., Karcher, M., Kauker, F., & Bentsen, M. (2005). Ocean general circulation modelling of the Nordic Seas. In H. Drange, T. Dokken, T. Furevik, R. Gerdes, & W. Berger (Eds.), *From the Nordic Seas: An integrated perspective* (Vol. 158, pp. 199–220). American Geophysical Union, Washington DC: AGU Monograph.

Dukhovskoy, D. S., Myers, P. G., Platov, G., Timmermans, M.-L., Curry, B., Proshutinsky, A., . . . Somavilla, R. (2016). Greenland freshwater pathways in the sub-Arctic seas from model experiments with passive tracers. *Journal of Geophysical Research: Oceans*, *121*(1), 877-907. doi: 10.1002/2015JC011290

Dukhovskoy, D. S., Yashayaev, I., Proshutinsky, A., Bamber, J. L., Bashmachnikov, I. L., Chassignet, E. P., . . . Tedstone, A. J. (2019). Role of Greenland freshwater anomaly in the recent freshening of the subpolar North Atlantic. *Journal of Geophysical Research: Oceans*, *124*(5), 3333-3360. doi: 10.1029/2018JC014686

Ezer, T. (2016). Revisiting the problem of the Gulf Stream separation: on the representation of topography in ocean models with different types of vertical grids. *Ocean Modelling*, *104*, 15–27. doi: 10.1016/j.ocemod.2016.05.008

Fahrbach, E., Meincke, J., Osterhus, S., Rohardt, G., Schauer, U., Tverberg, V., & Verduin, J. (2001). Direct measurements of volume transports through Fram Strait. *Polar Research*, *20*(2), 217–224.

Fenty, I., & Heimbach, P. (2013a). Coupled Sea Ice–Ocean-State Estimation in the Labrador Sea and Baffin Bay. *J. Phys. Oceanogr.*, *43*(5), 884–904. doi: 10.1175/JPO-D-12-065.1

Fenty, I., & Heimbach, P. (2013b). Hydrographic preconditioning for seasonal sea ice anomalies in the labrador sea. *J. Phys. Oceanogr.*, *43*(5), 863–883. doi: 10.1175/JPO-D-12-064.1

Fenty, I., Menemenlis, D., & Zhang, H. (2015). Global coupled sea ice-ocean state estimate. *Clim. Dyn.*. doi: 10.1007/s00382-015-2796-6

Fer, I. (2014). Near-inernal mixing in the central Arctic Ocean. *J. Phys. Oceanogr.*, *44*, 2031–2049. doi: 10.1175/JPO-D-13-0133.1

Forget, G., Campin, J.-M., Heimbach, P., Hill, C. N., Ponte, R. M., & Wunsch, C. (2015a). ECCO version 4: an integrated framework for non-linear inverse modeling and global ocean state estimation. *Geosci. Model Dev. Discuss.*, *8*(5), 3653–3743.

Forget, G., Ferreira, D., & Liang, X. (2015b). On the observability of turbulent transport rates by argo: supporting evidence from an inversion experiment. *Ocean Sciences Diss.*, *12*(3), 1107–1143.

Forget, G., & Wunsch, C. (2007). Global hydrographic variability and the data weights in ocean state estimates. *J. Phys. Oceanogr.*, *37*, 1997–2008.

Foukal, N. P., & Lozier, M. S. (2018). Examining the origins of ocean heat content variability in the eastern North Atlantic subpolar gyre. *Geophysical Research Letters*, *45*, 11,275–11,283. doi: https://doi.org/10.1029/2018GL079122

Fournier, S., Lee, T., Tang, W., Steele, M., & Omeldo, E. (2019). Evaluation and intercomparison of SMOS, Aquarius and SMAP sea surface salinity products in the Arctic Ocean. *Remote Sensing*, *11*(3043). doi: 10.3390/rs11243043

Fowler, C., Emery, W., & Tschudi, M. (2013). *Polar pathfinder daily 25 km ease-grid sea ice motion vectors. version 2, northern hemisphere* (Tech. Rep.). Boulder, Colorado, USA: National Snow and Ice Data Center. (NSIDC Technical Report)

Fox-Kemper, B., & Menemenlis, D. (2008). Can large eddy simulation techniques improve mesoscale rich ocean models? In M. W. Hecht & H. Hasumi (Eds.), *Ocean modeling in an eddying regime* (pp. 319–337). Washington, D. C.: American Geophysical Union.

Freville, H., Brun, E., Picard, G., Tatarinova, N., Arnaud, L., Lanconelli, C., ... van den Broeke, M. (2014). Using MODIS land surface temperatures and the Crocus snow model to understand the warm bias of ERA-Interim reanalyses at the surface in Antarctica. *The Cryosphere*, *8*, 1361–1373. doi: 10.5194/tc-8-1361-2014

Fukumori, I., Fenty, I., Forget, G., Heimbach, P., King, C., Nguyen, A., ... Wang, O. (2018b). *Data sets used in ECCO Version 4 Release 3.* Retrieved from `http://hdl.handle.net/1721.1/120472`

Fukumori, I., Heimbach, P., Ponte, R. M., & Wunsch, C. (2018a). A dynamically consistent, multi-variable ocean climatology. *Bulletin of the American Meteorological Society*, *0*(0), null. (in press) doi: 10.1175/BAMS-D-17-0213.1

Gent, P. R., & McWilliams, J. C. (1990). Isopycnal mixing in ocean circulation models. *J. Phys. Oceanogr.*, *20*, 150–155.

Germe, A., Houssais, M., Herbaut, C., & Cassou, C. (2011). Greenland Sea sea ice variability over 1979–2007 and its link to the surface atmosphere. *J. Geophys. Res.*, *116*(C10034). doi: 10.1029/2011JC006960

Giering, R., Kaminski, T., & Slawig, T. (2005, October). Generating efficient derivative code with TAF. *Future Generation Computer Systems*, *21*(8), 1345–1355.

Gilbert, J., & Lemaréchal, C. (1989). Some numerical experiments with variable-storage quasi-newton algorithms. *Math. Program.*, *45*(B), 407-435.

Gopalakrishnan, G., Cornuelle, B. D., Hoteit, I., Rudnick, D. L., & Owens, W. B. (2013). State estimates and forecasts of the loop current in the Gulf of Mexico using the MITgcm and its adjoint. *Journal of Geophysical Research: Oceans*, *118*(7), 3292-3314. doi: 10.1002/jgrc.20239

Grabon, J. S. (2020). *An analysis of Atlantic Water in the Arctic Ocean using the Arctic Subpolar gyre sTate Estimate and observations* (Unpublished master's thesis). Massachusetts Institute of Technology, Cambridge, MA, USA. (90pp)

Griffies, S. M. (2004). *Fundamentals of ocean climate models.* Princeton, NJ: Princeton University Press. (518pp)

Griffies, S. M., Yin, J., Durack, P. J., Goddard, P., Bates, S. C., Behrens, E., ... Zhang, X. (2014). An assessment of global and regional sea level for years 1993–2007 in a suite of interannual CORE-II simulations. *Ocean Modelling*, *78*(C), 35–89. doi: 10.1016/j.ocemod.2014.03.004

Haine, T. W. N., Curry, B., Gerdes, R., Hansen, E., Karcher, M., Lee, C., ... Woodgate, R. A. (2015). Arctic freshwater export: Status, mechanisms, and prospects. *Global Planet. Change*, *125*, 13–35. doi: https://doi.org/10.1016/j.gloplacha.2014.11.013

Hansen, B., Larsen, K. M. H., Hátún, H., Kristiansen, R., Mortensen, E., & Østerhus, S. (2015). Transport of volume, heat, and salt towards the Arctic in the Faroe Current 1993–2013. *Ocean. Sci.*, *11*, 743. doi: https://doi.org/10.5194/os-11-743-2015

Hansen, B., & Østerhus, S. (2000). North Atlantic–Nordic Seas exchanges. *Progress in Oceanography*, *45*(2), 198–208. doi: https://doi.org/10.1016/S0079-6611(99)00052-X

Hattermann, T., Isachsen, P. E., Appen, W.-J., Albretsen, J., & Sundfjord, A. (2016, April). Eddy-driven recirculation of Atlantic Water in Fram Strait. *Geophysical Research Letters*, *43*(7), 3406–3414.

Heimbach, P., Fukumori, I., Hill, C. N., Ponte, R. M., Stammer, D., Wunsch, C., ... Zhang, H. (2019, March). Putting It All Together: Adding Value to the Global Ocean and Climate Observing Systems With Complete Self-Consistent Ocean State and Parameter Estimates. *Frontiers in Marine Science*, *6*, 769–10.

Heimbach, P., Hill, C., & Giering, R. (2005). An efficient exact adjoint of the parallel MIT general circulation model, generated via automatic differentiation. *Future Generation Computer Systems*, *21(8)*, 1356–1371. doi: 10.1016/j.future.2004.11.010

Heimbach, P., Menemenlis, D., Losch, M., Campin, J.-M., & Hill, C. (2010). On the formulation of sea-ice models. Part 2: Lessons from multi-year adjoint sea-ice export sensitivities through the Canadian Arctic Archipelago. *Ocean Modelling*, *33*(1-2), 145–158. doi: 10.1016/j.ocemod.2010.02.002

Heuzé, C., & Årthun, M. (2019). The Atlantic inflow across the Greenland-Scotland ridge in global climate models (CMIP5). *Elem. Sci. Anth.*, *7*(16). doi: https://doi.org/10.1525/elementa.354

Holloway, G., Dupont, F., Golubeva, E., Hakkinen, S., Hunke, E., Jin, M., ... Zhang, J. (2007). Water properties and circulation in arctic ocean models. *J. Geophys. Res.*, *112*(C04S03). doi: 10.1029/2006JC003642

Holmes, R. M., Coe, M. T., Fiske, G. J., Gurtovaya, T., McClelland, J. W., Shiklomanov, A. I., ... Zhulidov, A. V. (2012). Climate change impacts on the hydrology and biogeochemistry of Arctic rivers. In *Climatic change and global warming of inland waters* (p. 1-26). John Wiley & Sons, Ltd. doi: https://doi.org/10.1002/9781118470596.ch1

Ilicak, M., Drange, H., Wang, Q., Gerdes, R., Aksenov, Y., Bailey, D., ... Yeager, S. G. (2016). An assessment of the Arctic Ocean hydrography in a suite of interannual CORE-II simulations. part III: Hydrography and fluxes. *Ocean Modelling*, *100*, 141–161. doi: 10.1016/j.ocemod.2016.02.004

Ivanov, V. V., Alexeev, V. A., Repina, I., Koldunov, N. V., & Smirnov, A. (2012). Tracing Atlantic water signature in the Arctic sea ice cover east of Svalbard. *Advances in Meteorology*, *2012*. doi: 10.1155/2012/201818

Jackson, J. M., Carmack, E. C., McLaughlin, F. A., Allen, S. E., & Ingram, R. G. (2010). Identification, characterization, and change of the nearsurface temperature maximum in the Canada Basin, 1993–2008. *J. Geophys. Res.*, *115*(C05021). doi: 10.1029/2009JC005265

Jahn, A., Aksenov, Y., de Cuevas, B. A., de Steur, L., Häkkinen, S., Hansen, E., ... Zhang, J. (2012). Arctic ocean freshwater: How robust are model simulations? *Journal of Geophysical Research: Oceans*, *117*(C8). doi: 10.1029/2012JC007907

Jakobson, E., Vihma, T., Palo, T., Jakobson, L., Keemik, H., & Jaagus, J. (2012). Validation of atmospheric reanalyses over the central Arctic Ocean. *Geophys. Res. Lett.*, *39*(L10802). doi: 10.1029/2012GL051591

Jakobsson, M., Mayer, L. A., Coakley, B., Dowdeswell, J. A., Forbes, S., Fridman, B., ... Weatherall, P. (2012). The International Bathymetric Chart of the Arctic Ocean (IBCAO) Version 3.0. *Geophysical Research Letters*. doi: 10.1029/2012GL052219

Janjić, T., Bormann, N., Bocquet, M., Carton, J. A., Cohn, S. E., Dance, S. L., ... Weston, P. (2017). On the representation error in data assimilation. *Quarterly Journal of the Royal Meteorological Society*, *144*(713), 1257–1278. doi: 10.1002/qj.3130

Jochum, M., Danabasoglu, G., Holland, M., Kwon, Y.-O., & Large, W. G. (2008). Ocean viscosity and climate. *Journal of Geophysical Research*, *113*(C6). doi: 10.1029/2007JC004515

Johns, W. E., Townsend, T. L., Fratantoni, D. M., & Wilson, W. D. (2002). On the Atlantic inflow to the Caribbean Sea. *Deep-Sea Research Part I: Oceanographic Research Papers*, *49*(2), 211–243. doi: 10.1016/S0967-0637(01)00041-3

Johnson, M., Gaffigan, S., Hunke, E., & Gerdes, R. (2007). A comparison of Arctic Ocean sea ice concentration amonth the coordinated AOMIP model experiments. *J. Geophys. Res.*, *112*(C04S11). doi: 10.1029/2006JC003690

JPL_MUR_MEaSUREs_Project. (2015). *GHRSST level 4 MUR global foundation sea surface temperature analysis (v4.1). ver. 4.1.* `https://doi.org/10.5067/GHGMR-4FJ04`. (Dataset Accessed: 2017-11-08) doi: 10.5067/GHGMR-4FJ04

Karcher, M., Smith, J. N., Kauker, F., Gerdes, R., & Jr., W. M. S. (2012). Recent changes in Arctic Ocean circulation revealed by iodine-129 observations and modeling. *J. Geophys. Res.*, *117*(C08007). doi: 10.1029/2011JC007513

Kinney, J. C., Maslowski, W., Aksenov, Y., de Cuevas, B., Nguyen, A. T., Osinski, R., … Zhang, J. (2014). On the flow through Bering Strait: a synthesis of model results and observations. In J. Grebmeier & W. Maslowski (Eds.), (pp. 167–198). Dordrecht: Springer Dordrecht.

Kobayashi, S., Ota, Y., Harada, Y., Ebita, A., Moriya, M., Onoda, H., … Takahashi, K. (2015). The JRA-55 Reanalysis: General Specifications and Basic Characteristics. *Journal of the Meteorological Society of Japan*, *93*(1), 5–48. doi: https://doi.org/10.2151/jmsj.2015-001

Köhl, A. (2020). Evaluating the GECCO3 1948-2018 ocean synthesis a configuration for initializing the MPIESM climate model. *Quarterly Journal of the Royal Meteorological Society*, *146*(730), 2250–2273. doi: 10.1002/qj.3790

Köhl, A., & Stammer, D. (2008, 05). Decadal Sea Level Changes in the 50-Year GECCO Ocean Synthesis. *Journal of Climate*, *21*(9), 1876-1890. doi: 10.1175/2007JCLI2081.1

Krishfield, R. A. (2020). pers. comm.

Krishfield, R. A., Toole, J. M., Proshutinsky, A., & Timmermans, M.-L. (2008). Automated ice-tethered profilers for seawater observations under pack ice in all seasons. *J. Atmos. Oceanic Technol.*, *25*(11), 2091–2105. doi: 10.1175/2008JTECHO587.1

Kwok, R., & Cunningham, G. F. (2008). Icesat over arctic sea ice: Estimation of snow depth and ice thickness. *J. Geophys. Res.*, *113*(C08010). (doi:10.1029/2008JC004753)

Kwok, R., & Cunningham, G. F. (2015). Variability of Arctic sea ice thickness and volume from CryoSat-2. *Phil. Trans. Royal Soc. A*, *373*. doi: 10.1098/rsta.2014.0157

Kwok, R., Cunningham, G. F., Wensnahan, M., Rigor, I., Zwally, H. J., & Yi, D. (2009). Thinning and volume loss of the arctic ocean sea ice cover: 2003-2008. *J. Geophys. Res.*, *114*(C07005). (10.1029/2009JC005312)

Kwok, R., & Morison, J. (2016, January). Sea surface height and dynamic topography of the ice-covered oceans from CryoSat-2: 2011-2014. *Journal of Geophysical Research: Oceans*, *121*(1), 674–692.

Lammers, R. B., & Shiklomanov, A. I. (2001). Assessment of contemporary Arctic river runoff based on observational discharge records. *J. Geophys. Res.*, *106*(D4), 3321.

Large, W. G., McWilliams, J., & Doney, S. (1994). Oceanic vertical mixing: A review and a model with nonlocal boundary layer parameterization. *Rev. Geophys.*, *32*, 363–403.

Large, W. G., & Yeager, S. G. (2008). The global climatology of an interannually varying air–sea flux data set. *Clim. Dyn.*, *33*(2–3), 341–364.

Lavergne, T., Sørensen, A. M., Kern, S., Tonboe, R., Notz, D., Aaboe, S., … Pedersen, L. T. (2019). Version 2 of the EUMETSAT OSI SAF and ESA CCI sea-ice concentration climate data records. *The Cryosphere*, *13*(1), 49–78. doi: 10.5194/tc-13-49-2019

Leith, C. E. (1968). Diffusion approximation for two-dimensional turbulence. *Phys. Fluids*, *10*, 1409–1416.

Leith, C. E. (1996). Stochastic models of chaotic systems. *Physica D*, *98*, 481–491.

Levitus, S. (Ed.). (2010). *World ocean atlas 2009*. NOAA Atlas NESDIS 68, U.S. Government Printing Office, Washington, D.C.

Liang, X., Piecuch, C. G., Ponte, R. M., Forget, G., Wunsch, C., & Heimbach, P. (2017). Change of the global ocean vertical heat transport over 1993-2010. *Journal of Climate*, *14*(30), 5319–5327. doi: 10.1175/jcli-d-16-0569.1

Lind, S., Ingvaldsen, R. B., & Furevik, T. (2018). Arctic warming hotspot in the northern Barents Sea linked to declining sea-ice import. *Nature climate change*, *8*, 634–639. doi: https://doi.org/10.1038/s41558-018-0205-y

Liu, C., Liang, X., Ponte, R. M., Vinogradova, N., & Wang, O. (2019). Vertical redistribution of salt and layered changes in global ocean salinity. *Nat. Commun.*, *10*(3445). doi: 10.1038/s41467-019-11436-x

Locarnini, R. A., Mishonov, A. V., Antonov, J. I., Boyer, T. P., Garcia, H. E., Baranova, O. K., … Johnson, D. R. (2010). Volume 1: Temperature. In S. Levitus (Ed.), . NOAA Atlas NESDIS 68, U.S. Government Printing Office, Washington, D.C.

Locarnini, R. A., Mishonov, A. V., Baranova, O. K., Boyer, T. P., Zweng, M. M., Garcia, H. E., … Smolyar, I. (2018). Volume 1: Temperature. In A. Mishonov (Ed.), . NOAA Atlas NESDIS 82, U.S. Government Printing Office, Washington, D.C.

Losch, M., Menemenlis, D., Campin, J.-M., Heimbach, P., & Hill, C. (2010). A dynamic-thermodynamic sea ice model for ocean climate modeling on an Arakawa C-grid: Part 1: Forward model sensitivities. *omod*, *33(1-2)*, 129-144. doi: 10.1016/j.ocemod.2009.12.008

Lozier, M. S., Bacon, S., Bower, A. S., Cunningham, S. A., Femke de Jong, M., de Steur, L., … Zika, J. D. (2017). Overturning in the Subpolar North Atlantic Program: a new international ocean observing system. *Bull. Amer. Meteor. Soc.*, *98*(4), 737–752.

Lozier, M. S., Li, F., Bacon, S., Bahr, F., Bower, A. S., Cunningham, S. A., … Zhao, J. (2019). A sea change in our view of overturning in the subpolar North Atlantic. *Science*, *363*(6426), 516–521. doi: 10.1126/science.aau6592

Lupkes, C., Vihma, T., Jakobson, E., Konig-Langlo, G., & Tetzlaff, A. (2010). Meteorological observations from ship cruises during summer to the central Arctic: A comparison with reanalysis data. *Geophys. Res. Lett.*, *37*(L09810). doi: 10.1029/2010GL042724

Manucharyan, G. E., & Isachsen, P. E. (2019). Critical role of continental slopes in halocline and eddy dynamics of the Ekman-driven Beaufort Gyre. *Journal of Geophysical Research*, *124*, 2679–2696. doi: 10.1029/2018JC014624

Marnela, M., Rudels, B., Goszczko, I., Beszczynska-Möller, A., & Schauer, U. (2016). Fram Strait and Greenland Sea transports, water masses, and water mass transformations 1999–2010 (and beyond). *Journal of Geophysical Research*, *121*(4), 2314–2346. doi: 10.1002/2015JC011312

Marshall, J., Adcroft, A., Hill, C., Perelman, L., & Heisey, C. (1997). A finite-volume, incompressible Navier stokes model for studies of the ocean on parallel computers. *J. Geophys. Res.*, *102*, 5753–5766.

Martin, T., Steele, M., & Zhang, J. (2014). Seasonality and long-term trend of Arctic Ocean surface stress in a model. *J. Geophys. Res.*, *119*, 1723–1738. doi: 10.1002/2013JC009425

Mashayek, A., Ferrari, R., Merrifield, S., Ledwell, J. R., St Laurent, L., & Garabato, A. N. (2017). Topographic enhancement of vertical turbulent mixing in the Southern Ocean. *Nat. Commun.*, *8*(14197). doi: 10.1038/ncomms14197

Mazloff, M. R., Heimbach, P., & Wunsch, C. (2010). An eddy-permitting Southern Ocean State Estimate. *Journal of Physical Oceanography*, *40*(5), 880-899. doi: 10.1175/2009JPO4236.1

Meneghello, G., Marshall, J., Cole, S. T., & Timmermans, M.-L. (2017). Observational inferences of lateral eddy diffusivity in the halocline of the Beaufort Gyre. *Geophysical Research Letters*, *44*(24), 12,331–12,338. doi: 10.1002/2017GL075126

Meneghello, G., Marshall, J., Timmermans, M.-L., & Scott, J. (2018, 04). Observations of seasonal upwelling and downwelling in the Beaufort Sea mediated by sea ice. *Journal of Physical Oceanography*, *48*(4), 795-805. doi: 10.1175/JPO-D-17-0188.1

Menemenlis, D., Hill, C., Adcroft, A., Campin, J.-M., Cheng, B., Ciotti, B., … Zhang, J. (2005). Towards eddy permitting estimates of the global ocean and sea-ice circulation. *EOS Transactions AGU*, *86*(9), 89.

Mishonov, A. (Ed.). (2018). *World ocean atlas 2018.* NOAA Atlas NESDIS 82, U.S. Government Printing Office, Washington, D.C.

Moore, G. W. K., Straneo, F., & Oltmanns, M. (2014). Trend and inter-annual variability in southeast Greenland sea ice: Impacts on coastal Greenland climate variability. *Geophys. Res. Lett.*, *41*, 8619–8626. doi: 10.1002/2014GL062107

Mu, L., Losch, M., Yang, Q., Ricker, R., Losa, S. N., & Nerger, L. (2018). Arcticwide sea ice thickness estimates from combining satellite remote sensing data and a dynamic iceocean model with data assimilation during the CryoSat2 period. *Journal of Geophysical Research: Oceans*, *123*, 7763–7780. doi: 10.1029/2018JC014316

Muilwijk, M., Smedsrud, L. H., Ilicak, M., & Drange, H. (2018). Atlantic water heat transport variability in the 20th century Arctic Ocean from a global ocean model and observations. *Journal of Geophysical Research: Oceans*, *123*(11), 8159-8179.

Munk, W. (1966). Abyssal recipes. *Deep Sea Research*, *13*, 707–730.

Nguyen, A. T., Heimbach, P., Garg, V. V., Ocaña, V., Lee, C., & Rainville, R. (2020a). Impact of synthetic Arctic Argo-type floats in a coupled ocean-sea ice state estimation framework. *J. Atmos. Ocean. Tech.*, *37*(8), 1477–1495. doi: 10.1175/JTECH-D-19-0159.1.

Nguyen, A. T., Menemenlis, D., & Kwok, R. (2011). Arctic ice-ocean simulations with optimized model parameters: approach and assessment. *J. Geophys. Res.*, *116*(C4), C04025. doi: 10.1029/2010JC006573

Nguyen, A. T., Ocaña, V., Garg, V. V., Heimbach, P., Toole, J. M., Krishfield, R. A., ... Rainville, R. (2017). On the benefit of current and future ALPS data for improving Arctic coupled ocean-sea ice state estimation. *Oceanography*, *30*(2), 69–73. (ALPS II Special Issue) doi: 10.5670/oceanog.2017.223

Nguyen, A. T., Pillar, H., Ocaña, V., Smith, T., & Heimbach, P. (2021a). *Arctic Subpolar gyre sTate Estimate Release 1 (ASTE_R1) data 2002–2017, monthly averages and snapshots, Arctic Data Center.* `https://doi.org/10.18739/A2CV4BS5K`.

Nguyen, A. T., Pillar, H., Ocaña, V., Smith, T., & Heimbach, P. (2021b). *Arctic Subpolar gyre sTate Estimate Release 1 (ASTE_R1) data 2002–2017, depth-integrated monthly averages and snapshots, Arctic Data Center.* `https://doi.org/10.18739/A2833N015`.

Nguyen, A. T., Pillar, H., Ocaña, V., Smith, T., & Heimbach, P. (2021c). *Arctic Subpolar gyre sTate Estimate Release 1 (ASTE_R1) data 2002–2017, daily averages, Arctic Data Center.* `https://doi.org/10.18739/A24B2X58W`.

Nguyen, A. T., Pillar, H., Ocaña, V., Smith, T., & Heimbach, P. (2021d). *Arctic Subpolar gyre sTate Estimate Release 1 (ASTE_R1) data 2002–2017, 12-month climatology, Arctic Data Center.* `https://doi.org/10.18739/A20P0WR8J`.

Nguyen, A. T., Pillar, H., Ocaña, V., Smith, T., & Heimbach, P. (2021e). *Arctic Subpolar gyre sTate Estimate Release 1 (ASTE_R1) data 2002–2017, in-situ profiles, Arctic Data Center.* `https://doi.org/10.18739/A2VX0643Z`.

Nguyen, A. T., Pillar, H., Ocaña, V., Smith, T., & Heimbach, P. (2021f). *Arctic Subpolar gyre sTate Estimate Release 1 (ASTE_R1) data 2002–2017, Grid files, Documentations and post-processing toolbox, Arctic Data Center.* `https://doi.org/10.18739/A2MC8RH3V`.

Nguyen, A. T., Pillar, H., Ocaña, V., Smith, T., & Heimbach, P. (2021g). *Arctic Subpolar gyre sTate Estimate Release 1 (ASTE_R1) data 2002–2017, rerun_ASTE_R1, Arctic Data Center.* `https://doi.org/10.18739/A2R49G98G`.

Nguyen, A. T., Woodgate, R. A., & Heimbach, P. (2020b). Elucidating large-scale atmospheric controls on Bering Strait throughflow variability using a data-constrained ocean model and its adjoint. *J. Geophys. Res.*, *125*. doi: 10.1029/2020JC016213

Nurser, A. J. G., & Bacon, S. (2014). The rossby radius in the Arctic Ocean. *Ocean. Sci.*, *10*, 967–975. Retrieved from `www.ocean-sci.net/10/967/2014` doi: 10.5194/os-10-967-2014

Østerhus, S., Woodgate, R. A., Valdimarsson, H., Turrell, B., de Steur, L., Quadfasel, D., . . . Berx, B. (2019). Arctic Mediterranean exchanges: a consistent volume budget and trends in transports from two decades of observations. *Ocean. Sci.*, *15*, 379–399. doi: https://doi.org/10.5194/os-15-379-2019

Padman, L., & Dillon, T. M. (1988). On the horizontal extent of thermohaline steps in the Canada Basin. *J. Phys. Oceanogr.*, *18*, 1458–1462.

Peralta-Ferriz, C., Morison, J. H., Wallace, J. M., Bonin, J. A., & Zhang, J. (2014). Arctic Ocean circulation patterns revealed by GRACE. *J. Climate*, *27*(4), 1445–1468. doi: 10.1175/JCLI-D-13-00013.1

Peralta-Ferriz, C., & Woodgate, R. A. (2015). Seasonal and interannual variability of pan-Arctic surface mixed layer properties from 1979 to 2012 from hydrographic data, and the dominance of stratification for multiyear mixed layer depth shoaling. *Progress in Oceanography*, *134*, 19–53. doi: 10.1016/j.pocean.2014.12.005

Perovich, D. K., Richter-Menge, J., Jones, K., Light, B., Elder, B. C., Polashenski, C., . . . Lindsay, R. (2011). Arctic sea-ice melt in 2008 and the role of solar heating. *Annals of Glaciology*, *52*(57), 355–359.

Piecuch, C. G. (2017). *A note on practical evaluation of budgets in ecco version 4 release 3* (Tech. Rep.). Retrieved from `http://hdl.handle.net/1721.1/111094`

Piecuch, C. G., & Ponte, R. M. (2012). Importance of circulation changes to Atlantic heat storage rates on seasonal and interannual time scales. *J. Climate*, *25*(1), 350–362. doi: 10.1175/JCLI-D-11-00123.1

Piecuch, C. G., & Ponte, R. M. (2013). Mechanisms of global-mean steric sea level change. *Journal of Climate*, *27*, 824–834. doi: 10.1175/JCLI-D-13-00373.1

Piecuch, C. G., Ponte, R. M., Little, C. M., Buckley, M. W., & Fukumori, I. (2017). Mechanisms underlying recent decadal changes in subpolar North Atlantic ocean heat content. *J. Geophys. Res.*, *122*, 7181–7197. doi: 10.1002/2017JC012845

Pillar, H. R., Heimbach, P., Johnson, H. L., & Marshall, D. P. (2016). Dynamical attribution of recent variability in Atlantic overturning. *J. Clim.*, *29*, 3339–3352. doi: 10.1175/JCLI-D-15-0727.1

Pilo, G. S., Oke, P. R., Coleman, R., Rykova, T., & Ridgway, K. (2018). Impact of data assimilation on vertical velocities in an eddy resolving ocean model. *Ocean Modelling*, *131*, 71–85. doi: 10.1016/j.ocemod.2018.09.003

Pnyushkov, A. V., Polyakov, I. V., Ivanov, V. V., Aksenov, Y., Coward, A. C., Janout, M., & Rabe, B. (2015). Structure and variability of the boundary current in the Eurasian Basin of the Arctic Ocean. *Deep Sea Research Part I: Oceanographic Research Papers*, *101*, 80–97. doi: 10.1016/j.dsr.2015.03.001

Pnyushkov, A. V., Polyakov, I. V., Ivanov, V. V., & Kikuchi, T. (2013). Structure of the Fram Strait branch of the boundary current in the Eurasian Basin in the Arctic Ocean. *Polar Science*, *7*(2). (10.1016/j.polar.2013.02.001)

Pnyushkov, A. V., Polyakov, I. V., Padman, L., & Nguyen, A. T. (2018). Structure and dynamics of mesoscale eddies over the Laptev Sea continental slope in the Arctic Ocean. *Ocean Sci.*, *14*, 1329–1347. doi: https://doi.org/10.5194/os-14-1329-2018

Polyakov, I. V., Alexeev, V. A., Ashik, I. M., Bacon, S., Beszczynska-Möller, A., Carmack, E. C., . . . Woodgate, R. A. (2011). Fate of early 2000s Arctic warm water pulse. *Bull. Amer. Meteor. Soc.*, *92*(5), 561–566. doi: 10.1175/2010BAMS2921.1

Polyakov, I. V., Pnyushkov, A. V., Alkire, M. B., Ashik, I. M., Baumann, T. M., Carmack, E. C., . . . Yulin, A. (2017). Greater role for Atlantic inflows on sea-ice loss in the Eurasian Basin of the Arctic Ocean. *Science*, *356*, 285–291. doi: 10.1126/science.aai8204

Polyakov, I. V., Pnyushkov, A. V., & Timokhov, L. A. (2012). Warming of the intermediate atlantic water of the arctic ocean in the 2000s. *J. Climate*, *25*(23), 8362–8370. doi: 10.1175/JCLI-D-12-00266.1

Polyakov, I. V., Rippeth, T. P., Fer, I., Alkire, M. B., Baumann, T. M., Carmack, E. C., … Rember, R. (2020). Weakening of cold halocline layer exposes sea ice to oceanic heat in the eastern Arctic Ocean. *Journal of Climate*. (in press) doi: 10.1175/JCLI-D-19-0976.1

Pradal, M.-A., & Gnanadesikan, A. (2014). How does the Redi parameter for mesoscale mixing impact global climate in an Earth System Model? *J. Adv. Model. Earth Syst.*, *6*, 586–601. doi: 10.1002/2013MS000273

Project Jupyter, Matthias Bussonnier, Jessica Forde, Jeremy Freeman, Brian Granger, Tim Head, … Carol Willing (2018). Binder 2.0 - Reproducible, interactive, sharable environments for science at scale. In Fatih Akici, David Lippa, Dillon Niederhut, & M. Pacer (Eds.), *Proceedings of the 17th Python in Science Conference* (p. 113 - 120). doi: 10.25080/Majora-4af1f417-011

Proshutinsky, A., Krishfield, R. A., & Timmermans, M. L. (2020). Introduction to special collection on Arctic Ocean modeling and observational synthesis (FAMOS) 2: Beaufort Gyre phenomenon. *J. Geophys. Res.*, *125*. doi: https://doi.org/10.1029/2019JC015400

Proshutinsky, A., Krishfield, R. A., Timmermans, M.-L., Toole, J. M., Carmack, E., McLaughlin, F., … Shimada, K. (2009). Beaufort Gyre freshwater reservoir: State and variability from observations. *J. Geophys. Res.*, *114*(C1), C00A10. doi: 10.1029/2008JC005104

Proshutinsky, A., Krishfield, R. A., Toole, J. M., Timmermans, M.-L., Williams, W., Zimmermann, S., … Zhao, J. (2019). Analysis of the Beaufort Gyre freshwater content in 20032018. *J. Geophys. Res.*, *124*, 9658–9689. doi: https://doi.org/10.1029/2019JC015281

Rabe, B., Karcher, M., Kauker, F., Schauer, U., Toole, J. M., Krishfield, R. A., … Su, J. (2014). Arctic Ocean basin liquid freshwater storage trend 1992–2012. *Geophys. Res. Lett.*, *41*, 961–968. doi: 10.1002/2013GL058121

Rainville, L., & Woodgate, R. A. (2009). Observations of internal wave generation in the seasonally ice-free Arctic. *Geophys. Res. Lett.*, *36*(23), L23604.

Redi, M. H. (1982). Oceanic isopycnal mixing by coordinate rotation. *J. Phys. Oceanogr.*, *12*, 1154–1158.

Richter-Menge, J., & Jeffries, M. (2011). The Arctic. *Bulletin American Meteorological Society*, *92*, S143-S160.

Ricker, R., Tian-Kunze, S. H. L. K. X., King, J., & Haas, C. (2017). A weekly Arctic sea-ice thickness data record from merged CryoSat-2 and SMOS satellite data. *The Cryosphere*, *11*, 1607–1623. doi: 10.5194/tc-11-1607-2017

Rossby, T., Flagg, C., Chafik, L., Harden, B., & Søiland, H. (2018). A direct estimate of volume, heat, and freshwater exchange across the Greenland-Iceland-Faroe-Scotland ridge. *J. Geophys. Res.*, *123*, 7139–7153. doi: https://doi.org/10.1029/2018JC014250

Roullet, G., & Madec, G. (2000). Salt conservation, free surface, and varying levels: a new formulation for ocean general circulation models. *J. Geophys. Res.*, *105*(C10), 23927–23942.

Rudels, B. (2012). Arctic ocean circulation and variability - advection and external forcing encounter constraints and local processes. *Ocean Science*, *8*(2), 261–286. doi: 10.5194/os-8-261-2012

Rudels, B. (2015). Arctic Ocean circulation, processes and water masses: A description of observations and ideas with focus on the period prior to the International Polar Year 2007–2009. *Progress in Oceanography*, *132*, 22–67. doi: 10.1016/j.pocean.2013.11.006

Rudels, B., Jones, E. P., Schauer, U., & Eriksson, P. (2004). Atlantic sources of the Arctic Ocean surface and halocline waters. *Polar Research*, *23*(2), 81–208.

Schauer, U., & Beszczynska-Möller, A. (2009). Problems with estimation and interpretation of oceanic heat transportconceptual remarks for the case of Fram Strait in the Arctic Ocean. *Ocean Science*, *5*, 487–494. doi: https://doi.org/10.5194/os-5-487-2009

Schauer, U., & Fahrbach, E. (2004). Arctic warming through the Fram Strait: Oceanic heat transport from 3 years of measurements. *J. Geophys. Res.*, *109*(C06026). doi: 10.1029/2003JC001823

Schauer, U., & Losch, M. (2019). "freshwater" in the ocean is not a useful parameter in climate research. *Journal of Physical Oceanography*, *49*(9), 2309–2321. doi: 10.1175/JPO-D-19-0102.1

Sciascia, R., Straneo, F., Cenedese, C., & Heimbach, P. (2013). Seasonal variability of submarine melt rate and circulation in an East Greenland fjord. *Journal of Geophysical Research*, *118*, 2492–2506. doi: 10.1002/jgrc.20142

Shiklomanov, A. I., Déry, S., Tretiakov, M., Yang, D., Magritsky, D., Georgiadi, A., & Tang, W. (2020, August). River Freshwater Flux to the Arctic Ocean. In *Arctic hydrology, permafrost and ecosystems* (pp. 703–738). Cham: Springer International Publishing.

Shiklomanov, A. I., Yakovleva, T. I., Lammers, R. B., Karasev, I. P., Vörösmarty, C. J., & Linder, E. (2006). Cold region river discharge uncertainty—estimates from large Russian rivers. *Journal of Hydrology*, *326*(1-4), 231–256.

Sirevaag, A., & Fer, I. (2012). Vertical heat transfer in the Arctic Ocean: the role of double-diffusive mixing. *J. Geophys. Res.*, *117*(C07010). doi: doi:10.1029/2012JC007910

Sivareddy, S., Paul, A., Sluka, T., Ravichandran, M., & Kalnay, E. (2017). The pre-Argo ocean reanalyses may be seriously affected by the spatial coverage of moored buoys. *Scientific Reports*, *7*(46685). doi: 10.1038/srep46685

Skagseth, O., Furevik, T., Ingvaldsen, R., Loeng, H., Mork, K. A., Orvik, K. A., & Ozhigin, V. (2008). Chapter: Volume and heat transports to the Arctic Ocean via the Norwegian and Barents Seas. In R. R. Dickson, J. Meincke, & P. Rhines (Eds.), *Arcticsubarctic ocean fluxes* (pp. 45–64). Netherlands: Springer. doi: https://doi.org/10.1007/978-1-4020-6774-7_3

Smedsrud, L. H., Ingvaldsen, R., Nilsen, J. E. O., & Skagseth, O. (2010). Heat in the Barents Sea: Transport, storage and surface fluxes. *Ocean Sci.*, *6*(1), 219–234. doi: https://doi.org/10.5194/os-6-219-2010

Smith, T. (2021, January). *crios-ut/aste: Aste release 1.* Zenodo. Retrieved from `https://doi.org/10.5281/zenodo.4479779` doi: 10.5281/zenodo.4479779

Smith, W., & Sandwell, D. T. (1997). Global sea floor topography from satellite altimetry and ship depth soundings. *Science*, *277*(5334), 1956–1962.

Spall, M. A. (2020, 08). Potential vorticity dynamics of the Arctic halocline. *Journal of Physical Oceanography*, *50*(9), 2491-2506. doi: 10.1175/JPO-D-20-0056.1

Spreen, G., Kern, S., Stammer, D., & Hansen, E. (2009). Fram Strait sea ice volume export estimated between 2003 and 2008 from satellite data. *Geophys. Res. Lett.*, *36*(L19502). doi: 10.1029/2009GL039591

Stammer, D., Balmaseda, M., Heimbach, P., Köhl, A., & Weaver, A. (2016). Ocean data assimilation in support of climate applications: Status and perspectives. *Annu. Rev. Mar. Sci.*, *8*(accepted). doi: 10.1146/annurev-marine-122414-034113

Stammer, D., Wunsch, C., Giering, R., Eckert, C., Heimbach, P., Marotzke, J., ... Marshall, J. (2002). Global ocean circulation during 1992–1997, estimated from ocean observations and a general circulation model. *Journal of Geophysical Research*, *107*(C9), 3118–1–27.

Steele, M., Morley, R., & Ermold, W. (2001). PHC: A global ocean hydrography with a high-quality arctic ocean. *J. Clim.*, *14*, 2079–2087.

Straneo, F., & Cenedese, C. (2015). The dynamics of Greenlands glacial fjords and their role in climate. *Annu. Rev. Mar. Sci.*, *7*, 89112. doi: 10.1146/annurev-marine-010213-135133

Tesdal, J.-E., & Haine, T. W. N. (2020). Dominant terms in the freshwater and heat budgets of the subpolar North Atlantic Ocean and Nordic Seas from 1992 to 2015. *J. Geophys. Res.*. (submitted) doi: https://doi.org/10.1002/essoar.10503232.1

Tian-Kunze, X., Kaleschke, L., Maass, N., Maekynen, M., Serra, N., Drusch, M., & Krumpen, T. (2014). SMOS-derived sea ice thickness: algorithm baseline, product specifications and initial verification. *The Cryosphere*, *8*, 997–1018. (doi:10.5194/tc-8-997-2014)

Timmermans, M.-L., Cole, S., & Toole, J. M. (2012). Horizontal density structure and restratification of the Arctic Ocean surface layer. *J. Phys. Oceanogr.*, *42*(4), 659–668. doi: 10.1175/JPO-D-11-0125.1

Timmermans, M.-L., & Jayne, S. R. (2016). The Arctic Ocean spices up. *Journal of Physical Oceanography*, *46*, 1277–1284. doi: 10.1175/JPO-D-16-0027.1

Timmermans, M.-L., & Marshall, J. (2020). Understanding Arctic Ocean circulation: A review of ocean dynamics in a changing climate. *Journal of Geophysical Research*, *125*(4), e2018JC014378. doi: 10.1029/2018JC014378

Timmermans, M.-L., Toole, J. M., & Krishfield, R. A. (2018). Warming of the interior Arctic Ocean linked to sea ice losses at the basin margins. *Science Advances*, *4*(8). doi: 10.1126/sciadv.aat6773

Toohey, R. C., Herman-Mercer, N. M., Schuster, P. F., Mutter, E. A., & Koch, J. C. (2016). Multidecadal increases in the Yukon River Basin of chemical fluxes as indicators of changing flowpaths, groundwater, and permafrost. *Geophys. Res. Lett.*, *43*, 12120–12,130. doi: 10.1002/2016GL070817

Toole, J. M. (2007). Temporal characteristics of abyssal finescale motions above rough bathymetry. *Journal of Physical Oceanography*, *37*(3), 409-427. Retrieved from `https://doi.org/10.1175/JPO2988.1` doi: 10.1175/JPO2988.1

Toole, J. M., Krishfield, R. A., & Timmermans, M.-L. (2011). The ice-tethered profiler: Argo of the Arctic. *Oceanography*, *24*(3), 126–135. doi: 10.5670/oceanog.2011.64

Treguier, A. M., Deshayes, J., Le Sommer, J., Lique, C., Madec, G., Penduff, T., . . . Talandier, C. (2014). Meridional transport of salt in the global ocean from an eddy-resolving model. *Ocean Science*, *10*(2), 243–255. doi: 10.5194/os-10-243-2014

Tsubouchi, T., Bacon, S., Aksenov, Y., Garabato, A. C. N., Beszczynska-Möller, A., Hansen, E., . . . Lee, C. M. (2018). The Arctic Ocean seasonal cycles of heat and freshwater fluxes: Observation-based inverse estimates. *Journal of Physical Oceanography*, *48*(9), 2029–2055. doi: 10.1175/JPO-D-17-0239.1

Uotila, P., Goosse, H., Haines, K., Chevallier, M., Barthélemy, A., Bricaud, C., . . . Zhang, Z. (2019). An assessment of ten ocean reanalyses in the polar regions. *Clim Dyn*, *52*, 1613–1650. doi: 10.1007/s00382-018-4242-z

Verdy, A., Cornuelle, B., Mazloff, M. R., & Rudnick, D. L. (2017). Estimation of the tropical Pacific Ocean state 2010-13. *J. Atm. Oceanic Tech.*, *34*, 1501–1517. doi: 10.1175/JTECH-D-16-0223.1

Vinogradova, N. T., & Ponte, R. M. (2012). Assessing temporal aliasing in satellite-based salinity measurements. *J. Atmos. Ocean. Technol.*, *29*(9), 1391–1400. doi: 10.1175/JTECH-D-11-00055.1

von Appen, W.-J., Schauer, U., Hattermann, T., & Beszczynska-Möller, A. (2015a). Seasonal cycle of mesoscale instability of the West Spitsbergen Current. *Journal of Physical Oceanography*, 1231–1254. doi: doi:10.1175/jpo-d-15-0184.1

von Appen, W.-J., Schauer, U., Somavilla Cabrillo, R., Bauerfeind, E., & Beszczynska-Möller, A. (2015b). Exchange of warming deep waters across

Fram Strait. *Deep Sea Res.*, 86–100. doi: doi:10.1016/j.dsr.2015.06.003

Våge, K., Moore, G. W. K., Jónsson, S., & Valdimarsson, H. (2015). Water mass transformation in the Iceland Sea. *Deep Sea Res. Part I*, *101*, 98–109. (doi:10.1016/j.dsr.2015.04.001)

Wadhams, P., Comiso, J. C., Prussen, E., Wells, S., Brandon, M., Aldworth, E., ... Crane, D. R. (1996). The development of the Oden ice tongue in the Greenland Sea during winter 1993 from remote sensing and field observations. *J. Geophys. Res.*, *101*(C8), 18213–18235.

Wang, C., Graham, R. M., Wang, K., Gerland, S., & Granskog, M. A. (2019). Comparison of ERA5 and ERA-Interim near-surface air temperature, snowfall and precipitation over Arctic sea ice: effects on sea ice thermodynamics and evolution. *The Cryosphere*, *13*(6), 1661–1679. doi: 10.5194/tc-13-1661-2019

Wang, Q., Ilicak, M., Gerdes, R., Drange, H., Aksenov, Y., Bailey, D. A., ... Yeager, S. G. (2016a). An assessment of the Arctic Ocean in a suite of interannual CORE-II simulations. part ii: Liquid freshwater. *Ocean Modelling*, *99*, 86–109. Retrieved from `http://www.sciencedirect.com/science/article/pii/S1463500315002450` doi: https://doi.org/10.1016/j.ocemod.2015.12.009

Wang, Q., Ilicak, M., Gerdes, R., Drange, H., Aksenov, Y., Bailey, D. A., ... Yeager, S. G. (2016b). An assessment of the Arctic Ocean in a suite of interannual CORE-II simulations. part i: Sea ice and solid freshwater. *Ocean Modelling*, *99*, 110–132. doi: https://doi.org/10.1016/j.ocemod.2015.12.008

Wang, Q., Wekerle, C., Wang, X., Danilov, S., Koldunov, N., Sein, D., ... Jung, T. (2020). Intensification of the Atlantic Water supply to the Arctic Ocean through Fram Strait induced by Arctic sea ice decline. *Geophysical Research Letters*, *47*(3). doi: 10.1029/2019GL086682

Watkins, M. M., Wiese, D. N., Yuan, D.-N., Böning, C., & Landerer, F. W. (2015). Improved methods for observing earth's time variable mass distribution with GRACE using spherical cap mascons. *J. Geophys. Res.*, *120*(4), 2648–2671. doi: 10.1002/2014JB011547

Weijer, W., Maltrud, M. E., Hecht, M. W., Dijkstra, H. A., & Kliphuis, M. A. (2012). Response of the Atlantic Ocean circulation to Greenland Ice Sheet melting in a strongly-eddying ocean model. *Geophys. Res. Lett.*, *39*(L09606). doi: 10.1029/2012GL051611

Wiese, D., Yuan, N., Böning, C., Landerer, F. W., & Watkins, M. M. (2018). *JPL GRACE mascon ocean, ice, and hydrology equivalent water height release 06 coastal resolution improvement (cri) filtered version 1.0. ver. 1.0. po.daac, ca, usa.* `https://doi.org/10.5067/TEMSC-3MJC6`. (Dataset Accessed: 2019-11-08) doi: 10.5067/TEMSC-3MJC6

Wolfe, C. L., Hameed, S., & Chi, L. (2019). On the drivers of decadal variability of the Gulf Stream North Wall. *J. Climate*, *32*, 1235–1249. doi: 10.1175/JCLI-D-18-0212.1

Woodgate, R. A. (2018). Increases in the Pacific inflow to the Arctic from 1990 to 2015, and insights into seasonal trends and driving mechanisms from year-round Bering Strait mooring data. *Progress in Oceanography*, *160*, 124–154. doi: https://doi.org/10.1016/j.pocean.2017.12.007

Woodgate, R. A., Stafford, K. J., & Prahl, F. G. (2015). A synthesis of year-round interdisciplinary mooring measurements in the Bering Strait (1990–2014) and the RUSALCA years (2004–2011). *Oceanography*, *28*(3), 46–67. doi: 10.5670/oceanog.2015.57

Wunsch, C. (2018). Towards determining uncertainties in global oceanic mean values of heat, salt, and surface elevation. *Tellus A: Dynamic Meteorology and Oceanography*, *70*(1), 1-14. doi: 10.1080/16000870.2018.1471911

Wunsch, C., & Heimbach, P. (2007). Practical global oceanic state estimation. *Physica D: Nonlinear Phenomena*, *230*(1-2), 197–208. doi: 10.1016/j.physd.2006.09.040

Wunsch, C., & Heimbach, P. (2013). Dynamically and Kinematically Consistent Global Ocean Circulation and Ice State Estimates. In *Ocean circulation and climate: A 21st century perspective* (pp. 553–579). Elsevier Ltd. doi: 10.1016/B978-0-12-391851-2.00021-0

Yang, J. (2005). The Arctic and subarctic ocean flux of potential vorticity and the Arctic Ocean circulation. *J. Phys. Oceanogr.*, *35*, 2387–2407.

Yin, J., Stouffer, R. J., Spelman, M. J., & Griffies, S. M. (2010). Evaluating the uncertainty induced by the virtual salt flux assumption in climate simulations and future projections. *Journal of Climate*, *23*, 80–96. doi: 10.1175/2009JCLI3084.1

Zaba, K. D., Rudnick, D. L., Cornuelle, B. D., Gopalakrishnan, G., & Mazloff, M. R. (2018). Annual and interannual variability in the California Current System: comparison of an ocean state estimate with a network of underwater gliders. *J. Phys. Oceanogr.*, *48*, 2965–2988. doi: 10.1175/JPO-D-18-0037.1

Zhang, J., & Rothrock, D. A. (2003). Modeling global sea ice with a thickness and enthalpy distribution model in generalized curvilinear coordinates. *Mon. Weather Rev.*, *131*, 845–861.

Zhang, J., & Steele, M. (2007). Effect of vertical mixing on the atlantic water layer circulation in the arctic ocean. *J. Geophys. Res.*, *112*(C04S04), doi:10.1029/2006JC003732.

Zhao, M., Timmermans, M.-L., Cole, S., Krishfield, R. A., & Toole, J. M. (2016). Evolution of the eddy field in the Arctic Oceans Canada Basin, 20052015. *Geophys. Res. Lett.*, *43*, 8106–8114. doi: 10.1002/2016GL069671

Zlotnicki, V., Qu, Z., & Willis, J. (2019). *MEaSUREs gridded sea surface height anomalies version 1812. ver. 1812. PO.DAAC, CA, USA.* https://doi.org/10.5067/SLREF-CDRV2. (Dataset Accessed: 2019-11-08) doi: 10.5067/SLREF-CDRV2

Zweng, M. M., Reagan, J. R., Seidov, D., Boyer, T. P., Locarnini, R. A., Garcia, H. E., … Smolyar, I. (2018). Volume 2: Salinity. In A. Mishonov (Ed.), . NOAA Atlas NESDIS 82, U.S. Government Printing Office, Washington, D.C.